REVIEW ARTICLE

Check for updates

Clarifying the local microenvironment of metal–organic frameworks and their derivatives for electrochemical CO_2 reduction: advances and perspectives

Muhammad Kashif Aslam, Kang Yang, Sheng Chen, [ID] * Qiang Li* and Jingjing Duan [ID] *

The conversion of carbon dioxide (CO_2) into fuels, value-added products and electricity is one of the most effective ways to reduce the atmospheric CO_2 concentration, and thus mitigate the greenhouse effect, simultaneously resolving the environmental and energy crises. In this case, metal–organic frameworks (MOFs) show good application prospect in the catalytic CO_2 reduction reaction because of their well-defined porous structure, rich active sites and feasible functionalization. Herein, we summarize the latest research progress of MOFs and their derivatives for catalytic CO_2 electroreduction and discuss their mechanism, kinetics, thermodynamics and catalytic performance. Moreover, the effect of first-, secondary and out-sphere coordination on the metal active centers and the local microenvironment of MOFs, which can be manipulated by adjusting their metal nodes, organic linkers, and solvents, are addressed in-depth to clarify the key to their great electrocatalytic performance. Based on this, the main challenges and future outlook of MOF catalysts are summarized and perspectives presented.

Broader context

Renewable energy technologies are trying to reshape the energy pathway of modern society, which will decrease the usage of fossil fuels, and thus reduce the risk of future environmental degradation. The efficient utilization of renewable energy is the key, and thus there is a great demand for appropriate energy conversion technologies. The electrochemical reaction is the foundation and key of various energy conversion technologies. The electroreduction of CO_2 reaction (eCO_2RR) promoted by renewable power for the conversion of CO_2 into valuable industrial materials stores excess renewable energy as chemical energy in fuels. Therefore, eCO2RR is important technology to realize carbon recycling and renewable energy storage for a zero/negative carbon and energy cycle. In this case, the design of highly efficient electrocatalysts is crucial but challenging, which is significant for the actual use of conversion reactions. This work summarizes the key aspects and latest progress of MOFs and their derivatives for eCO_2RR in recent years. In combination with the research trend, the metal nodes, coordination types and configuration and local microenvironment are discussed in-depth. Finally, the problems and future development strategies of MOFs and MOF-derived confined materials in CO_2 reduction have been analyzed and prospected.

1. Introduction

Presently, the rapid industrialisation and excessive use of fossil fuels as an energy source have resulted in a significant increase in the concentration of carbon dioxide in the atmosphere, reaching a high value never seen in the last tens of millions of years. As a typical greenhouse gas, the increasing CO_2 concentration has increased the global temperature

MIIT Key Laboratory of Thermal Control of Electronic Equipment, School of Energy and Power Engineering, School of Chemistry and Chemical Engineering, Nanjing University of Science and Technology, Nanjing, 210094, China.
E-mail: jingjing.duan@njust.edu.cn

gradually,[1] leading to extreme weather, rising sea levels, species extinction and other serious consequences. Accordingly, renewable energy technology is reshaping the energy layout of modern society, which will decrease the use of fossil fuels and reduce the risk of future environmental degradation.[2–7] Here, the efficient utilization of renewable energy is the key, and thus there is a great demand for appropriate energy conversion technologies.[8–10] Electrochemical reactions are the foundation and key of various energy conversion technologies. For example, the electrochemical oxygen reduction reaction (ORR) is a vital cathode reaction in proton exchange membrane fuel cells (PEMFCs) to realize effective energy conversion.[11–13] Furthermore, techniques such as biological,[14] thermochemical,

photochemical, and electrochemical reactions are being widely studied for CO_2 reduction. Thermal CO_2 reduction can achieve the use of energy in the form of heat, where a pressurized reactant gas (CO_2) and high-performance catalyst to reduce the amount of energy consumed during CO_2 decomposition are required to utilize waste heat. In thermal CO_2 reduction, the catalyst facilitates the breakage of the strong $C=O$ bonds, which have a dissociation energy of 750 kJ mol^{-1} ($\sim 9 \times 10^4$ K). The reduction of CO_2 to CO was achieved at 1100 K using CeO_2, ZrO_2, $LaFeO_3$, and lanthanum-based perovskites as catalysts.[15–18] Alternatively, the electrochemical conversion of CO_2 has several advantages over thermal reduction, including mild reaction conditions, controllable reaction rates and product selectivity through the applied potential, and wide scalability due to modular electrolyzer design. However, the electroreduction of CO_2 reaction (CO_2RR) uses renewable power for the conversion of CO_2 into valuable industrial materials and stores excess renewable electric energy as chemical energy in fuels.[19] Therefore, CO_2RR is important technology to realize carbon recycling and renewable energy storage. Consequently, the design of high-efficiency electrocatalysts is crucial but challenging, which inhibit the actual use of conversion reactions.[3,20–24] Nevertheless, in these electrochemical conversion applications, the slow electrode reaction and low gas diffusion have become increasingly prominent. Noble metals (such as Ag and Au) and their derivatives are considered to be the key catalysts for the electroreduction of CO_2.[25–29] However, their high cost and low abundance hinder the commercial applications of noble metal catalysts. Consequently, researchers have devoted their efforts to finding alternatives to noble metal catalysts for electrocatalysis. In this case, non-noble metal–carbon catalysts with high activity are known as the superior choice and receiving increasing attention.[30] Scheme 1 schematically illustrates the first CO_2RR catalyst and some representative work.

Carbon materials with significant porosity have become the main catalysts to replace precious metals due to their outstanding physiochemical stability, high porosity with variable pore size, high surface area, and feasible synthesis method.[31–34] Metal–organic frameworks (MOFs) are porous materials with well-defined crystallinity constructed of organic ligands and metal centers.[35] MOF-confined carbon materials exhibit several advantages, as follows: (1) significantly porous, large surface area and variable pore size, which are beneficial for the enrichment and diffusion of gas molecules and conducive to mass transport.[36] (2) The components (metal nodes and linkers) of MOFs can catalyse important reactions by creating charge transfer interactions with active sites through π bond coordination, thus chemically improving the microenvironment.[37–40] (3) Compared with ordinary carbon catalysts, MOF-derived carbon shells can efficiently encapsulate the active center and prevent the leaching or agglomeration of particles, thus exhibiting excellent electrochemical stability during catalysis.[41,42] (4) MOF materials possessing a transition metal are regularly used as active centers for electrocatalysis. The active centers in MOFs and MOF-derived catalysts are

uniformly dispersed due their homogeneously arranged metal nodes and linkers.[43] Therefore, MOF-derived carbon-containing materials are extensively used as electrocatalysts.[44–46] The porous multifunctional structure of MOFs can be tuned via heteroatom-doping of carbon electrocatalysts obtained through calcination, such as N-, Fe-, Co-, and Ni-doping, whereas some studies have suggested the use of the as-prepared MOFs for CO_2RR without further treatment. In addition to the above-mentioned valuable properties, the synthesis of MOF materials is cost-effective, and MOFs can be converted into single-atom catalysts, metal nanoparticle catalysts, metal oxides and carbon-based catalysts via single-step heat treatment.

Due to the diversity of MOF materials, many carbon materials having heteroatom doping, dispersed pore size and morphology can be obtained using MOF precursors. Usually, carbon materials with a large surface area can be obtained by proper heat treatment, and subsequently metal removal. Among the MOFs, Zn metal-based MOFs are the most frequently used materials because Zn can be reduced to metal Zn by the supporting carbon material at high temperatures. Also, the boiling point (908 °C) of metal Zn is low, and consequently Zn evaporates at about 900 °C via the simple calcination of Zn-based MOFs, resulting in the formation of carbon materials with high porosity and large surface area. In addition, MOFs and other metal ions can be used to prepare metallic single-atoms/clusters/nanoparticles with the confinement of porous carbon. The dispersion of metal species in the carbon matrix will be uniform and more active sites will be exposed for the electroactive metal species. The MOF-derived porous carbon base not only provides a conductive path for electron transfer, but also avoids the agglomeration of the metal species. Generally, the type of metal species (single atoms/clusters/nanoparticles) has an impact on the electronic structure of the catalytic material. Firstly, the type of material to be synthesized can be adjusted by regulating the proportion of metal source in the raw material.[47] Secondly, the type of metal states finally synthesized can also be tuned by controlling the temperature during carbonization.[48] However, at present, it is challenging to regulate the synthesis of specific types of materials, and thus the precise synthesis of metal types will be a fundamental strategy in the future. Recent research showed that MOF-derived carbon-based electrocatalysts under confinement engineering exhibit surprising results when used as electrocatalysts, as presented below. Firstly, the uniform distribution of metal centers in the carrier can be achieved because of the regular cavities/channels of MOFs, and also aggregation does not occur easily.

Specifically, spatial confinement can be used to stabilize and disperse individual atoms or nanoparticles to avoid agglomeration and advance the performance of the catalyst.[22,49–51] Secondly, by coordinating with the organic ligand in the MOF, the metal center can be better stabilized on the support, thus stabilizing the long-term cyclic performance of the catalyst. In addition, the confinement engineering in materials can subtly change the microelectronic properties of the active sites and
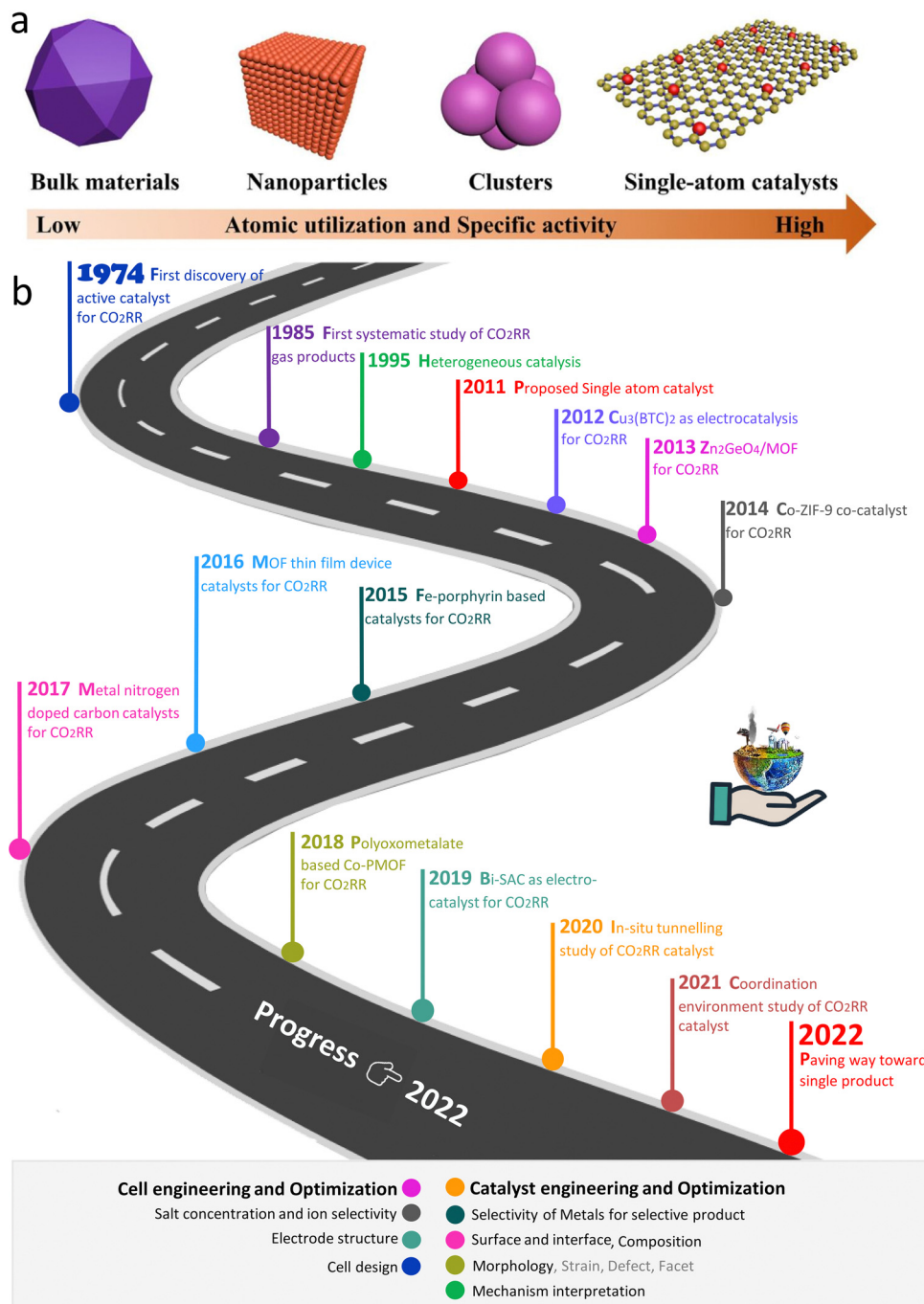
Scheme 1 (a) Illustration of size-dependent catalytic activity of materials. (b) Systematic depiction of some historic progress and works on the CO_2RR.

nearby microenvironment, enhancing the performance of the catalyst. To date, a relevant summary and review on MOF-derived and confinement-engineering-based electrocatalysis and the molecular-level interaction between the confinement engineering and reaction intermediates are limited. Because of the fast improvement in research in this direction and the continuous breakthroughs in catalyst performance (Scheme 2), herein, we summarize the key aspects and latest progress of new functional materials based on MOFs for CO_2RR in the last three years. In combination with

the research trend, the scope of the discussion is expanded, and three types of materials, *i.e.*, active MOFs, MOF composites and MOF derivatives, are discussed, focusing on the analysis of their physiochemical properties. It can be seen from the comparison of these materials that their metal site properties, ligand environment, morphology and size of the particles are common concerns in the design of catalysts. Finally, the problems and future development strategies of MOF and MOF-derived confined materials in CO_2 reduction are analyzed and prospected.
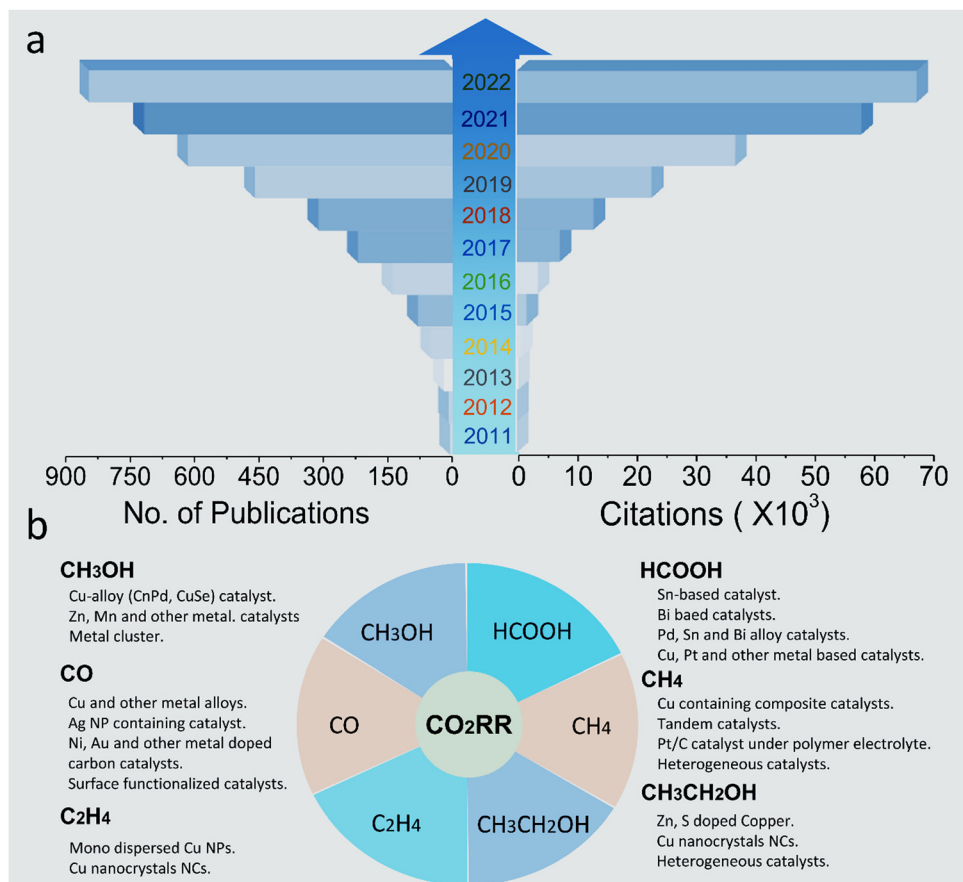
Scheme 2 (a) Trend of publications and citations of electroreduction of carbon dioxide, with data collected from Web of Science. (b) Systematic illustration of metal-based CO_2RR catalysts and their corresponding products.

2. Structural engineering to regulate catalytic performance

Carbon-based materials derived from MOFs exhibit a significant confinement effect when applied as electrocatalysts because of their ordered pore size, huge surface area, high porosity, and strong chemical composition adjustability, as follows: (1) different metal atoms and linkers have an important synergistic effect with restricted active centers, modifying the microelectronic structure of the active centers, and thus improving the catalytic performance. (2) The spatial distribution and specific crystal structure of the metal atoms and linkers offer an ideal scenario for elucidating the possible catalytic mechanism. (3) The active centers (including single atoms, clusters and nanoparticles) are confined in the cavity/channel of MOFs to prevent agglomeration, which helps to improve the catalytic stability. (4) The porous structure of MOFs has significant potential to regulate the catalytic stability by adjusting the reaction rate. To regulate the electronic structure and maintain the stability of the active sites in carbon compounds derived from MOFs, the confinement effect is a key factor. To increase the rate of adsorption and desorption of the reaction intermediates, to lower the energy barrier in the catalysis process, speed up the reaction kinetics and enhance

the catalytic activity, it is useful to regulate the microelectronic structure and stability of the active center.[52-54] Generally, the improvement in the catalytic performance by altering the electronic environment by coordinating the metal active center with a metal node or ligand is called the chemical coordination confinement effect. Given that coordination structures mostly exist in monatomic catalysts, the confinement effect mostly applies to monatomic catalysts. The effect of improving stability is called the spatial confinement effect, which mostly applies to metal-nanoparticle catalysts. Here, we explore both spatial confinement and chemical coordination compared to the confinement effect of carbon-based materials derived from MOFs in electrocatalytic applications.

2.1 Effect of chemical coordination confinement

The MOF precursor contains metal atoms and linkers, which are advantageous for the confinement of single-metal atoms in catalysts. To realize the dispersion of metal atoms, the desired metal atom can to some extent replace the original metal nodes in MOFs. The MOF precursor can also be used to stabilize the metal atoms. A certain degree of interactions is present between the confined metal atoms and the ligands in the MOF precursor, which stabilize the metal active centers.[55] Furthermore, besides the confinement of metal atoms in metal
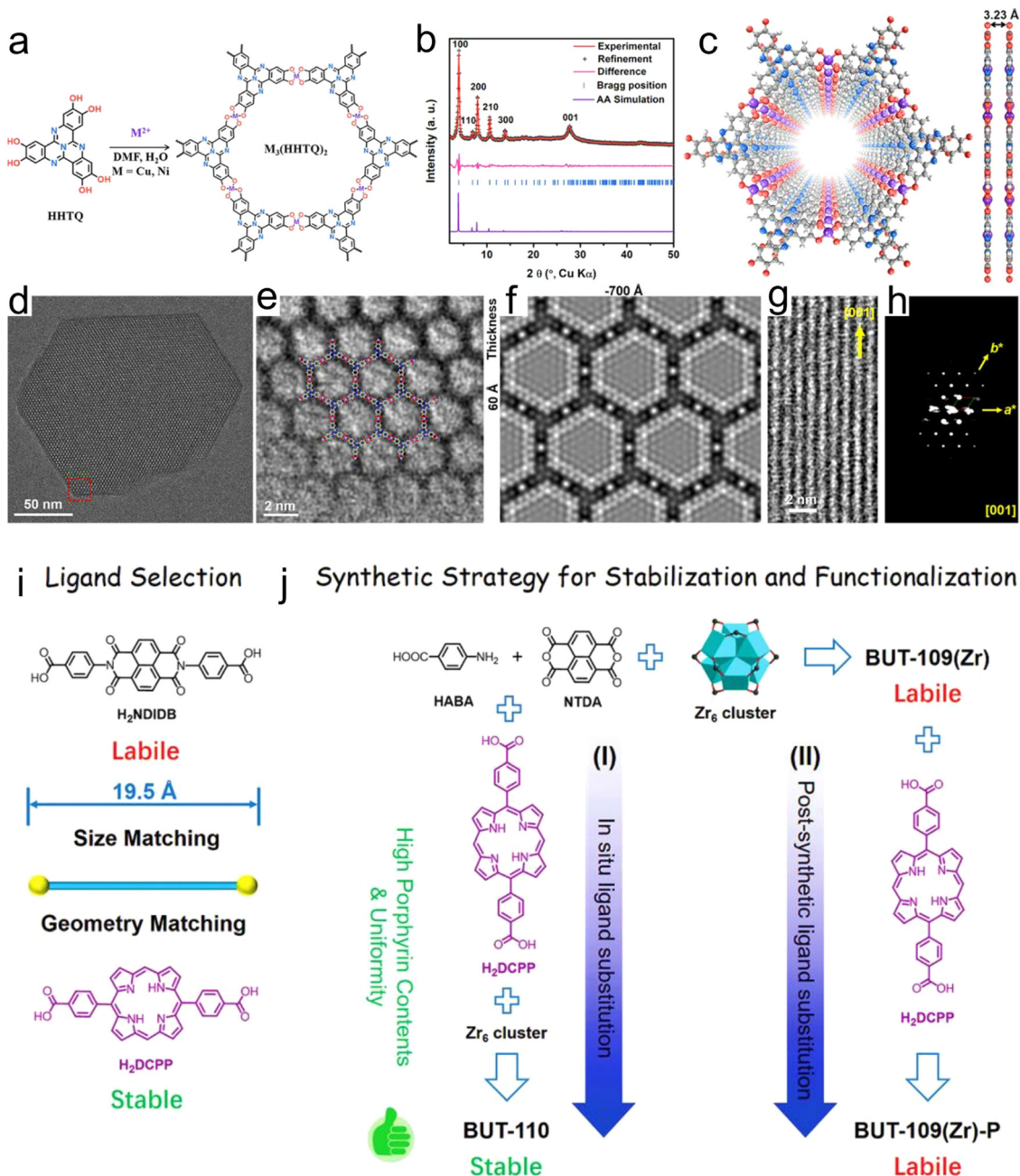
Fig. 1 (a) Synthesis of $M_3(HHTQ)_2$ (M = Cu and Ni). (b) Experimental and Pawley-refined PXRD patterns of $Cu_3(HHTQ)_2$. (c) Structural model of $Cu_3(HHTQ)_2$. (d) TEM image of $Cu_3(HHTQ)_2$ taken along the *c* axis. (e) Magnified view of HRTEM image for $Cu_3(HHTQ)_2$ taken along the *c* axis, showing a hexagonal pore and ligand termination, overlaid with the structure model. (f) Simulated TEM image along the [001] direction. (g) HRTEM image along the [120] direction. (h) Projection view of 3D EDT data of $Cu_3(HHTQ)_2$ along the [001] direction. Reproduced with permission from ref. 56 Copyright 2021, Wiley. (i) Ligand selection and (j) synthetic strategies of BUT-110 through (I) *in situ* ligand substitution and (II) post-synthetic ligand substitution. Reproduced with permission from ref. 57 Copyright 2021, Wiley.

nodes, other coordination structures can be assembled to immobilize metal atoms. In summary, the use of MOFs to confine a single-metal atoms is a simple and effective method.

Due to the presence of defects in the coordination sites in linkers or MOFs, MOFs can be used to design single-metal atoms for many reactions. Chen *et al.*[56] prepared a catalyst based on the nitrogen-rich tricyclic quinazoline (TQ), multi-

catechol ligands and transition metal ions, which coordinated to form a two-dimensional (2D) porous sheet similar to graphene and denoted as $M_3(HHTQ)_2$. The $M_3(HHTQ)_2$ catalyst can be considered an SA catalyst, in which the Ni or Cu sites are regularly distributed in the lattice (Fig. 1a–h). This study revealed the strong dependence of the catalytic performance on the metal sites and N-rich linkers, indicating that the

chemical confinement effect in the MOF coordinates with the organic ligands, having a noteworthy effect on the catalyst performance. Because the porphyrin unit has a clear planar symmetric anchor site, it can successfully anchor various noble metal atoms. For example, Li et al.[57] effectively designed a Zr porphyrin-based MOF using a viable coordination approach, displaying SA catalytic sites and exceptionally high catalytic performance (Fig. 1i and j).

In brief, the components of MOFs, i.e., their metal atoms and linkers, can confine single-metal atom catalysts and enhance the stability of the active centers. Consequently, the materials obtained by confinement in MOFs can be used as catalysts. Qin et al.[58] reported a broad approach for the large-scale preparation of $CoFe_2O_4/C$ nanocubes from MOFs through a combined exchange coordination and pyrolysis method (Fig. 2a). The strong restriction by the metal and organic MOF realizes the reconstruction of the crystal phase and composition, but not by simply introducing the metal oxide supported by Co^{2+}. Compared with $Co_3O_4Fe_2O_3/C$, the MOF-derived $CoFe_2O_4/C$ nanocubes possessed a higher surface area and better surface chemical properties, showing excellent catalytic activity and competitive water resistance.

Also, MOF-derived catalysts are commonly prepared via the domain-confining effect. Cao et al.[59] designed conductive 2D-phthalocyanine-based ($NiPc-NiO_4$) MOF nanosheets, which were used as an electrocatalyst for CO_2RR, efficiency producing
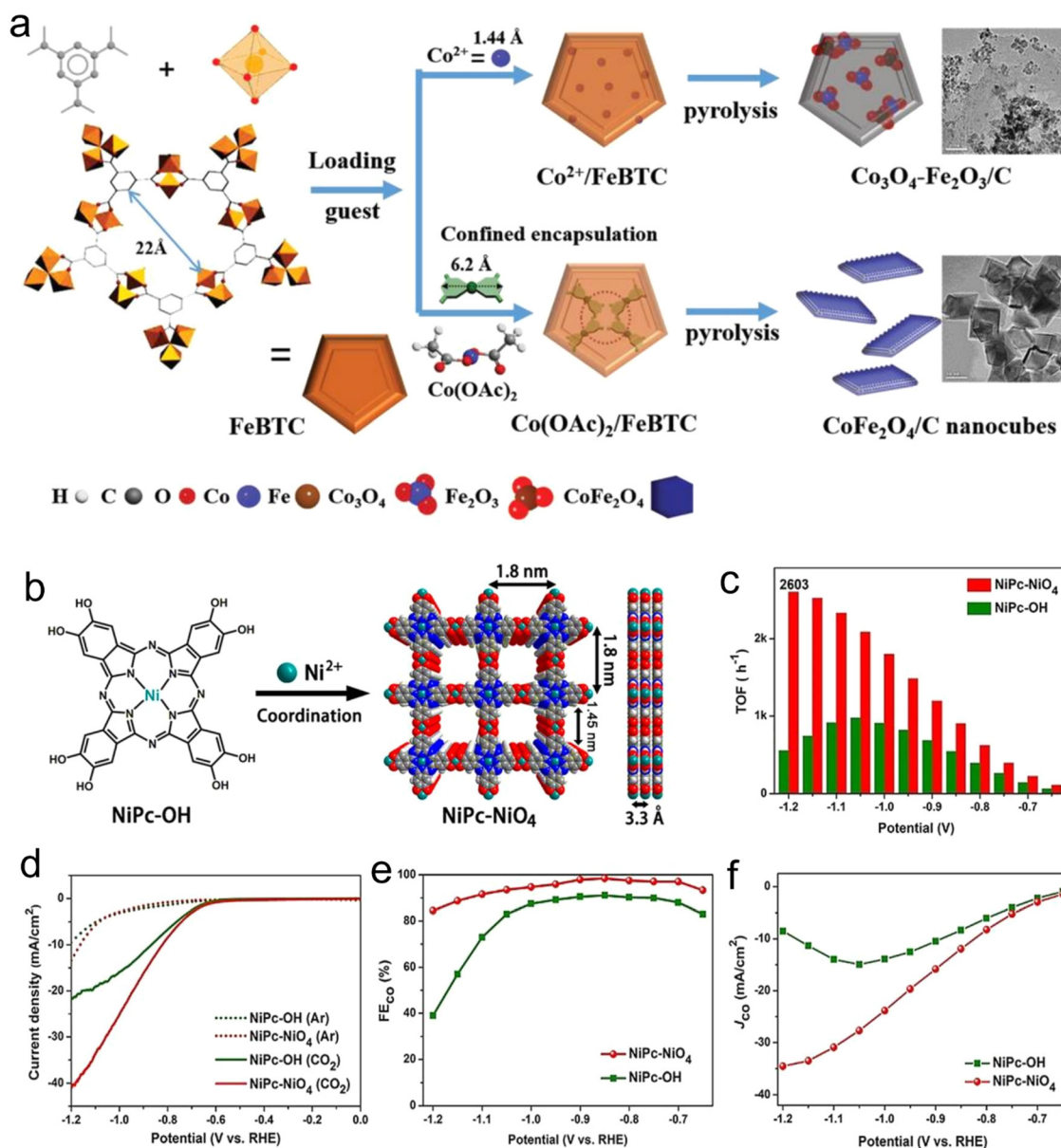

Fig. 2 (a) Illustration of assembly MOF–derived bimetallic spinel oxide $CoFe_2O_4$ nanocubes through the combination of exchange–coordination and pyrolysis. Reproduced with permission from ref. 58 Copyright 2020, Wiley. (b) Synthesis. (c) Turnover frequency. (d) LSV curves in CO_2. (e) FEs for CO. (f) CO partial current density of NiPc–NiO_4. Reproduced with permission from ref. 59 Copyright 2021, Wiley-VCH.

CO because of its planar full π-d conjugation. The prepared NiPc–NiO$_4$ nanosheets exhibited high selectivity (98.4%) and a CO partial current density of about 34.5 mA cm^{-2} (Fig. 2b–f). Single-metal atoms can be stabilized and dispersed through confinement via chemical coordination, and accordingly they can increase the stability and activity of the catalysts. However, to date, scarce research has been reported in the use of coordination confinement to stabilize nanoparticles. Consequently, designing new strategies for the synthesis and confining extra active centers is one of the main challenges in the development of efficient MOF-derived catalysts in the future.

2.2 Spatial confinement effect

MOFs are a new class of porous materials, which are appealing in many research fields because of their high specific surface area, uniform pore size, and exclusive tailorability and design. The presence of uniform porous structures allows MOFs to spatially disperse and confine metal active centers via appropriate confinement approaches. Xu et al.[60] reported the use of covalent organic framework materials (COFs) as shells and MOF as the yolk shell structure of the inner yolk to construct yolk–shell COF@MOF (YS-COF@MOF) via a template-free solvothermal method. The comparative experiments showed that the formation of the cavity between the core and shell under the catalysis of pyrrolidine is due to the transformation from amorphous to crystalline and the simultaneous contraction of the shell. YS-COF@MOF combined the inherent structure adjustability and function of the COF and MOF and exhibited the space-limiting effect of MOFs on other materials (Fig. 3a–e). Wang et al.[61] synthesized MIL-101 via the hydrothermal method, which possesed excellent thermal stability and highly ordered pore structure, and subsequently Au particles were immobilized and the content of Au was adjusted within a certain range. Based on the confining effect of MIL-101, the size of the Au nanoparticles could be controlled to less than 3 nm. The Au particles with this small size could provide good catalytic activity. Meanwhile, the pore confinement effect of MIF-101 ensured the uniform size and distribution of the nanoparticles.

Kim et al.[62] synthesized a bimetallic nanoparticle catalyst encapsulated in a conductive MOF (cMOF, Fig. 4a–e), in which the localization was guided by the site-specific nucleation induced by dipole interactions. The heterogeneous metal precursor was bound in the pores of the 2D cMOF through dipole interaction, and its subsequent reduction produced ultra-small and well-isolated PtRu-NPs with a size of ≈1.54 nm encapsulated in pores. Due to the bimetallic synergism of PtRu-NPs and the highly porous and large surface area of cMOFs, the PtRu-NPs-modified cMOFs exhibited a significantly enhanced NO$_2$ sensing performance. Usman et al.[63] demonstrated the confinement effect of a porous metal organic framework (HKUST-1) on the surface and wall of nanochannels by orbital etching in polyethylene terephthalate (np-PET) films using liquid phase epitaxy (LPE) (Fig. 4f). The composite film (HKUST-1/np-PET) showed the defect-free growth of the MOF, strong adhesion of the MOF to the carrier and high flexibility. The MOF has a preferred growth direction, which can capture CO$_2$ in natural gas and olefins. Experimentally and theoretically (DFT), it was confirmed that the confined diffusion of the gas only occurs on np-PET substrates confined by nanoporous MOFs. These findings provide a new perception for the growth of other porous MOFs for artificially prepared nanochannels and prove that the MOF structure has a limiting effect on the gas reactants in energy conversion.

3. Electrocatalysis carbon dioxide reduction (CO$_2$RR)

It is of great significance to effectively convert carbon dioxide into liquid fuels and high-value-added chemicals to alleviate global warming and the energy crisis at present, where the resource utilization technologies of CO$_2$ include catalytic hydrogenation, photochemical reduction, photocatalytic reduction and electrochemical reduction.[64] Among them, electrochemical technology has attracted wide attention because of its mild reaction conditions, which can effectively use the electric energy generated by renewable energy, for example, wind energy, solar energy and tidal energy, to convert CO$_2$ into a variety of carbon-containing compounds, and its high catalytic efficiency. According to the number of electrons transferred, the CO$_2$RR is generally divided into 2e$^-$, 4e$^-$, 6e$^-$, 8e$^-$ or 12e$^-$ electron reactions, and the thermodynamic potential energy of several reactions that may occur is different, resulting in the formation of mixed products of several carbonaceous compounds (Table 1 and Fig. 5).[65] At present, there are many challenges to realize the greatly effective CO$_2$RR, including the competing HER, which leads to a reduction in the product selectivity; the stable molecular structure of CO$_2$, and the high overpotential of CO$_2$ generated by electrons. In recent years, researchers have developed new catalyst structures to reduce the overpotential and inhibit the HER side reaction to improve the reactivity and selectivity for the CO$_2$RR.[66–68] In this case, various nanocatalysts such as gold (Au), silver (Ag) and copper (Cu) show excellent catalytic performances.[69] However, these traditional electrocatalysts exhibit several disadvantages, as follows: (1) they exhibit high overpotentials and slow kinetics for the multielectron CO$_2$RR. (2) It is still difficult to control the reaction path to generate carbon-based products with high selectivity. (3) The CO$_2$RR rate is mainly determined by the concentration of reactants, which limits the use of catalysts in a low-concentration CO$_2$ environment.[70] Therefore, the research on the application of MOF-based materials in the CO$_2$RR has developed rapidly, which can be divided into three directions, including the design of active MOF materials, the formation of composites of MOFs and other catalytic materials, and the development of MOF-based derivatives.

4. Mechanism, kinetics and thermodynamics of CO$_2$RR

4.1 Mechanism and kinetics

The electrochemical conversion pathway of CO$_2$ is thermodynamically favourable, where the energy barrier/overpotential
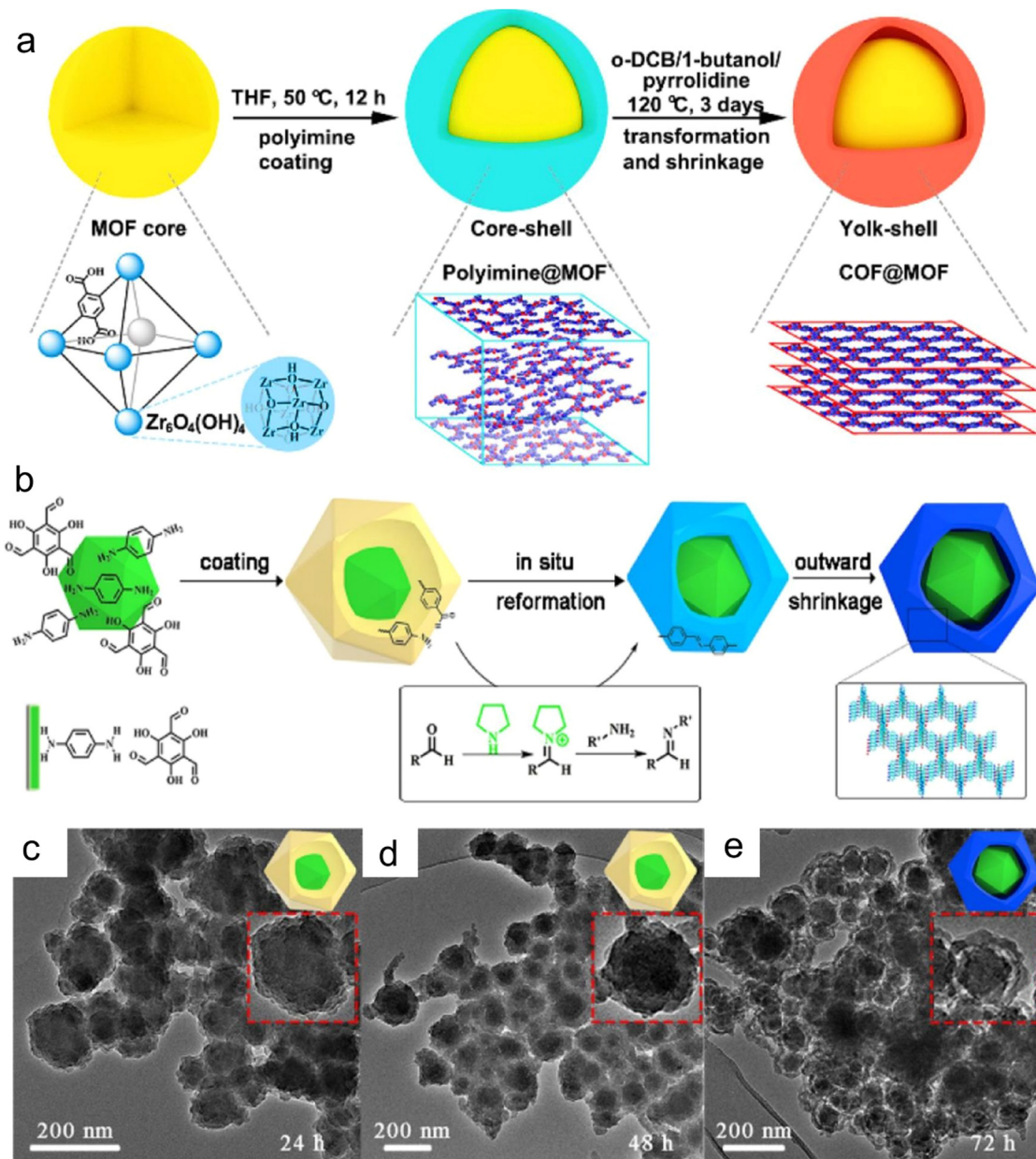
Fig. 3 (a) Synthesis of yolk shell COF@MOF nanocomposites and the *in situ* transformation of the COF shell. (b) Proposed mechanism of the formation of yolk–shell-structured COF@MOF. (c–e) Time-dependent experiments of YS-TpPa@UiO-66-(COOH)$_2$. Reproduced with permission from ref. 60 Copyright 2021, ACS.

decides the practical selectivity for the CO$_2$RR products. The selectivity, current density and long-time stable working hours are the critical parameters for commercial viability.[72] The mechanistic study of the CO$_2$RR includes two steps including the formation of intermediate products and formation of the final products. The mechanism of the different products (C$_1$, C$_2$ and C$_{2+}$) is different. Generally, the first step in the formation of mono carbon products (HCOOH and CO) is critical, where carbon dioxide can be activated by transferring of one electron from the catalyst surface (*CO$_2$•$^-$).[73–76] For the formation of the *COOH intermediate, proton-coupled electron transfer (PCET) occurs with *CO$_2$•$^-$. Also, after the formation of the *COOH

intermediate, PCET occurs again to convert this intermediate to CO. The *OCHO intermediate is generated by the interaction between *CO$_2$•$^-$ and the O atom, and then converted to formate *via* the electron-transfer protonation of the O atom.[77] In the suggested mechanism for the production of methanol, methane, and formaldehyde by the CO$_2$RR, theoretical and experimental studies illustrate that the first intermediate formed is *CO.[73,78] Subsequently, the *HCO, *H$_2$CO and *H$_3$CO intermediates are generated by the hydrogenation of *CO and transformed into HCHO, CH$_4$ and CH$_3$OH, respectively. However, there are two different views supporting the transformation of the *CO intermediate to CH$_4$, as follows: (1) it
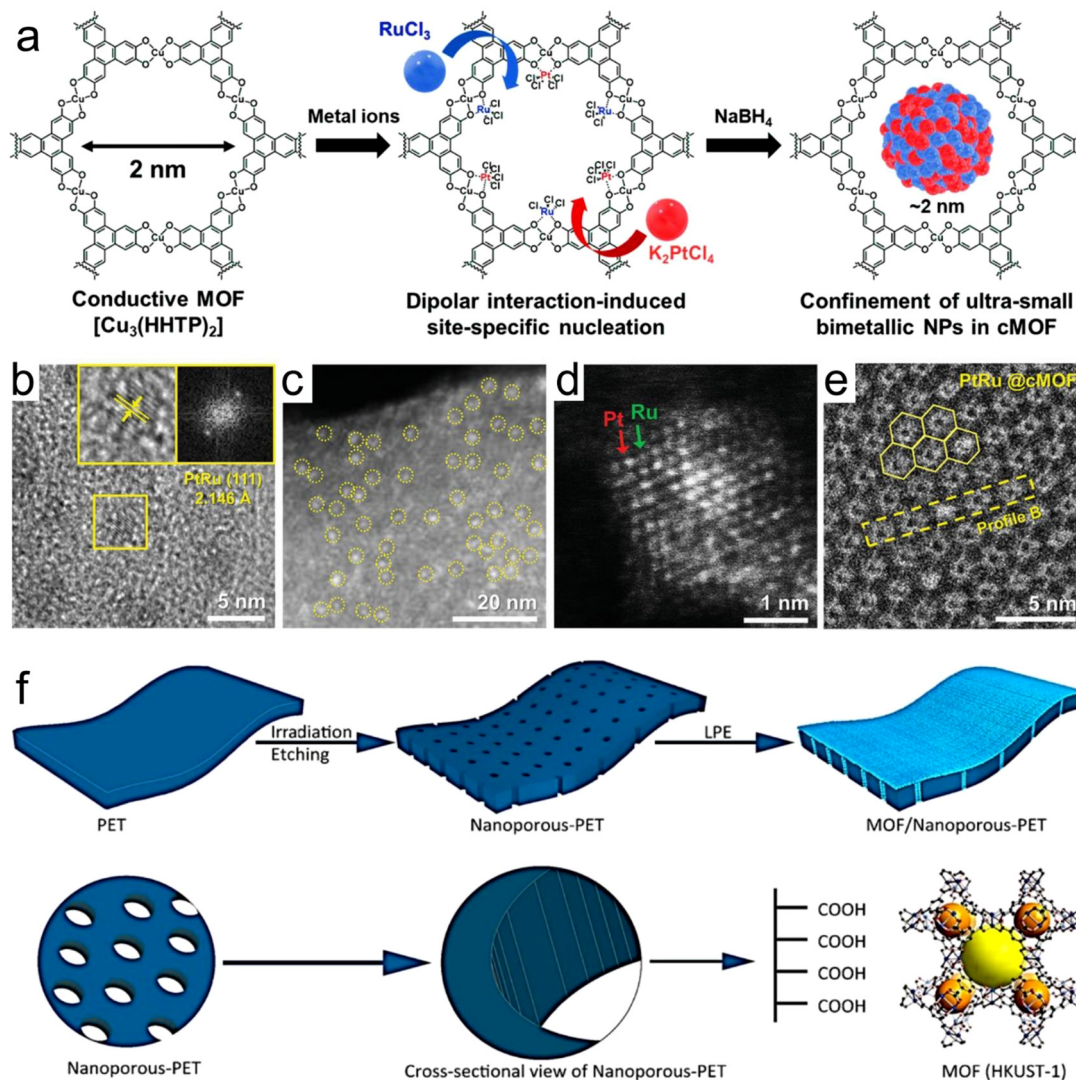
Fig. 4 (a) Synthesis of PtRu@cMOF. (b) HR-TEM image of PtRu@cMOF. The inset shows magnified images, exhibiting the inter planar spacing of the PtRu(111) plane and corresponding fast Fourier transformation pattern. (c) HAADF-STEM image of PtRu@cMOF. (d) Z-contrast image. (e) Cryo-EM images of PtRu@cMOF. Reproduced with permission from ref. 62 Copyright 2021, Wiley-VCH. (f) Formation of nanochannels in the polymer membrane and subsequent confinement of the porous HKUST-1 metal–organic framework. Reproduced with permission from ref. 63 Copyright 2020, ACS.

is suggested that *CO is reduced to *C through the *COH intermediate, and furthermore this reduction is expanded to *CH, *CH$_2$ and *CH$_3$, and lastly CH$_4$ is generated.[79,80] (2) The most favourable route according to experiments and theoretical calculations is *CO → *CHO → *CH → *CH$_2$ → *CH$_3$ → *$^+$CH$_4$.[81]

In addition, the production of multi-carbon products generally follows the *CO intermediate route and the final product decided after the reduction of *CO depends on the experimental conditions.[82,83] For example, after *CH is protonated to *CH$_3$, ethane is generated by the PCET process *via* the *CH intermediate. The *CH$_3$ intermediate produces C$_2$H$_6$ as the final product after dimerization. The addition of CO to *CH$_2$ generates CH$_3$COO$^-$. Also, *CO–CO generates the *CHCH$_2$O intermediate through successive proton and electron transfer, which is the rate-determining step (RDS) to produce ethylene and ethanol.[83,84]

In some of CO$_2$RR experiments, bulk metals have been used for catalysis. According to the results, there is a theoretical trend,[85–91] and bulk metal catalysts are divided into the following categories: (1) formic acid production, for example, Hg, Tl, Cd, Sn, In, Pb, and Bi. (2) Production of CO (Au, Ag, Ga, Zn and Pd). (3) H$_2$-Producing metals, *i.e.*, Fe, Ni, Ti and Pt. (4) Copper metal-based electrodes, which are known to produce multi-carbon products.[92–94] According to studies, any electronic change or influence on the active centers can lead to changes in the selectivity and FE of the products. For example, Zn and Cu have the same electronic structures but their catalytic properties are quite different. Specifically, the Zn electrode displays 2e$^-$ reduction and produces CO upon CO$_2$ reduction, while Cu generates multiple hydrocarbons.[95,96] In some other reports, Zn-doped (Zn/Cu) electrodes generated different products, *i.e.*, the production of alcohols.[97,98] For example, a Cu$_4$Zn

Table 1 Standard potentials for the electrocatalytic reduction of CO_2 to the corresponding products[71]

Reduction reaction	Product	R. potential (V vs. SHE)
$2H^+(g) + 2e^- \rightarrow H_2(g)$	Hydrogen	0
$CO_2(g) + e^- \rightarrow CO_2^{\bullet-}$		−1.900
$CO_2(g) + 2H^+(aq) + 2e^- \rightarrow CO(g) + H_2O(l)$	Carbon monoxide	−0.531
$CO_2(g) + H_2O(l) + 2e^- \rightarrow CO(g) + 2OH^-(aq)$	Carbon monoxide	−1.347
$CO_2(g) + 2H^+(aq) + 2e^- \rightarrow HCOOH(l)$	Formic acid	−0.610
$CO_2(g) + H_2O(l) + 2e^- \rightarrow HCOO^-(aq) + 2OH^-(aq)$	Formate	−1.491
$CO_2(g) + 4H^+(aq) + 2e^- \rightarrow HCHO(l) + H_2O(l)$	Formaldehyde	−0.480
$CO_2(g) + 3H_2O(l) + 4e^- \rightarrow HCHO(l) + 4OH^-(aq)$	Formaldehyde	−1.311
$CO_2(g) + 6H^+(aq) + 6e^- \rightarrow CH_3OH(l) + H_2O(l)$	Methanol	−0.380
$CO_2(g) + 5H_2O(l) + 6e^- \rightarrow CH_3OH(l) + 6OH^-(aq)$	Methanol	−1.225
$CO_2(g) + 8H^+(aq) + 8e^- \rightarrow CH_4(g) + 2H_2O(l)$	Methane	−0.240
$CO_2(g) + 6H_2O(l) + 8e^- \rightarrow CH_4(g) + 8OH^-(aq)$	Methane	−1.072
$2CO_2(g) + 12H^+(aq) + 12e^- \rightarrow C_2H_4(g) + 4H_2O(l)$	Ethene	−0.349
$2CO_2(g) + 8H_2O(l) + 12e^- \rightarrow C_2H_4(g) + 12OH^-(aq)$	Ethene	−1.177
$2CO_2(g) + 12H^+(aq) + 12e^- \rightarrow C_2H_5OH(l) + 3H_2O(l)$	Ethanol	−0.329
$2CO_2(g) + 9H_2O(l) + 12e^- \rightarrow C_2H_5OH(l) + 12OH^-(aq)$	Ethanol	−1.157
$3CO_2(g) + 18H^+(aq) + 18e^- \rightarrow C_3H_7OH(l) + 5H_2O(l)$	Propanol	−0.320
$2CO_2(g) + 2H^+(aq) + 2e^- \rightarrow H_2C_2O_4(l)$	Oxalic acid	−0.913
$2CO_2(g) + 2e^- \rightarrow C_2O4^{2-}(aq)$	Oxalate	−1.003
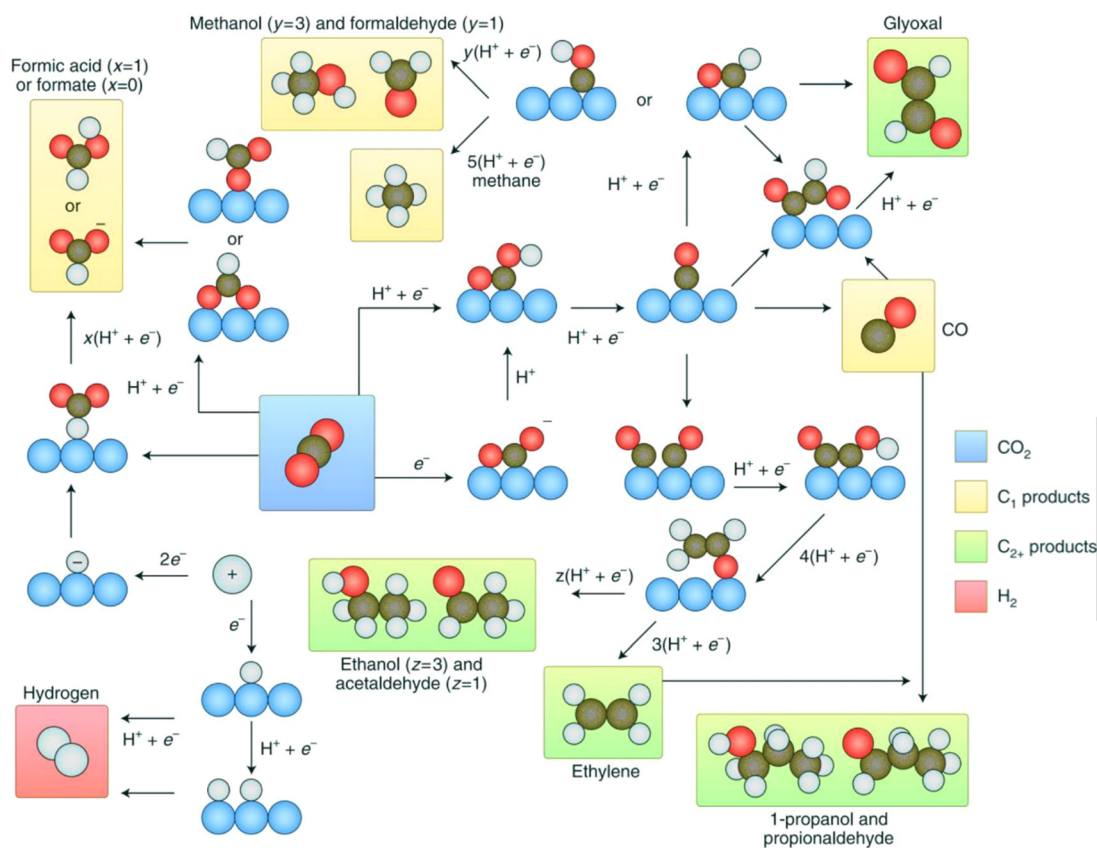
Fig. 5 Reaction pathways of CO_2 to different products. Reproduced with permission from ref. 65 Copyright 2019, Springer Nature.

catalyst produced ethanol with 29.1% FE.[97] Similarly, a mixture of ZnO and CuO (with 0.5 : 1 wt%) produced CH_3OH with an FE of 25.2%.[99] However, Sn-doped Cu did not exhibit a good performance, which may be ascribed to the strong interactions of the intermediate (*CO) with the Cu surface.[100,101] Consequently, the absorbance time of the intermediates on the

catalyst surface is also an important factor to regulate the product selectivity in the CO_2RR process, and it is suggested that the long-term interactions between the designed catalysts and intermediates may possibly generate multi-carbon (C_{2+}) products.[102–107] For example, recently, Song et al. revealed the transition state of the adsorbed intermediate of CO_2 to realize

selectivity for the formation of formic acid on the surface of an S-doped Cu catalyst during the CO_2RR.[107] They confirmed that S can stabilize the reduced Cu center.

In recent years, it has also been suggested that the structural properties of catalytic materials can change the reaction kinetics, products, and selectivity. Accordingly, porous materials have received special consideration because of their special characteristics, for example, enlarged surface area ratio to active centers, adjustable pore size for reactant/product mass transfer, and controllable local pH value.[104,108] He et al. applied the self-assemble strategy to synthesize gradient macro and mesoporous alloys (Cu/Zn). The catalysis outcomes displayed that the Cu_5Zn_8 alloy exhibited a superior performance in reducing carbon dioxide to ethanol with an FE of about 46% and excellent stability for 11 h.[89] SnO_2 and Au show almost the same catalytic performance for the CO_2RR because they possess the same morphology.[106,109] Nam et al. proposed the reaction kinetics for the CO_2RR to multi-carbon products under different morphologies.[102] They applied various copper-based catalytic materials with defined morphologies and revealed that the morphology also plays an active role in accelerating the coupling (C–C) and the stability can be controlled by the flow rate and pH.[102,103] MOF materials generally have highly-tuneable large porosity and huge surface area, which are very important for CO_2RR, and thus they have been extensively studied in recent years. For instance, a 2D Bi-MOF displayed an excellent performance for the CO_2RR (FE for formic acid was 92%)

compared with the reversible hydrogen electrode (RHE), with stability for 30 h. The specific mass ratio of formic acid was as high as 41.0 mA Mg_{Bi}^{-1} and better than that of the commercially available Bi sheets and Bi_2O_3.[110]

4.2 Thermodynamics

CO_2 bond cleavage requires an active catalyst for the conversion of CO_2 to fuels and chemicals.[113] The CO_2 molecular orbital (MO) diagram, showing a fully interconnected and formed orbital, demonstrates that CO_2 is a stable substance (Fig. 6a).[111] In the first step to activate CO_2 molecules, the transfer of electrons occurs (i.e., the reduction process), which have LUMO $\sigma*$ to counter binding. Also, the HOMO takes the high electron density, which is localized as the lone pair on the oxygen plane, favouring the interaction with the electrophilic molecule. Accordingly, the bond length of C–O is enhanced, which is displayed as the first tilt in the linear molecule. The electrophilic and nucleophilic molecules can easily attack to the curved molecule through their charged local orbital boundaries. Nonetheless, the electronic reduction of CO_2 to CO_2^- is an intricate pathway and requires high overpotentials (Fig. 6b and c).[112] Because of the big barrier between the bent anion and linear-shape molecule, the subsequent step, specifically, PCET, is thermodynamically more favourable than the first step (Fig. 6d).[65,114,115]

As designated in Fig. 6b and d, the transfer of 2, 4, 6, 8 or 12 electrons and protons during the CO_2RR process leads to the
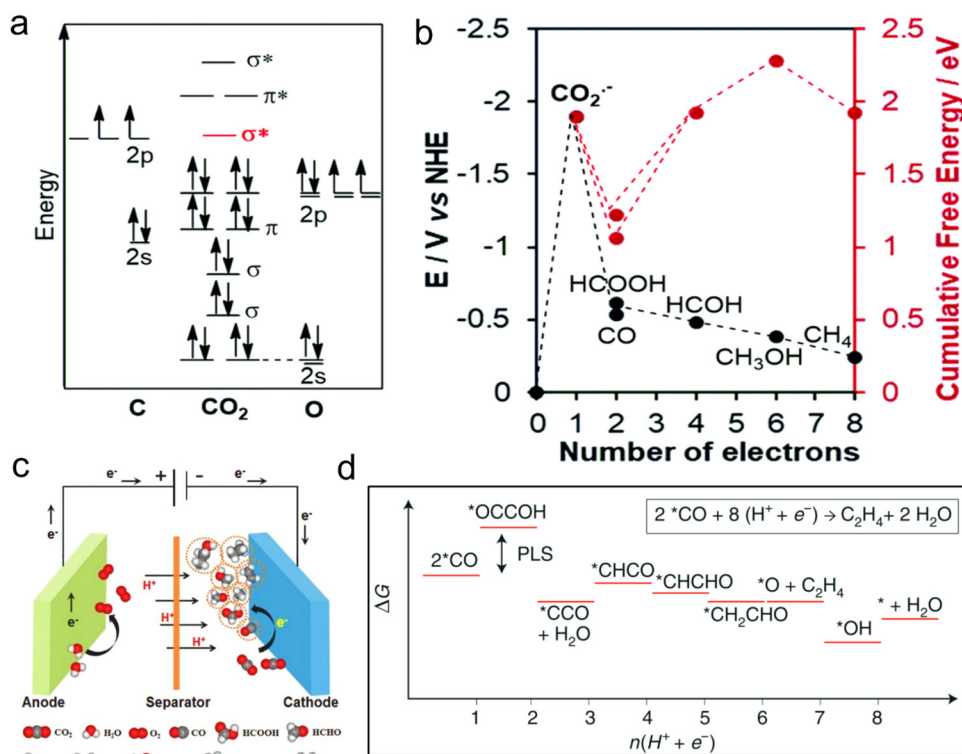
Fig. 6 (a) CO_2 molecular orbital (MO) diagram. (b) Thermodynamic of required activation energy to final product. Reproduced with permission from ref. 111 Copyright 2020, RSC. (c) Design of the cell for the conversion of CO_2. Reproduced with permission from ref. 112 Copyright 2018, Wiley. (d) Free-energy diagram with favourable reaction path for CO_2 to C_2H_4 on Cu surface. Reproduced with permission from ref. 65 Copyright 2019, Springer Nature.

formation of various products. The generation of different as well as specific products during the CO_2RR process, for example, mono and multi-carbon products, mainly depends on the reaction conditions (electrolyte, overpotential, pH and design of the device) and nature of the catalyst (metal type and distribution of active centers). Many types of products are generated in the catalytic process, but one will be produced that is thermodynamically competitive with the others. Thus, the selectivity for the production of the target product is one of the important standards to evaluate the CO_2RR performance.

5. MOFs for the CO_2RR

The apparent performance of electrocatalysts is greatly affected by the electrode preparation process. However, the traditional electrode preparation methods such as drop coating usually result in low apparent activity. Alternatively, the *in situ* synthesis of MOFs on the electrode is expected to give full play to the intrinsic activity of the material. Zhu *et al.*[116] reported the strategy of *in situ* electrosynthesis of a hollow copper-MOF and reduction to multi-stage Cu dendrite catalyst during the reaction. The preparation of thew Cu-MOF film only took 5 min. The Cu dendrite catalyst obtained by this strategy possessed a large surface area and open active sites, which are conducive to the CO_2RR to $HCOO^-$ in ion–liquid electrolyte. The current density of the above-mentioned system was 102.1 mA cm^{-2} with an FE of 98.2%. Kang *et al.*[117] used copper foam as the substrate and ligands with large steric hindrance to control the growth kinetics of an MOF, producing Cu-MOF with a large number of defects, *i.e.*, (Cu₂(L)) (H₄l = 4,4′,4″,4‴-(1,4-phenylene)bis(pyridine-4,2,6-triacyl)) tetrabenzoic acid, which rapidly grew on the copper foam in acetonitrile ionic–liquid electrolyte to produce formate with an FE of 90%. The Cu^{2+} defect has strong binding ability to CO_2 and mainly coordinates with the oxygen in CO_2 in the form of O–Cu–O because the formation of Cu-MOF*OOCH is easier than Cu-MOF*COOH, leading to higher selectivity for formic acid. The high-density Cu^{2+} defects also generated formic acid at lower overpotentials, thus weakening other competitive reactions such as Cu^{2+} reduction and hydrogen generation.

Kang *et al.*[118] successfully deposited MFM-300 (In) on In foil within 10 min using an acetate ionic liquid as the electrolyte. The MOF prepared using this method had strong binding force with the electrode metal substrate, and the particles were evenly dispersed, which effectively enhanced the charge transfer efficiency in the reaction process. Compared with other MOFs and oxides, MFM-300 (In) is more stable and can maintain its structural integrity at a negative potential without being reduced to In. Besides, the FE of formate produced by the MFM-300 (In)/In electrode was as high as 99.1% due to the presence of defect sites and strong interactions with CO_2. Compared with the MFM-300 (In)/carbon paper electrode prepared by the traditional thermal synthesis method, it could generate more $^\bullet$COOH radicals, thus promoting the efficient synthesis of formic acid.

The type and states of ligands also have a significant influence on the electrocatalytic activity of MO-based catalysts. Dou *et al.*[119] reported an approach to improve the catalytic activity of MOFs for CO_2 reduction by ligand doping. The electron donor 1,10-phenanthroline was doped in activated ZIF-8, promoting the charge transfer and endowing the sp^2 hybrid atoms in the adjacent imidazole ligands with more electrons, making it easier to generate *COOH, and thus improving the catalytic activity and FE for CO production.

Conductive materials are beneficial for charge transfer and will show great advantages in electrocatalysis. Therefore, the development and application of cMOFs have become a research hotspot. Yi *et al.*[59] prepared conductive phthalocyanine-based 2D nanosheets denoted as MOF-NiPc@NiO₄ using nickel pyrocatechol (Fig. 2b), which efficiently converted CO_2 to CO with an FE of 98.4% under a CO partial current density of 34.5 mA cm^{-2} (Fig. 2d). Compared with the NiO₄ node, the CO_2RR is more likely to occur on the nickel phthalocyanine center (NiPc) because the adsorption energy of CO_2 on NiPc (0.23 eV) is higher than that of the NiO₄ node (0.02 eV), which makes it easier to bind with NiPc, and the electron content of nickel in NiPc is greater than that in NiO₄. When the CO_2 molecule moves from NiPc to the NiO₄ node, the LUMO shifts from −4.22 eV to −4.62 eV, which indicates that NiPc has better reducibility, and thus enables the catalyst to show higher selectivity and activity.

Majidi *et al.*[122] constructed a 2D copper-based cMOF, *i.e.*, copper tetrahydroxyquinone (Cu-THQ) nanosheet. In a mixed electrolyte (1 M (CH₃)₃N(Cl)CH₂CH₂OH and 1 M KOH), the CO_2RR could be accomplished at a low overpotential of 16 mV, showing excellent catalytic activity. At an applied potential of −0.45 V, the current density was about 173 mA cm^{-2} and FE_{CO} was about 91%. In addition, the MOF can provide a good fixing platform for organic molecules with intrinsic electrocatalytic activity, and thus a large number of molecular catalysts can be fully contacted with the electrode, resulting in various advantages for heterogeneous catalysis. Hod *et al.*[123] used electrophoresis technology to immobilize an Fe porphyrin molecular catalyst on the electrode surface on the Fe-MOF-525 platform. Simultaneously, the Fe porphyrin molecule was not the only catalytically active material, but also the ligand of the MOF acted as a bridge to connect the electrode and the outer catalytically active sites. Based on the porous platform provided by the MOF, the amount of effective electrochemically active centers on the catalyst surface increased to about 1015 cm^2, which is nearly 3 times higher than the active site concentration obtained by direct monolayer-loaded Fe porphyrin molecules and nearly 1-fold higher than the reported maximum concentration of loaded molecular catalyst. In this system, the product of CO_2RR is an equal mixture of CO and H_2 with an FE of close to 100%. This work reflects the innovative application of MOFs due to their regular and ordered pore structures in the immobilization of molecular electrocatalysts. Furthermore, Table 2 presents a comparison of the state-of-the-art results for MOFs in the CO_2RR.

Table 2 The performance of different MOFs and their related products in the CO_2RR

Material	Main product	Electrolyte	Faradaic efficiency [%]	Potential	Current density [mA cm^{-2}]	Ref.
Bi MOF	HCOOH	0.5 M KHCO$_3$	95.5	−0.86 V vs. RHE	−11.2	124
ZIF-8	CO	0.5 M NaCl	65.5	−1.8 V vs. SCE	NA	125
ZIF-8	CO	0.25 M K$_2$SO$_4$	81	−1.1 V vs. RHE	6.9	126
ZIF-108			NA	−1.3 V vs. RHE	12.8	
ZIF-A-LD	CO	0.1 M KHCO$_3$	90.57	−1.1 V vs. RHE	NA	127
HKUST-1(Cu, Ru)	C$_2$H$_5$OH CH$_3$OH	0.5 M KHCO$_3$	47.2	NA	20	128
Cu@MOF	HCOOH	0.1 M NaClO$_4$	28	−0.82 V vs. RHE	−1.2	129
Cu$_2$O@Cu-MOF	CH$_4$	0.1 M KHCO$_3$	63.2	−1.71 V vs. RHE	8.4	130
Ag$_2$O/layered ZIF	CO	0.25 M K$_2$SO$_4$	80.6	−1.2 V vs. RHE	26.2	131
RE-ndc-fcu-MOF @AuNMEs	CH$_4$	0.1 M KHCO$_3$	0.5 ± 0.1	−0.5 V vs. RHE	−2.5	132
Cu(bdc)·xH$_2$O @AuNMEs			1 ± 0.4		−1.7	
ZIF-8@AuNMEs			0.9 ± 0.2		−0.1	
Al$_2$(OH)$_2$ TCPP@AuNMEs	C$_2$H$_4$		1.1 ± 0.4		−3.1	
Co porphyrin MOF	CO	0.5 M K$_2$CO$_3$	76	−0.7 V vs. RHE	NA	133
Fe-MOF-525/FTO	CO + H$_2$	1 M TBAPF$_6$	100	−1.3 V vs. NHE	5.9	123
Zn-BTC MOF/CP	CH$_4$	BmimBF$_4$	80.1 ± 6.6	−2.2 V vs. Ag/Ag$^+$	3.1 ± 0.5	134
		BmimOTf	85.4 ± 3.2		2.1 ± 0.3	
		BmimPF$_6$	87.7 ± 5.1		1.6 ± 0.3	
		BmimClO$_4$	88.3 ± 3.8		0.5 ± 0.2	
Re MOF/FTO	CO	0.1 M TBAH in CH$_3$CN + 5% trifluoroethanol	93 ± 5	−1.6 V vs. NHE	2.5	135

5.1 Role of central metal atoms

Usually, for the CO_2RR to occur, it is assumed that a cathode potential is required, and most likely, the central metal atom acts as the active site for the CO_2RR. Thus far, most of the used electrocatalysts in the CO_2RR work as pre-catalytic converters. In the catalytic process, the central metal atom is oxidized or reduced, which is why it is difficult to distinguish the actual active site before the catalytic process.[120] For example, in the case of transition metals, CuO-driven Cu has been extensively studied for the CO_2RR because of its high selectivity. Correspondingly, in Cu-based MOFs, Kumar et al.[136] detected different $Cu(I)/Cu(II)$ and $Cu(0)/Cu(I)$ as well as reversible redox reactions during cyclic voltammetry in 0.1 M KCl using a glassy carbon electrode coated with a Cu–BTC thin film. Chang et al.[120] elaborated the transition phase of Cu-based electrodes using in situ XAS and explored their oxidation state together with local structure. The synthesis of Cu-based materials with Cu(0) is advantageous to produce multi-carbon products of the CO_2RR rather than Cu(I), whereas the competitive oxidation reaction of Cu(0) decides the products and chemically active sites of CO_2RR. Furthermore, in situ Raman was performed, confirming that the re-oxidation reaction determines the chemical state of Cu, as shown in Fig. 7a and b. In addition, Sargent et al.[121] used in situ XAS to inspect the percentage of copper at different potentials (Fig. 7c and d). Additionally, they proposed a noteworthy relationship between the product distribution and the surface state of copper and noted the existence of copper-stabilized ethylene intermediates. Furthermore, Yaghi et al.[133] explored the active oxidation states of other transition metals, e.g., they investigated the oxidation states of Co in a Co-MOF during the CO_2RR using in situ techniques. This study displayed that most of the metal centers are available for redox reactions, where Co(II) is reduced to (I), and revealed that Co reduction is the first step in the reduction

process. During the CO_2RR process, the reduction of Co(II) to Co(0) is due to the adsorption of CO_2 on the surface of the active center. However, this type of transition does not occur on MOF-derived metal active centers. Recently, Hu et al.[137] reported the exceptional FE and low overpotential of an iron-based single-atomic catalyst (SAC) for CO. In addition, in situ XAS analysis indicated that the active Fe^{3+} species coordinated with the pyrrolic-N atom, which can maintain its +3 oxidation state during the electrocatalysis process. Furthermore, on MOF-74 impregnated with cobalt, nickel and zinc, the role of the metal center was also experimentally determined, where at −0.91 V vs. RHE, CO_2 was reduced to 78.3% of H_2 and 15.4% CO, which suggests that this heterogeneous catalyst can produce syngas efficiently.[138] In addition, inorganic modification was performed to determine its effects on the selectivity and activity of Zn-MOF catalysts for the CO_2RR. Wang et al.[139] designed many zinc (ZIF-8)-based materials using different sources for Zn as reactants and studied the CO_2RR process. The electrochemical findings showed that the ZIF-8 prepared using a $ZnSO_4$ source exhibited a better catalytic performance for the CO_2RR with a high FE of 65% and current density of 3 mA cm^{-2}, giving new insight into the relationship between activity for the CO_2RR and the zinc source, and it is appealing that the vital active centers are discrete zinc nodes. The boost in the activity and selectivity of Zn-MOF in the presence of SO_4^{2-} ions is mainly ascribed to the interaction between the Zn node and SO_4^{2-} ions, which can contribute to the exchange of the anion for charge balance on the oxidation of the Zn nodes. However, some reported works showed that the Zn metal sites of Zn MOFs are not the active sites for the catalysis process because of their fully filled of d-orbital.[140–142] Bao et al.[140] explored and confirmed the imidazole coordination with Zn in ZIF and that it serves as the catalytic center for the CO_2RR using DFT calculations and in situ XAS. Therefore, the definite
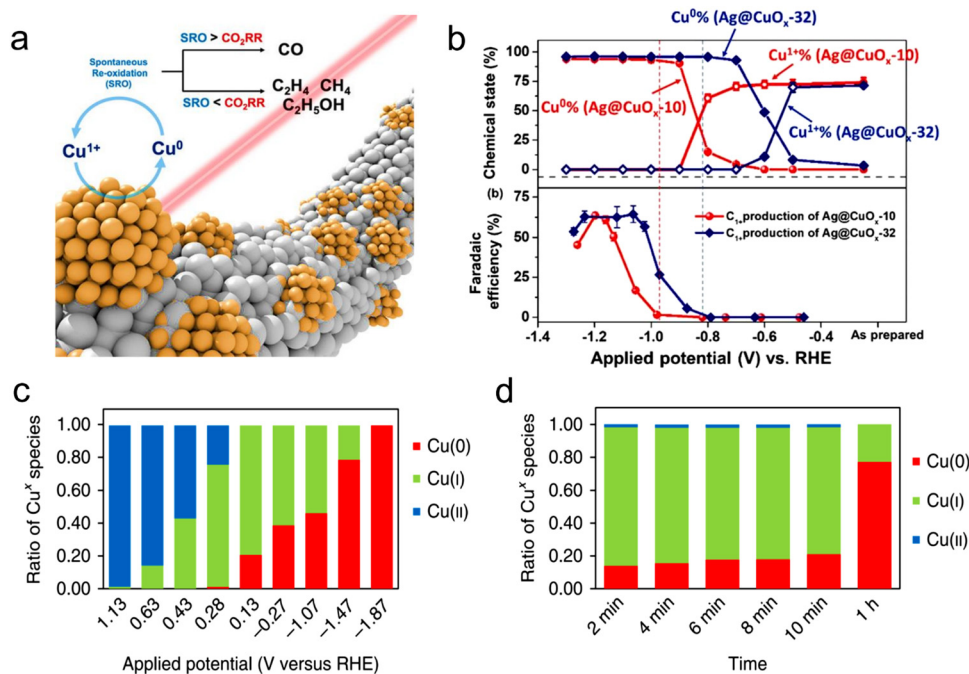
Fig. 7 (a) Schematic process of Cu during the CO_2RR. (b) FE and chemical state *vs.* applied potential. Reproduced with permission from ref. 120 Copyright 2019, ACS. (c) Oxidation state ratio of Cu *vs.* applied potential. (d) Oxidation state ratio *vs.* time. Reproduced with permission from ref. 121 Copyright 2018, Springer Nature.

active center in MOFs is quite controversial, and thus further in-depth research is needed to answer this question. In this case, operando or *in situ* studies play an important role in the dynamic process of the electrocatalytic process, which can recognize the definite active centres and support the understanding of the reaction mechanism. However, with the help of powerful *in situ* technology, it is still necessary to develop next-generation catalysts.

5.2 Role of organic linkers

The presence of ligands can change the catalytic performance of MOFs. For example, ligands with electron-donating ability can increase the catalytic activity of MOFs by inducing electrons to move from the active site to the anti-bonding orbital of CO_2, thereby generating *COOH through proton coupling.[119] Based on this, numerous works have been performed to check the influence of the surrounding ligands on the CO_2RR process. Here, in this part, we reflect the microscopic and macroscopic influence of ligands on the catalytic performance of metal complexes and MOFs. The effect of ligands on the CO_2RR product was demonstrated in the ground-breaking work of catalysis. It is worth noting that different Cu-MOFs generate different CO_2RR products in the reduction process, which is due to the presence of different ligands connected to the same metal center.[136,143] Kumar *et al.*[136] used a ligand with an O donor atom, and consequently the CO_2RR product was oxalate. Hinogami *et al.*[143] designed an MOF containing S and N donor atoms and the CO_2RR product was formic acid. Actually, the ligands and their donor atoms change the electronic

configuration of the central active metal atom, resulting in different CO_2RR products.

To confirm this influence, four different copper-MOFs were synthesized, as follows: (1) copper AdeAce, (2) HKUST-1, (3) metal organic aerogel of mesoporous Cu-DTA, and (4) CuZn-DTA, and sprayed on GDE.[144] The measured cumulative (methanol and ethanol) FE for the CO_2RR was 15.9% using the HKUST-1 electrode at a current density of 10 mA cm^{-2}. It was observed that the MOFs having unsaturated metal sites can contribute to CO_2 reduction to alcohol. Furthermore, HKUST-1 displayed a stable output load for 17 h. Therefore, MOF catalysts are very flexible catalysts due to their tuneable features especially for CO_2RR catalysis because of the excellent adsorption property for CO_2 gas, which enhances the interaction between CO_2 and the active sites of the catalysts. Jiang *et al.*[140] synthesized the ZIF-8 MOF, which is a typical MOF material, and confirmed that the coordination between the imidazole ligand and Zn(II) acts as the active center for the CO_2RR, which was confirmed by XAS and DFT calculations. In addition, they studied the topology structure of other ZIFs but with different organic linkers, for example, SIM-1 and ZIF-7, -8, and -108 for the CO_2RR. Remarkably, among the catalysts, ZIF-8 showed a progressive FE_{CO} of 81%. Porphyrin-based Fe catalysts are high-efficiency homogeneous catalysts, which were first synthesized by Savéant *et al.*,[145] and subsequently used for the CO_2RR.[146–148] Considering the constant use of Fe porphyrins, porphyrin-based constituents are introduced in MOF structures for two scientific purposes, as follows: (1) MOFs have potential electrocatalytic use and electron transfer capabilities, which are crucial for the CO_2RR and (2) the catalytic
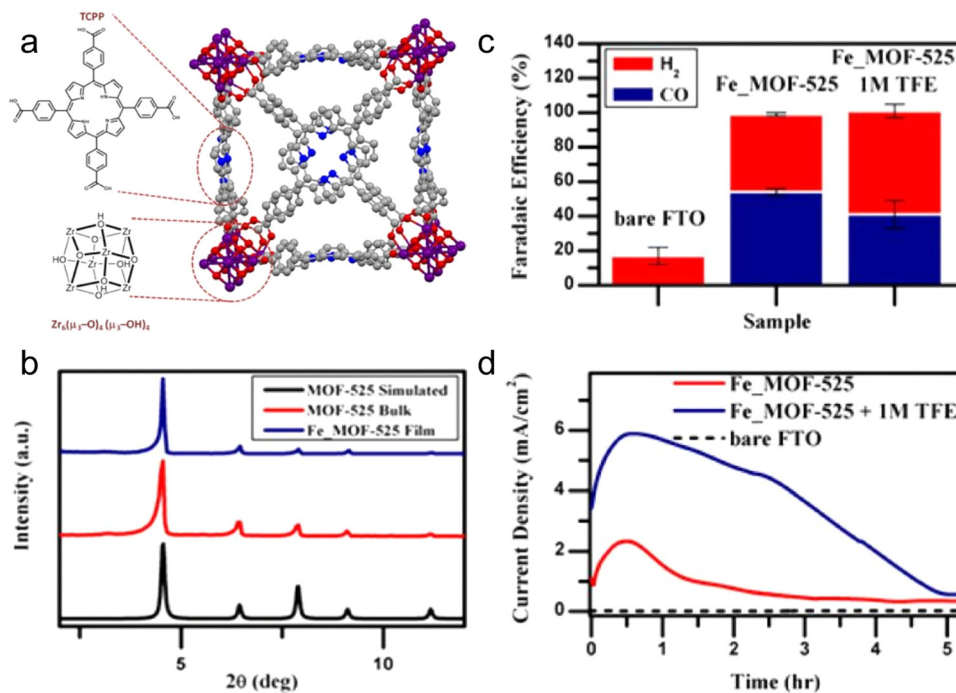
Fig. 8 (a) Crystal structure of MOF-525 including the chemical structure of Zr-based node. (b) Comparison of PXRD of Fe-MOF-525 and other MOFs. (c) FE. (d) Current density *vs.* time. Reproduced with permission from ref. 123 Copyright 2015, ACS.

structure is modified by introducing active molecules having characteristics including adjustable porosity, surface controllability, chemical stability, and access to active sites.[149] For instance, Hod *et al.*[123] combined an Fe-porphyrin with MOF-525 and applied it as a CO$_2$RR catalyst, and confirm its structure by XRD (Fig. 8a and b). During the CO$_2$RR process, a mixture of H$_2$ and CO (FE$_{CO}$ of 50%) was produced. These results indicate that Fe–porphyrins bound to the surface of MOFs can be used for the CO$_2$RR (Fig. 8c and d). In addition, it has been observed that the porphyrin ring-coordinated Co atom is also a catalytically active site for the CO$_2$RR. For example, Yaghi *et al.* designed a Co-based MOF with porphyrin as the organic linker, which was named as Al$_2$(OH)$_2$TCPP-Co, for the CO$_2$RR.[133] Consequently, an improved current density and catalytic performance of FE$_{CO}$ 76% were achieved, and it was demonstrated that Co is the active center. Furthermore, they stated that the metal center of Co(II) is not actually the active center, instead Co(I) is the active center for the reduction of CO$_2$.[133] These preliminary investigations show that the electrocatalytic performance of MOFs for the CO$_2$RR can be adjusted by changing their ligand.

5.3 Role of metal–ligand bonding

In addition, MOFs have the ability to resist the chemical environment for a long time. Actually, their chemical stability is very important for electrochemical reactions, which depends on the metal-linker bonding strength of the MOFs. Generally, the thermal and mechanical stability of MOFs are related to their capability to maintain their structural integrity when exposed to vacuum, pressure or heat.[150] Because MOF-based

materials are widely applied in the electrocatalytic process of different pH value electrolytes, their stability in a wide pH range is very important. For instance, it was reported that the highly stable Bi-MOF is an effective catalyst for the CO$_2$RR process, which can yield formate with an FE of 92.2% and stability for 30 h. Moreover, a current density of 14 mA cm^{-2} was achieved under the low overpotential of 0.61 V. Further, *in situ* and *ex situ* XAFS were employed to study the structure-related features of Bi-MOF to reserve Bi^{3+}, representing the chemical stability of Bi-based MOFs.[110] Subsequently, Zhang *et al.* synthesized and studied a Bi-BTC MOF for the CO$_2$RR *via* the simple hydrothermal process. They reported that Bi-BTC is an active catalyst for the production of HCOO$^-$ with an FE of 92 $\pm$ 3%. Interestingly, the FE was observed to be 90% after a long stability test of 12 h, which can be ascribed to the electrochemical stability of the MOF material.[124] Yang *et al.*[133] reported that Co–porphyrin has a better initial performance for the CO$_2$RR with an FE of 76% at 0.7 V, but they reported the stability performance only of 7 h. Similarly, a zirconium-based MOF (MOF-525) containing Fe–porphyrin was used as an electrocatalyst for the CO$_2$RR, where the stability of the MOF declined within 4 h, indicating its unsatisfactory stability.[123] Although numerous studies synthesized novel MOFs with good stability using different synthesis methods, further expanded studies are needed to improve the stability of MOFs and systematically elucidate the degradation of the catalyst. In this case, more operando characterizations are needed to examine the electronic structural composition and morphological features.

6. MOF-based composites

As is known, pristine MOFs possess low conductivity, and thus MOF-based composites with other materials (for example, metal, graphene, metal oxides and conductive carbon) are commonly used for the CO_2RR. Yi et al.[151] developed in situ uniformly distributed $Cu_2O(111)$ quantum dots on a porous conductive copper-based MOF. Because the catalyst has rich hydroxyl groups and uniform active sites (Fig. 9), it could efficiently reduce CO_2 to methane. During this process, the hydroxyl group on the MOF can form a hydrogen bond with intermediate products such as *COOH, *CHO, and *CO, while its uniform active sites can reduce the occurrence of side reactions, thus effectively improving the selectivity for methane. The in situ-formed $Cu_2O@Cu$-MOF having abundant active centers showed strong CO_2 adsorption capacity. In the case of MOF composites, the MOF provides high stability and porosity, and transfers the scaffold in a limited space to achieve size-selective catalysis.

6.1 Polyoxometalate@MOF

In polyoxometalates (POMs), polyhedrons of metal oxides, MO_x (x = 5, 6), are the basic unit and composed of polyanions of polyoxometalate and metal cations. The transition metal cations present in POMs usually have a high valence state, such as Mo_{VI}, W_{VI}, Ta_V, Nb_V, and V_V. As a typical class of cluster compounds, POMs have been extensively studied in catalytic applications.[152–154] Exploiting the excellent characteristics of POMs, including redox ability, clear active center, adjustable light absorption, and reversible electron acceptor and donor, POM materials can be applied as photocatalysts, photosensitizers, co-catalysts and multi-electron sources for the CO_2 reduction process.[155–161] By integrating POMs in the MOF

channels, they can promote electron transport, and ultimately improve the catalytic performance of the active centers. For instance, Lan et al.[162] designed POM@PCN-222(Co) by linking a rich-electron POM structure with an MOF with a large specific surface area (Fig. 10). Surprisingly, the composite (H-POM@PCN-222(Co)) displayed significantly improved electron transfer ability and showed an excellent CO_2RR performance with FE_{CO} of 96.2% at −0.8 V vs. RHE, and stability for up to 10 h. Fig. 11 shows the structure, synthesis, and reduction activity of CO_2 of (PW12, Cp*Rh)@UiO-67, in which a simple strategy was used to fix the POM in the voids of the MOF, and after the encapsulation of the $Cp*Rh(bpydc)Cl_2$ complex was done through the linker exchange post-synthesis.[163] The catalytic activity of the composite was evaluated in the reduction of CO_2 to formate. Compared with Cp*Rh@UiO-67 without the POM, the TON increased to high extent of 175 and the yield also doubled. The reference POM is considered as an electronic transfer material, but it does not impact on the electronic structure of the complex. In addition, $[BW_{12}O_{40}]^{5-}$, $[SiW_{12}O_{40}]^{4-}$, $[PMo_{12}O_{40}]^{3-}$ and $[PTi_2W_{10}O_{40}]^{7-}$ with different redox potentials and acidities are also appealing for further studies.

6.2 Metal oxide@MOF

It is very attractive to integrate copper oxide nanoparticles with the conductive network of MOFs, and the resulting electrocatalyst can display good catalytic activity. Accordingly, a Cu-based MOF (CuHHTP) with 2D conductive network was designed as the precursor material for the construction of quantum dots of $Cu_2O(111)$ on the porous surface of CuHHTP via an in situ strategy (Fig. 9). Operando IR spectroscopy and DFT calculations confirmed that $Cu_2O(111)$ can generate and stabilize $*CH_2O$ and $*OCH_3$, which are the key intermediates of
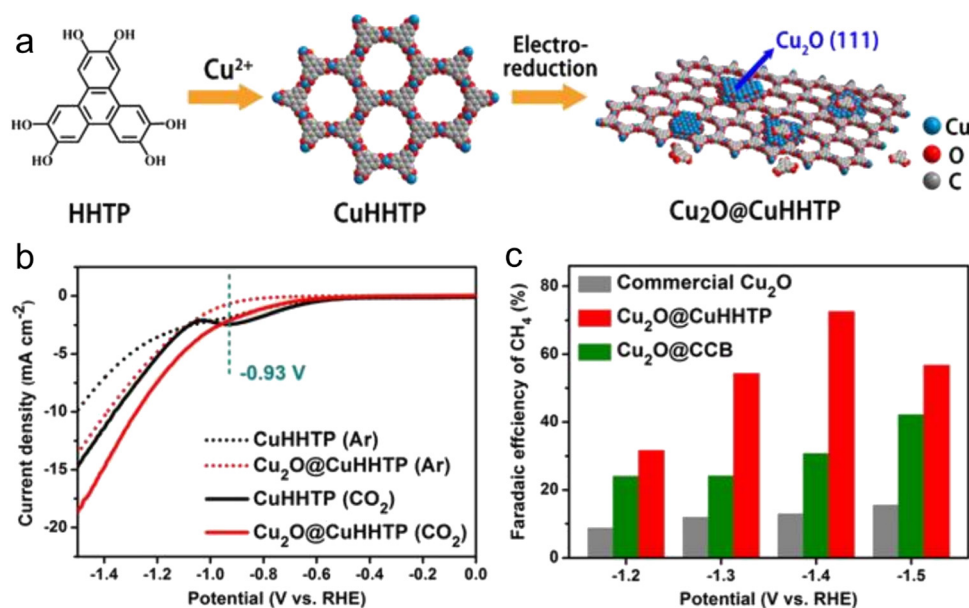

Fig. 9 (a) Design of $Cu_2O@CuHHTP$ through electrochemical treatment. (b) LSV curves. (c) FE comparison. Reproduced with permission from ref. 151 Copyright 2020, Wiley-VCH.
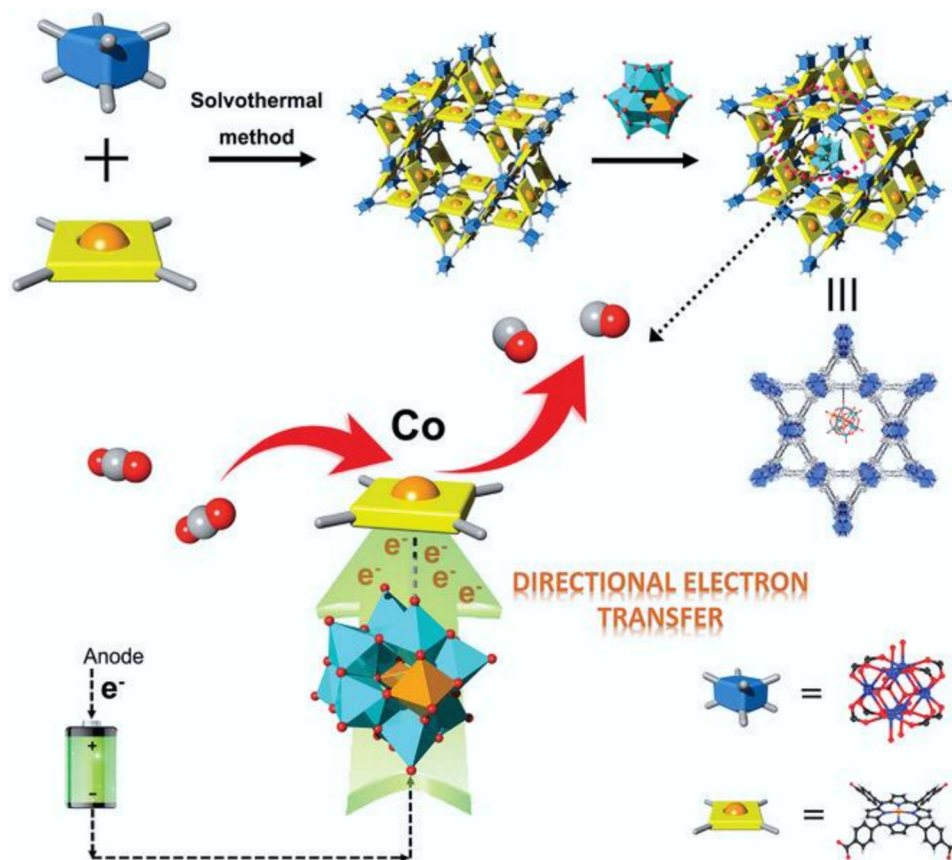
Fig. 10 Top: Schematic of the synthetic process and detailed structure of the POM@PCN-222(Co) composite. Bottom: Proposed electron transfer scheme on the active single-metal site Co of H-POM@PCN-222(Co) for the CO_2RR (Keggin-type POM builds an electron-transfer channel to the Co center from the electrode and accelerates this multi-electron-transfer process to enrich the electron density of the active Co center). Blue box: Zr-based second building unit, yellow square: TCPP linker, and yellow ball: Co metal center. Reproduced with permission from ref. 162 Copyright 2021, Wiley.

the CH_4 reaction path by Cu_2O, and hydrogen bonds. The FE_{CH_4} was high as 73%. The CuHHTP carrier with high conductivity could promote the electron transfer, resulting in a high current density.[151]

6.3 Conductive support@MOF

The inherent low conductivity of MOFs greatly limit their electrochemical activities and applications. Accordingly, the decoration of MOFs on a conductive support improves their overall conductivity, and thus electrochemical activity toward the CO_2RR. For instance, an MOF-55 Al–porphyrin containing cobalt porphyrin as the active center for the CO_2RR to CO was reported. The conductive alumina film was formed via the atomic layer deposition (ALD) method, which can also work as a metal precursor, and then the MOF was generated by reacting the coated alumina with a linker (Fig. 12a).[133] The thickness of the precursor could be simply controlled by the number of deposition cycles, which could adjust the thickness of the catalyst coating. The catalytic activity of the synthesized MOF was mainly enhanced by exploiting the thickness of the catalyst. The optimum catalyst with the thickness of 5 nm showed an FE_{CO} of 76% during the 7 h durability test

(Fig. 12b and c). In addition, Wu et al.[164] introduced a new strategy using FTO as a conductive support for the preparation of $Cu_2F(CuTCPP)$ MOF nanosheets, and the resulting catalyst displayed an improved performance for the CO_2RR, generating formate with 68.4% FE at 1.55 V vs. Ag/AgCl (Fig. 12d). Sun et al.[165] prepared highly oriented MOF films on FTO via liquid-phase epitaxy. The zinc acetate solution in ethanol and $Re(CO)_3C1$ solution in ethanol were successively sprayed on the surface of FTO with a spray gun containing nitrogen, and a layer of film was prepared. Spraying was repeated 30 times to obtain 30 layers of Re-MOF film (Fig. 13a–d).

In the CO_2RR process, porous structures are conducive to the entry of CO_2 dissolved in the organic solvent and the reaction with the inner catalyst, improving the effective active area of the Re-MOF catalyst. Simultaneously, they are also conducive to the escape of CO and H_2 generated during the catalytic process, thus preventing the generated gas from gathering on the surface of the film to hinder the further reaction of the catalyst. This conductive supported MOF showed an FE_{CO} of about 96%, which can be attributed to the improved charge transfer by the conductive support (Fig. 13e–g). It is remarkable that the durability of the catalyst was low
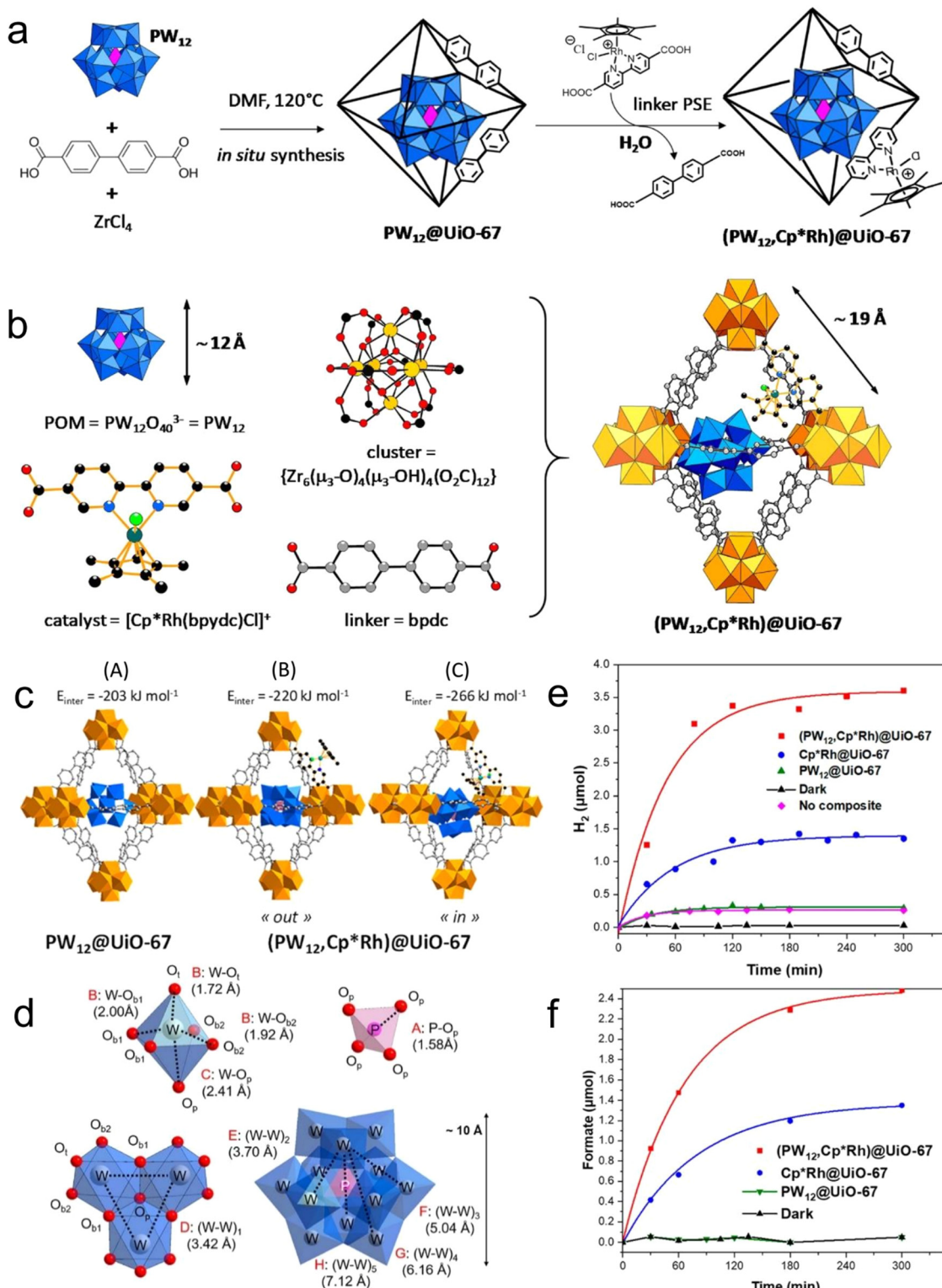
Fig. 11 (a) Schematic of *in situ* synthesis. (b) Components of (PW$_{12}$, Cp*Rh)@UiO-67. (c) Models of PW$_{12}$@UiO-67 and (PW$_{12}$,Cp*Rh)@UiO-67. (d) Distances between the components of POM. Production rate of (e) H$_2$ and (f) HCOO$^-$. Reproduced with permission from ref. 166 Copyright 2020, ACS.

because of its degradation (Re(CO)$_3$C1), and thus it is necessary to develop novel strategies to enhance the durability of the catalyst.

6.4 Molecular catalyst@MOF

It is well known that MOFs exhibit a large surface area, which is advantageous for the distribution of the active centers and can

Fig. 12 (a) Illustration of metal center, linkers, and functional groups and building unit in electrochemical system for CO_2 reduction. (b) Stability of the MOF catalyst evaluated through chronoamperometric measurements in combination with faradaic efficiency measurements. (c) FEs. Reproduced with permission from ref. 133 Copyright 2015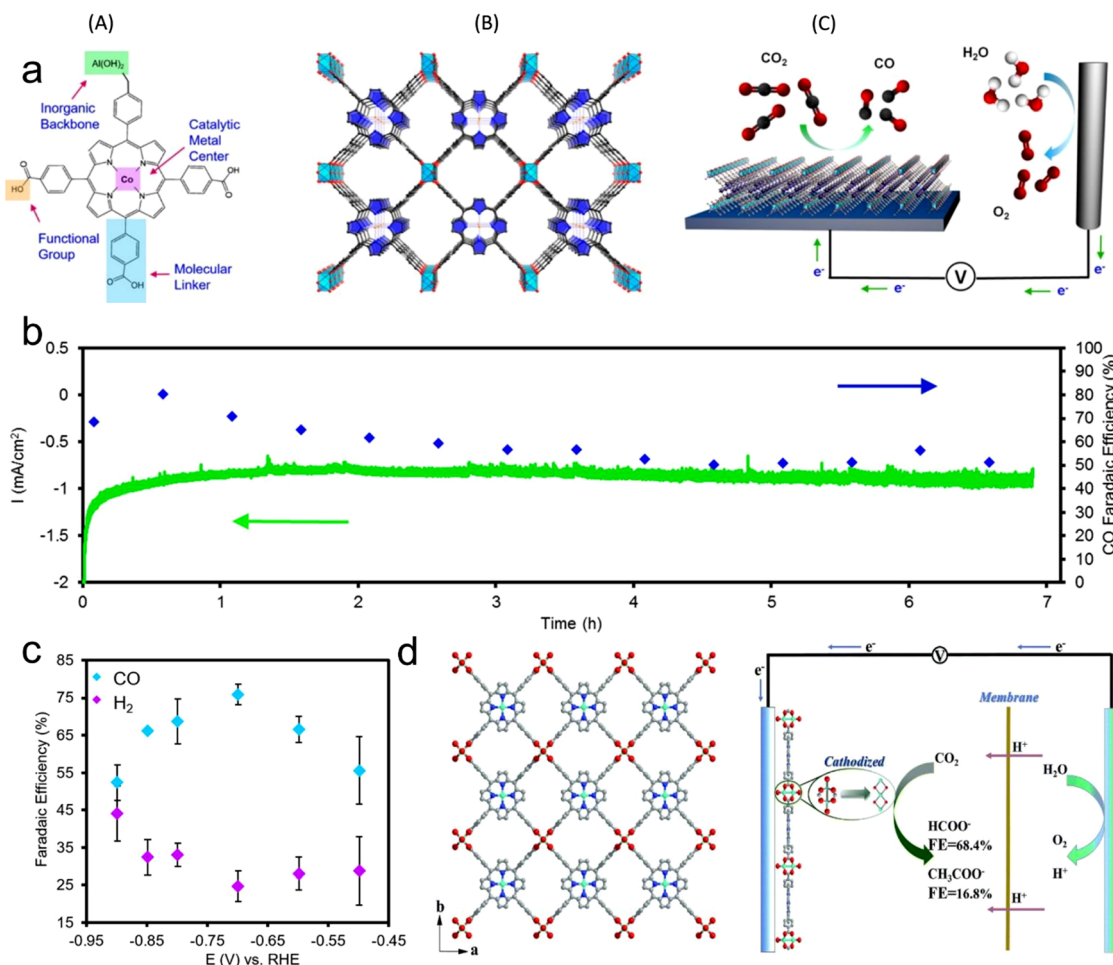, ACS. (d) Crystalline structure of $Cu_2(CuTCPP)$ nanosheets in CO_2 electrochemical reduction system. Reproduced with permission from ref. 164 Copyright 2019, RSC.

enhance the CO_2 transportation and charge, resulting in improved CO_2RR activity. Buonsanti et al.[167] proposed that CO_2 can be actively converted to CO using a mixed catalyst platform, for example, an MOF (Al-PMOF) was combined with colloidal crystals (Ag@PMOF). This study claimed that the hybrid material has greater ability to inhibit the HER than the single silver nanocrystal, and also contributes to the CO_2RR. In addition, the electronic properties were also enhanced by the synergistic effect of the silver colloidal crystals and Al-PMOF and by partially removing the MOF ligands. Furthermore, Lan et al.[168] also reported that the catalytic performance of a cobalt porphyrin increased to 99% FE_{CO} by the synergistic combination effect with POM in $KHCO_3$ (0.5 M) electrolyte (Fig. 14a and b). Through theoretical calculations (DFT), it was confirmed that the free energy of adsorption for *COOH and *CO (intermediate products) is small, further confirming the superior activity of Co-PMOF for the CO_2RR (Fig. 14c and d). Based on the previous perception, these findings verify that the cobalt atom in Co–porphyrins is the main active center, and POMs with

electron-rich aggregates are helpful to boost the electron transport (Fig. 14e and f).

In addition, Wang et al.[169] constructed a catalyst (TPY-MOL-CoPP) with pyridine and CoPP center group on an MOL layer, and assumed that TPY and CoPP have a synergistic effect. To verify this view, the authors prepared a catalyst without pyridine (BTB-MOL-CoPP) as a control. The electrochemical performance showed that at −0.86 V, the CO current density (j_{CO}) of BTB-MOL-CoPP was 923 mA mg^{-1}, and its j_{CO}/j_{H_2} ratio was 2.7, while the j_{CO} of TPY-MOL-CoPP was 1314 mA mg^{-1}, the j_{CO}/j_{H_2} ratio was 11.8, and the CO Faraday efficiency of TPY-MOL-CoPP was 92.2%, indicating that TPY-MOL-CoPP containing pyridine groups was more conducive to improving the selectivity and yield in the CO_2RR.

By adding Zn^{2+} or Ca^{2+} to coordinate TPY sites, it was found that the FE_{CO} was significantly reduced from 92.2% to 6% and 8%, respectively. The evaluation of the CO_2RR performance of various porphyrin-based catalysts showed that the activity of TPY-MOL-CoPP was higher than that of the other catalysts. Even at low potentials, the FE_{CO} of TPY-MOL-CoPP was higher
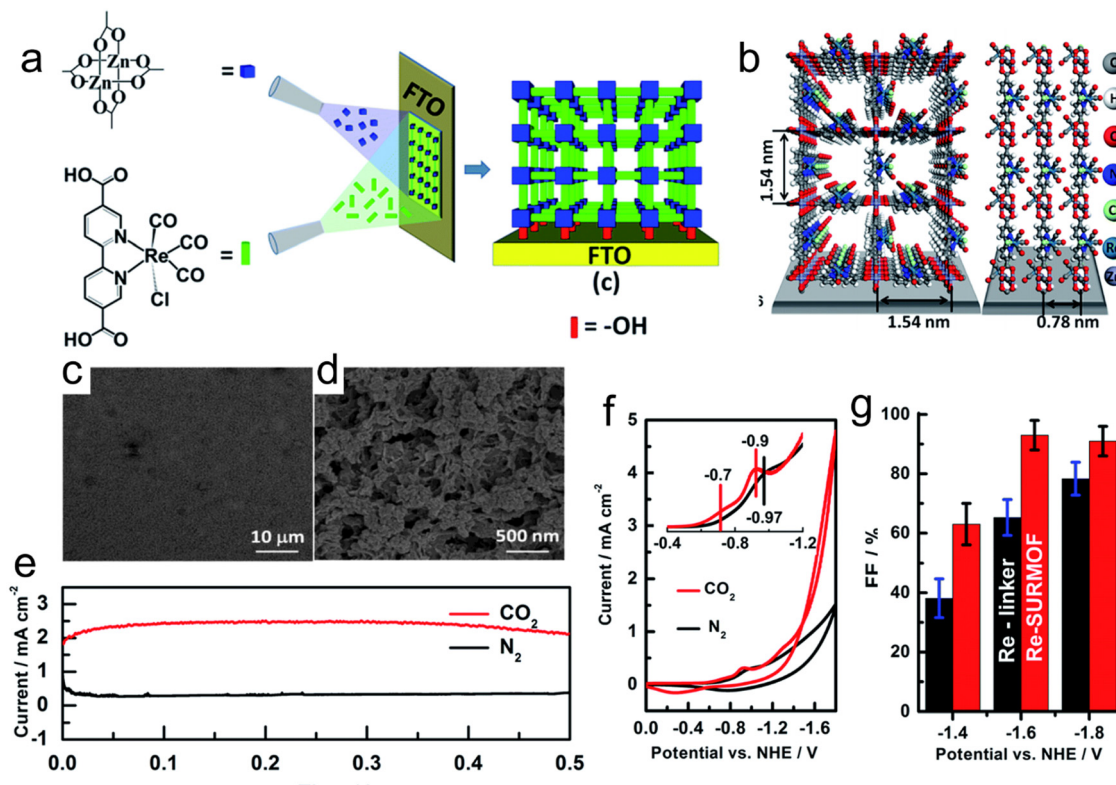
Fig. 13 (a) Schematic synthesis of Re-SURMOF. (b) Crystal structure of Re-SURMOF. (c and d) SEM images of Re-SURMOF. (e) Current density during catalysis of CO_2RR in CO_2- and N_2-saturated electrolyte. (f) Cyclic voltammograms of Re-SURMOF. (g) FE of Re-SURMOF. Reproduced with permission from ref. 165 Copyright 2016, RSC.

than that of BTB-MOL-CoPP. It was observed that TPY promoted the CO_2RR at all the measured potentials. The control experiment of BTB-MOL and TPY-MOL with CoPP-free functionalization showed that the only reaction was the HER, and all the results indicate that CoPP is the catalytic center and TPY ligand plays a role in promoting the CO_2RR. In the CV test, the performances of TPY-MOL-CoPP in a saturated CO_2- and N_2-atmosphere were tested, respectively. It was found that when the scanning rate was 200 mV s^{-1} in an N_2 atmosphere, the CV of TPY-MOL-CoPP with NaH_2PO_4/Na_2HPO_4 buffer solution displayed a reduction peak at 0.28 V vs. RHE, suggesting that $[CoPP]^0$ becomes $[CoPP]^-$. This means that the negative starting potential of the CO_2RR and HER should be greater than −0.28 V. The above-mentioned tests show that CoPP is the catalytic center of TPY-MOL-CoPP and the TPY ligand plays a role in promoting the CO_2RR. Based on the porphyrin MOF-525 (Fe-MOF-525) film as the active catalyst, Hod et al.[123] anchored a large number of active molecular catalysts on the conductive electrode for the CO_2RR. MOF-525 was chosen to immobilize the catalyst because it has good molecular porosity and chemical stability. In addition, the use of MOFs to fix molecular catalysts can effectively avoid polymerization and deactivation of the catalyst because each catalyst molecule is covalently connected with the frame node. This method generated (1015 active sites cm^{-2}) a high electrochemical surface area to synthesize CO gas (FE$_{CO}$ = 50%). Here, although the efficiency

of the CO_2RR was low, the results showed that molecular catalysts with MOF structures can be used for improved CO_2RR. Therefore, it is expected that the accumulation of molecular catalysts in MOFs will be further conducive to the design of advanced CO_2RR catalysts.

6.5 Metal nanoparticle@MOF

Noticeably, many metal nanoparticles (NPs) have been explored and used as electrocatalysts for the CO_2RR. However, in the catalytic process, the accumulation of these small NPs in macromolecules is always challenging. Thus, to address this problem and improve the practicality of extra catalytic active centers, several methods have been applied, including size reduction and shape control of NPs.[170,171] Compared to macro-molecule/large-size catalysts, MOFs having a porous structure with large specific surface area provide an improved platform for efficient CO_2 reduction and production functional materials. They can not only be used as a support material for metal molecular coatings, but also as an ideal material to instigate the uniform distribution of nanoparticles to reduce CO_2.

For example, Hupp et al.[172] prepared a catalyst for the CO_2RR by decorating Cu on the surface of NU-1000-MOF (Fig. 15a and b). The prepared catalyst exhibited catalytic ability for products of two phases, i.e., liquid-phase formate (HCOO) and gaseous-phase products (H_2 and CO). With reference to
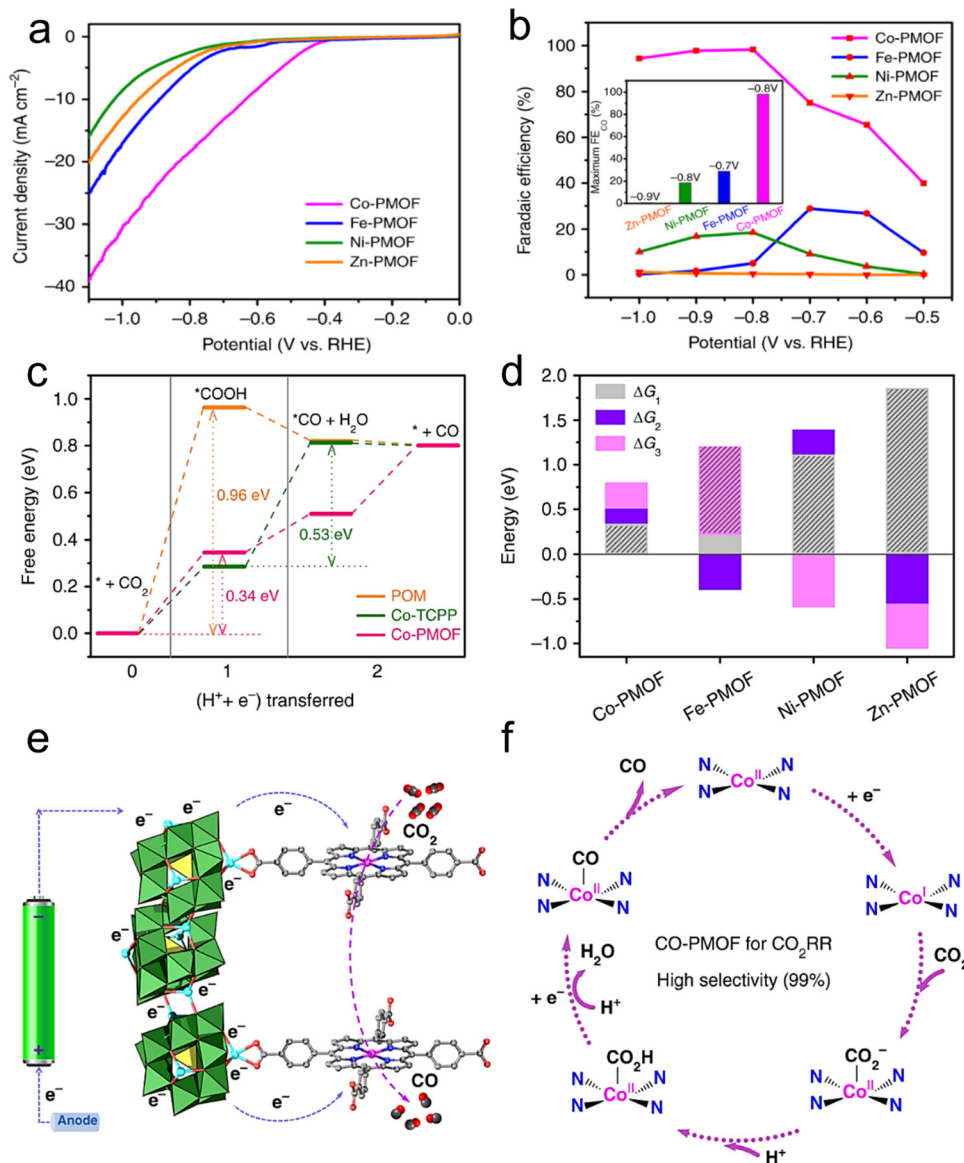
Fig. 14 (a) LSV curves of PMOFs. (b) FEs. (c) Free energy diagram. (d) Free energy comparison of elementary reactions. (e and f) Suggested mechanism for the CO_2RR on Co-PMOF. Reproduced with permission from ref. 168 Copyright 2018, Springer Nature.

RHE, formate production with an FE of 31% as the main product was achieved at −0.82 V. Overall, this Cu-NU-1000 MOF displayed a distinct CO_2RR performance compared to its individual components (Fig. 15c). Jiang and co-workers designed a composite of Ag_2O and ZIF *via* a refluxing method (Fig. 15d).[173] The prepared composite catalyst, Ag_2O/ZIF-7, presented improved CO_2RR results with an FE of 80% for CO compared to its individual components of ZIF-7 and Ag/C. The improvement in performance was attributed to be the synergistic combination of Ag_2O and ZIF, while the mass transfer was promoted due to the large specific surface area of the MOF. The electrocatalysis results showed that the Ag_2O nanoparticles were homogeneously dispersed on the ZIF surface. In addition, it was observed that when the Ag_2O/ZIF-7 composite reduced CO_2, it had a more positive onset potential of −0.6 V than the

ZIF-8/Ag_2O composite in 0.25 M K_2SO_4. The Ag_2O/ZIF-8 composite displayed a higher FE_{CO} of 80.6% at −1.2 V *vs.* RHE than that of its individual components of Ag/C and ZIF-8. This exceptional catalytic activity can be ascribed to the synergistic effect between the larger surface area of the MOF and significantly small size of the metal NPs (Fig. 15e–g). According to the above discussion, it is clear that MOF composites are also active catalysts.

7. Confinement effect of MOF-derived carbon materials for CO_2RR

7.1 MOF-derived atomic-dispersed carbon materials

Atomic-level catalysts refer to metal/non-metallic active centers that are dispersed at the atomic level on a carrier, avoiding their
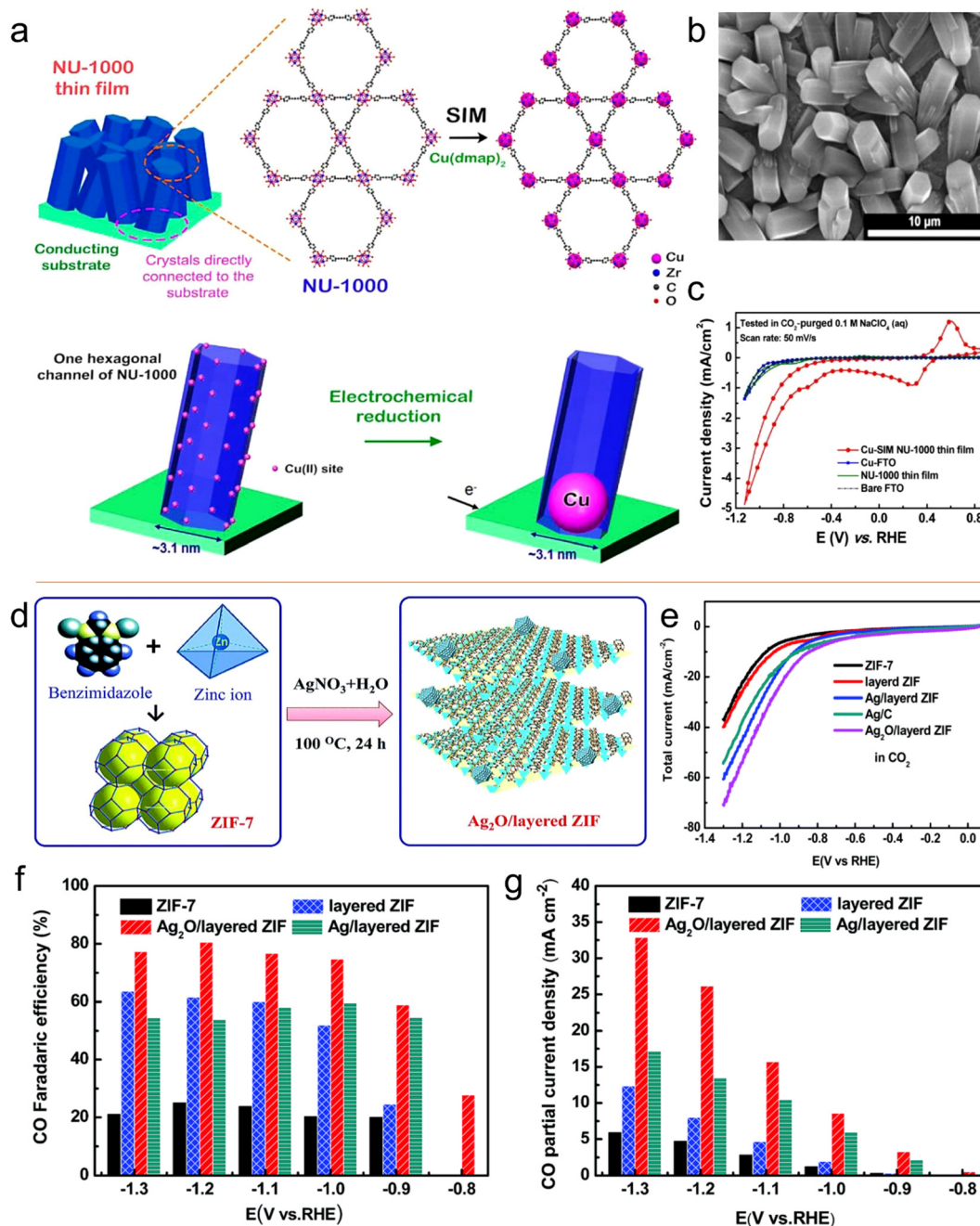
Fig. 15 (a) Schematic representation of installation of SIM in Cu(II) single site. (b) SEM image of NU-1000 film. (c) CV curves. Reproduced with permission from ref. 172 Copyright 2017, ACS. (d) Schematic synthesis of Ag_2O/layered ZIF. (e) LSV curves and (f) FEs for CO. (g) CO partial current densities $vs.$ V. Reproduced with permission of ref. 173 Copyright 2017, RSC.

accumulation. Nanocrystals exhibit excellent activity and selectivity for the CO_2RR when their size decreases to the atomic level and they are dispersed atomically because of the significant reduction in their energy with a decrease in their size.[174,175] However, during the sintering process, metal atoms easily migrate and accumulate to form clusters, resulting in a decrease in the density of active centers, and thus decreased catalytic activity.[176] Therefore, various strategies, such as spatial confinement,[177] coordination design[178] and

defect engineering,[179] have been adopted to prevent the agglomeration of metal atoms.

An effective way to construct single-atomic catalysts is with the assistance of MOFs to prevent atomic agglomeration. MNC materials are extensively studied catalysts for the CO_2RR. Zhao et al.[180] reported the decoration of ZIF-8 with Ni atoms, and after high-temperature treatment at 1000 °C, the Zn atom was replaced with Ni, finally forming Ni active centers. This single-atomic catalyst could efficiently reduce CO_2 to CO with 70% FE.
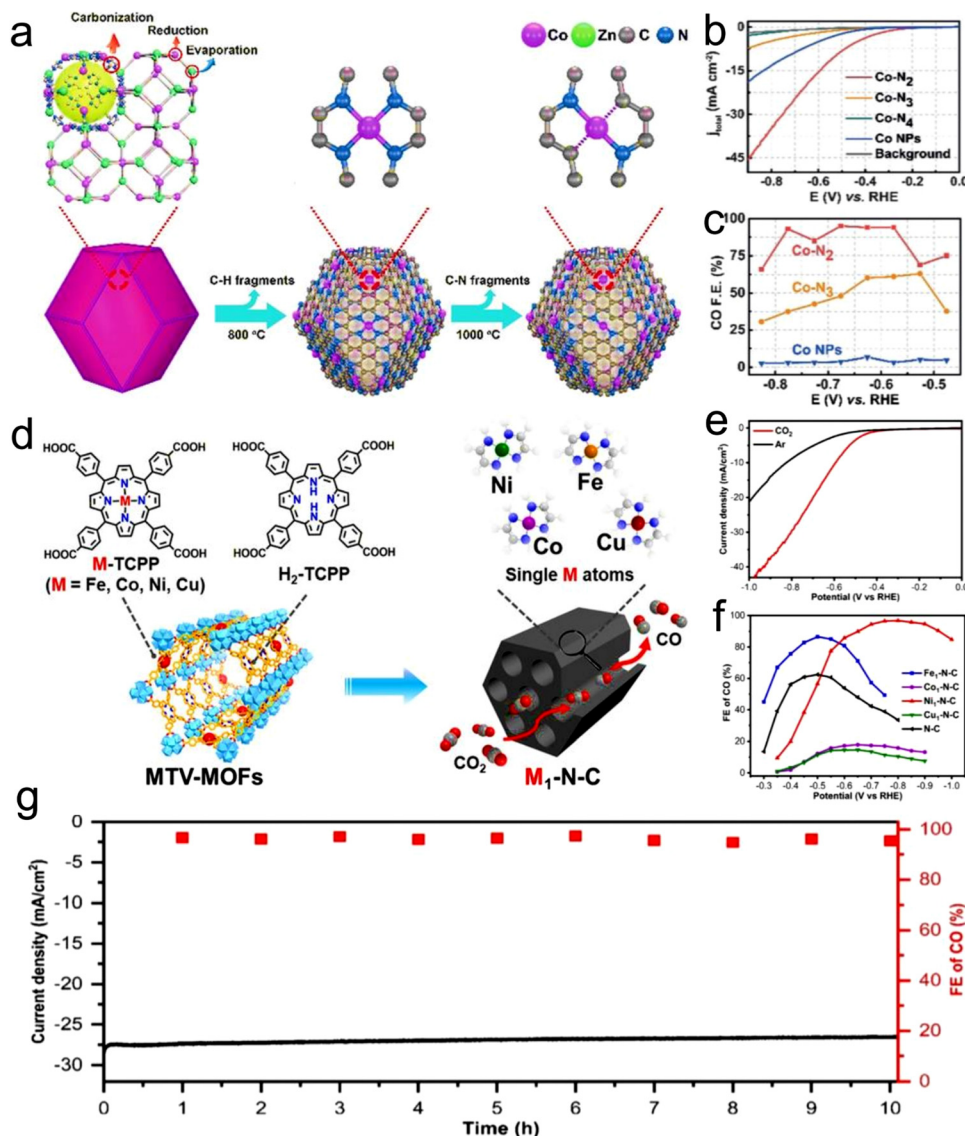
Fig. 16 (a) Co–N$_4$ synthesis process. (b) LSV curves of all the materials and (c) FEs. Reproduced with permission from ref. 181 Copyright 2021, Wiley. (d) Synthesis of M$_1$–N–C single-atom catalysts. (e) LSV curves of Ni$_1$–N–C. (f) FEs and (g) durability test of Ni$_1$–N–C. Reproduced with permission from ref. 182 Copyright 2020, Wiley-VCH.

The FE$_{CO}$ of the Co monatomic catalyst prepared using a similar method was up to 94%, and at the overpotential of 520 mV, the current density was 18 mA cm^{-2} with a TOF of 18 200 h^{-1} for CO. Under the applied voltage of −0.63 V, the current density attenuation of Co–N$_2$ during 60 h operation was negligible, and the FE$_{CO}$ remained almost unchanged (Fig. 16a–c).[181] The theoretical and experimental results displayed that the decrease in the coordination number of Co–N (4 to 2) supports the initiation of CO$_2$ to the CO$_2^{\bullet-}$ intermediate, thus improving the CO$_2$RR performance. Jiao et al.[182] designed several single-atomic electrocatalysts (e.g., M$_1$–N–C, M =,Co Fe, Cu and Ni) using a porphyrin polymetallic framework structure under the confinement effect. These single-atom metal catalysts possessed physical characteristics (specific surface area, particle size, and pore structure).

Importantly, when the CO$_2$RR performance of Ni$_1$–N–C was compared with that of the other M$_1$–N–C, the former exhibited a lower COOH production energy and lower desorption energy for CO. Hence, Ni–N–C with single-atom Ni displayed the best performance for the CO$_2$RR as the active center with high selectivity for CO (FE up to 97%, Fig. 16d–g). Furthermore, Ni$_1$–N–C had high selectivity and feasibility in industrial production at the CO$_2$ concentration of 30% and 15% (volume fraction), which further showed its superior and excellent selectivity for the CO$_2$RR. Besides, Hao et al.[183] systematically studied the selectivity and activity of transition metal and nitrogen doped-carbon for the CO$_2$RR to elaborate its significance. Using different metal nitrogen-doped carbon materials (e.g., M–N–C, M = Ni, Mn, Cu, Fe, Co) as model catalysts, they systematically studied the selectivity and activity of these
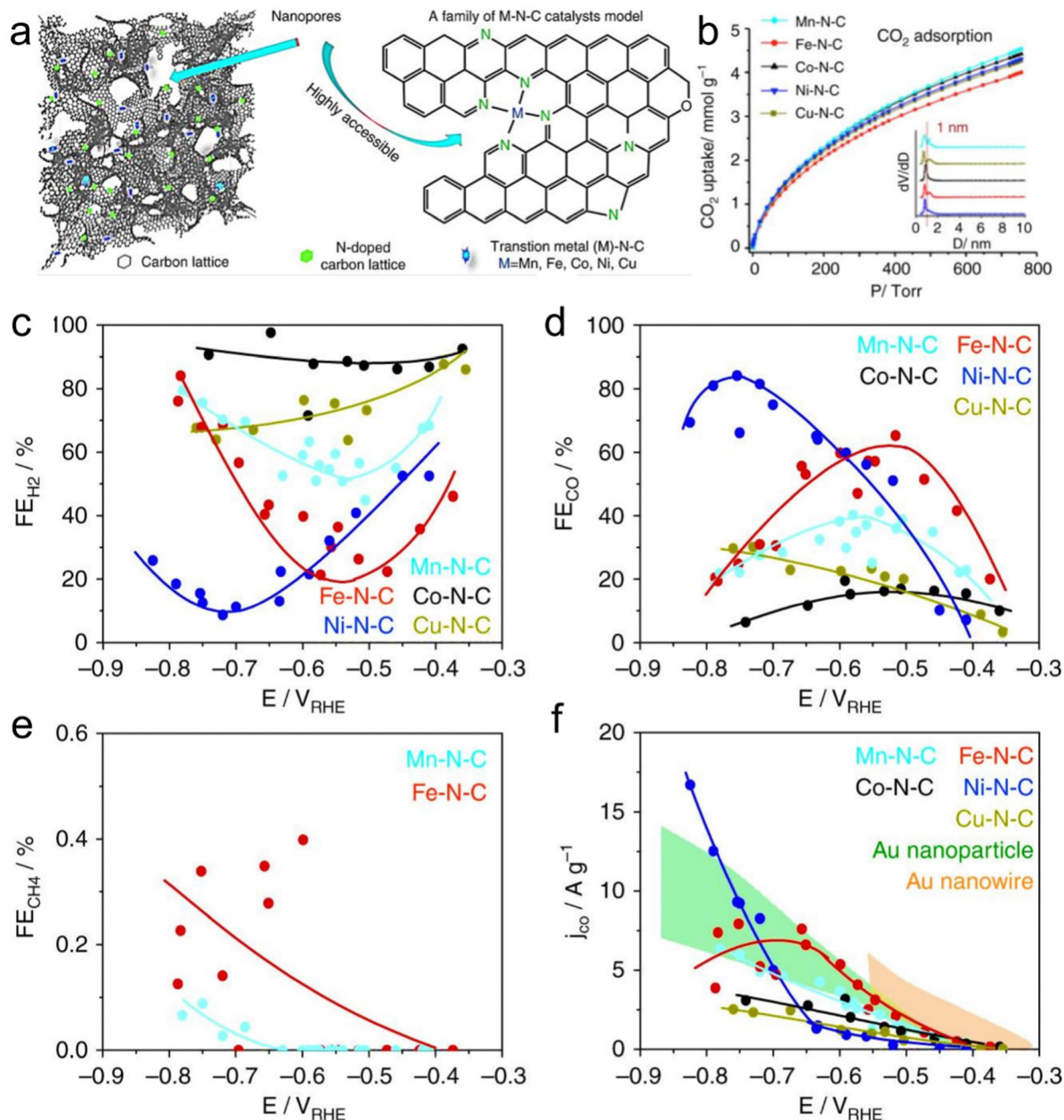
Fig. 17 (a) M–N–C model and structure. (b) Adsorption isotherm curves for CO_2 and inset is the pore size distribution. (c–e) FEs of H_2, CO and CH_4, respectively. (f) Mass-normalized partial currents for CO. reproduced with permission from ref. 183 Copyright 2017, Springer Nature.

catalyst in the CO_2RR to CO process through experiments and calculations, and found that the highly dispersed metal–nitrogen coordination center is the active site, which has guiding significance for the development of this type of materials (Fig. 17a). This series of M–N–C materials has a multi-stage pore structure, and the pore size of the micropores is uniformly distributed at 8 Å, showing strong CO_2 affinity. Under normal pressure, the CO_2 adsorption capacity reached 4–5 mmol g^{-1} (Fig. 17b). Furthermore, the catalyst precursor is a metal N coordination polymer crystal. After thermal decomposition, the metal–nitrogen coordination center was uniformly dispersed at the molecular level. The surface chemistry of this series of M–

N–C materials was analyzed, confirming the existence of the metal–N coordination structure, and the content and distribution of other forms of nitrogen-containing functional groups.

Here, the different samples did not show significant differences. Firstly, the activity of these catalysts was analyzed by linear sweep voltammetry (LSV). Comparing the LSV curves in the presence and absence of CO_2, it was found that Mn–, Fe–, Ni– and Cu–N–C exhibited CO_2 reducing activity and showed a lower overpotential compared with that for the HER. However, the HER activity of the Co-N-C sample dominated the Faraday process. The FE of the product was analyzed, and it was found that CO and H_2 accounted for the transferred charge of more

than 95%. It is worth noting that Mn–N–C and Fe–N–C catalyzed the reaction to produce a detectable amount of methane (CH_4). Although the density of metal–nitrogen active centers was low, its mass-normalized CO_2 conversion yield is equivalent to the best Au catalyst at present, especially in the high current range with practical application significance (Fig. 17c–f). This shows that metal- and nitrogen-doped carbon catalytic materials have great application significance for the CO_2RR.

Recently, Liao et al.[184] designed a reasonable active site structure and regulated and integrated its local chemical environment to realize the highly selective C_{2+} product under neutral conditions. The Cu-HITP MOF was used for the CO_2RR, and the FE of the C_{2+} product was 45.59%, and then the FE of the C_{2+} products significantly increased to 75.09% when polydopamine (PDA) was coated on the surface of Cu-HITP to provide a chemical microenvironment conducive to the CO_2RR to multi-carbon products (Fig. 18a, b and d). In addition, Cu-HITP@PDA has good electrocatalytic stability, where its current density and product selectivity remained basically unchanged in the stability test of 10 h. The CO_2RR mechanism was inspected using the in situ FTIR technique.

By comparison, it was found that the key intermediates *COH and *OCCOH in the process of CO_2RR red-shifted during in situ FTIR testing after the catalyst was coated with PDA due to the presence of hydrogen bond interactions. It was suggested that amino groups can be used as hydrogen bond donors to stabilize some basic intermediates for the formation of multi-carbon products, thus promoting the formation of C–C bonds. Zhang et al.[185] also reported a significant development in the design and synthesis of monatomic catalysts for the CO_2RR. They designed a nitrogen-doped carbon carrier anchored on an MOF-derived carbon carrier with $In^{\delta+}-N_4$. The monoatomic catalyst possessed an N_4 atomic interface structure (Fig. 18c and f). The catalyst exhibited an excellent CO_2RR performance. At −0.65 V, In SA_S/NC exhibited the maximum FE of 96% and optimal conversion frequency (TOF) of 12500 h^{-1}, which is
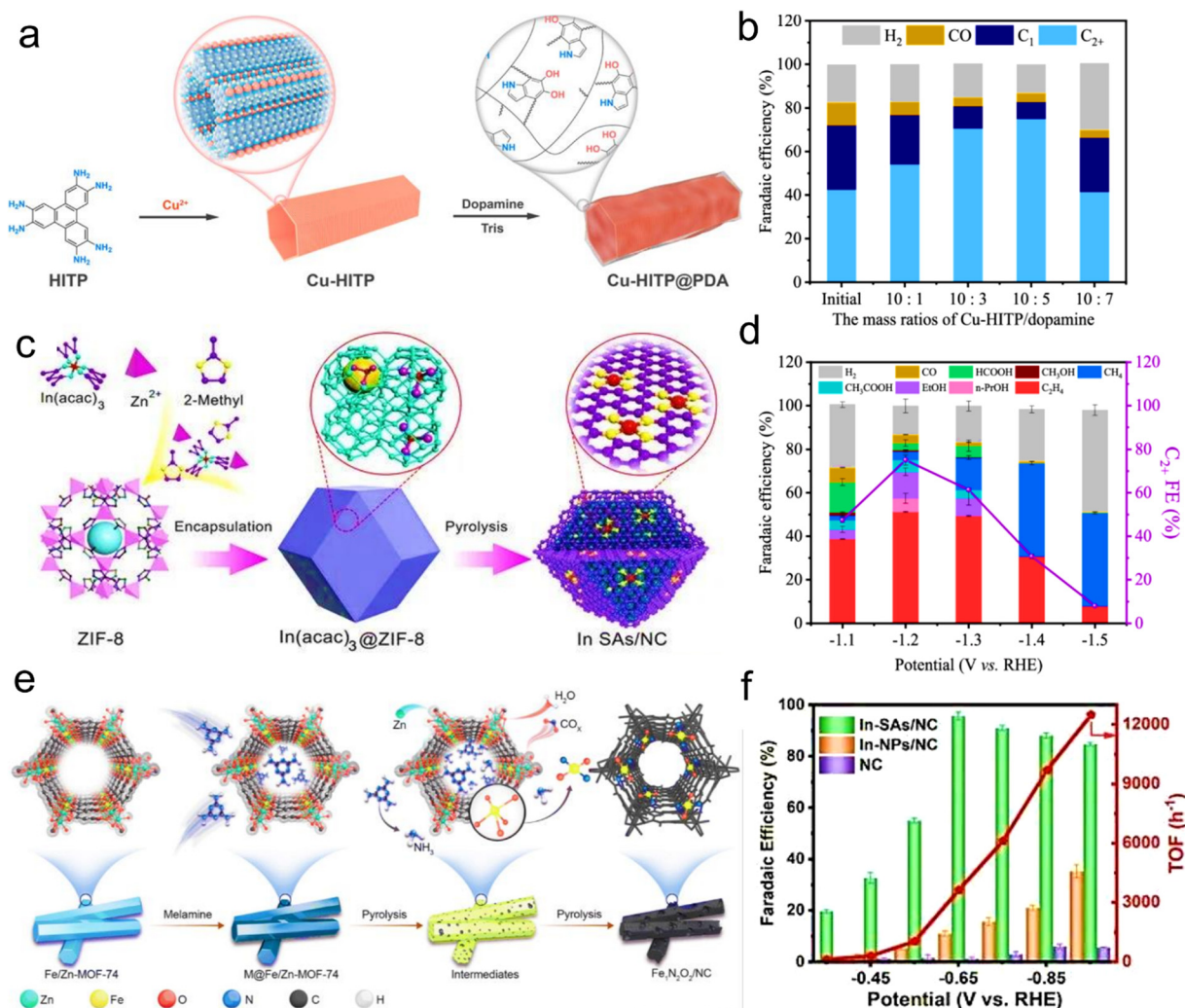
Fig. 18 (a) Synthesis of Cu-HITP and Cu-HITP@PDA. (b) Comparison of CO_2RR performances of Cu-HITP with different PDA coating amounts. Reproduced with permission from ref. 184 Copyright 2022, ACS. (c) Synthesis of In/NC single atom. (d) FEs of different products. Reproduced with permission from ref. 184 Copyright 2022, ACS. (e) Preparation of $Fe_1N_2O_2$/NC catalyst. Reproduced with permission from ref. 186 Copyright 2022, RSC. (f) TOF and FEs of formate. Reproduced with permission from ref. 185 Copyright 2020, Wiley.

superior to most similar catalysts. In addition, the XAFS study based on synchrotron radiation showed that the In$^{\delta+}$–N$_4$ atomic interface structure has high catalytic activity for the CO$_2$RR. The DFT simulation results showed that the In$^{\delta+}$–N$_4$ atomic interface has low free energy for the formate intermediate (HCOO*), which is conducive to advancing the catalyst activity for the CO$_2$RR. This study provides a novel approach for the rational design of main group catalysts for energy applications.

Recently, Chen et al.[186] reported that the Fe–N$_x$ coordination structure is the common structure of Fe–N–C in various M–N–C catalysts, which is expected to replace the traditional noble metal-based CO$_2$RR catalysts in the near future. For Fe–N–C-type electrocatalysts, the energy barrier is higher to produce *COOH. Also, given that the binding of *CO on the active site is relatively strong, CO desorption is difficult.

Therefore, the key to improving the CO$_2$-to-CO conversion efficiency of Fe–N–C electrocatalysts is to support the formation of *COOH (protonation) and optimize the binding strength of *CO (desorption). Zn-MOF-74 was selected as the precursor of oxygen enrichment for synthesis regulation, and then Fe/Zn-MOF-74 was obtained by doping Fe ions. After introducing an N source, it was calcined, finally producing the Fe$_1$N$_2$O$_2$/NC catalyst with a special coordination structure (Fig. 18e). The FE$_{CO}$ of the catalyst was maintained above 95% in the large potential window of −0.4 to −0.8 V. It is worth noting that the FE$_{CO}$ even reached 99.7% at −0.5 V, which is almost 100%. In addition, the formation mechanism of Fe$_1$N$_2$O$_2$/NC was revealed by analyzing the synchrotron radiation results of the calcined products at different temperatures. The theoretical calculation showed that compared with the traditional Fe–N$_4$ catalyst, the introduction of O and N together to regulate the interface of Fe atoms has a significant advantage in electrocatalytic carbon dioxide reduction to produce CO. The unique coordination structure of Fe$_1$N$_2$O$_2$ showed a small free energy change in the generation of the COOH* intermediate and CO desorption, thus accelerating the reaction rate and improving the catalytic performance. Moreover, recently, carbon-based catalysts having bimetallic sites derived from MOFs have attracted extensive attention due to their bimetal atoms centers and synergistic effect, which enhance the density of active centers and improve the performance. For example, Ren et al.[187] designed Fe/Ni bimetal carbon catalysts (Ni/Fe N–C) via the calcination the precursor of ZIF-8. It exhibited a high density of sites and activity and good catalytic performance for the CO$_2$RR. It is worth noting that due to the weak binding energy of *COOH and *CO on the surface of Ni/Fe–N–C, Fe/Ni displayed a decreased energy barrier, while increased CO$_2$RR performance. The reduction selectivity of CO$_2$ to CO was quite good given that the FE reached 98%. In the CO$_2$RR catalytic process, atomically dispersed active centers display excellent activity and selectivity toward CO production. Nevertheless, there are still many limitations in understanding the internal factors and structural influences that affect the performance of monatomic catalysis. Wu et al.[188] used the Fe–N–C as a standard catalyst to divide three key parameters, i.e., particle size, Fe percentage and structure of the Fe–N bond, and they

completely illustrates the factors affecting the CO$_2$RR performance. Importantly, the particle size and doped iron percentage are crucial to regulate the exterior morphology, porosity, surface area, electrochemical activity and graphitization degree of carbon in FeN$_4$.

Firstly, the Fe cluster catalyzes the formation of the surrounding graphite carbon shell. Secondly, it may promote the charge transfer to the central site of FeN$_4$. It also acts as a catalytic promoter. Reasonable control of the surface coordination number of copper clusters can offer active centers and optimize the activity, selectivity and efficiency for the CO$_2$RR. Sargent et al.[190] used a special structure to regulate the surface structure of copper clusters in the deformed HKUST-1 MOF. The results illustrated that the Cu clusters formed at the position of the deformed Cu dimer increased the ethylene FE from 10% to 45%. Additionally, the yield of H$_2$ decreased to less than 7%, which proved that MOFs can be used to alter the surface of copper clusters in the CO$_2$RR catalytic process.

MOF-derived monoatomic-dispersed carbon materials (M–N–C) are designed with the help of the limiting strategy, which can limit the metal atom dispersion, enhance the active center density, reduce the desorption–absorption energy barrier of the intermediates for the CO$_2$RR, speed up the reaction process, and advance the product selectivity.

7.2 MOF-derived carbon-based nanoparticles

Other metal materials derived from MOFs for the CO$_2$RR are metal alloys, metal nanoparticles and metal oxides. Among them, metal oxides and alloys are extensively studied for the CO$_2$RR. Alloys mostly show better or totally diverse catalytic output than monatomic materials, which improve the CO$_2$ conversion effectiveness and purposely reduce CO$_2$ to specific target products. To realize the goal of adjusting the ratio of products, metal oxides usually form alloy oxides with multiple metals to increase the CO$_2$RR performance. For example, Guo et al.[191] designed a series of carbon-based catalysts derived from an MOF, which contained different proportions of Cu/In bimetallic oxides. The as-prepared In/Cu bimetallic oxide catalysts exhibited a good CO$_2$RR electrocatalysis performance. It is notable that by regulating the proportion of Cu/In, different CO/H$_2$ compositions could be obtained. When the current density was 11.2 mA cm^{-2}, the maximum FE$_{CO}$ reached 92.1%, and the catalyst was stable for more than 24 h. The high activity for the CO$_2$RR is attributed to the fact that the addition of Cu to In$_2$O$_3$ can improve the interaction between electrons, and consequently increase the density of active centers, improve the adsorption capacity of CO$_2$ and accelerate the rate of electron transfer.

Zhong and co-workers prepared a layered bimetal conjugated MOF (PcCu–O$_8$–Zn) via a solvothermal method using a phthalocyanine linker and ZnO$_4$ (Fig. 19a and b). The selectivity for the CO$_2$RR to CO was promoted by PcCu–O$_8$–Zn and the FE was high as 88%; furthermore, the TOF was 0.4 s^{-1}. Additionally, PcCu–O$_8$–Zn showed good stability (>10 h) at −0.7 V (Fig. 19c and e). The results showed that the coordination of ZnO$_4$ in PcCu–O$_8$–Zn catalyst has high activity toward CO$_2$ to
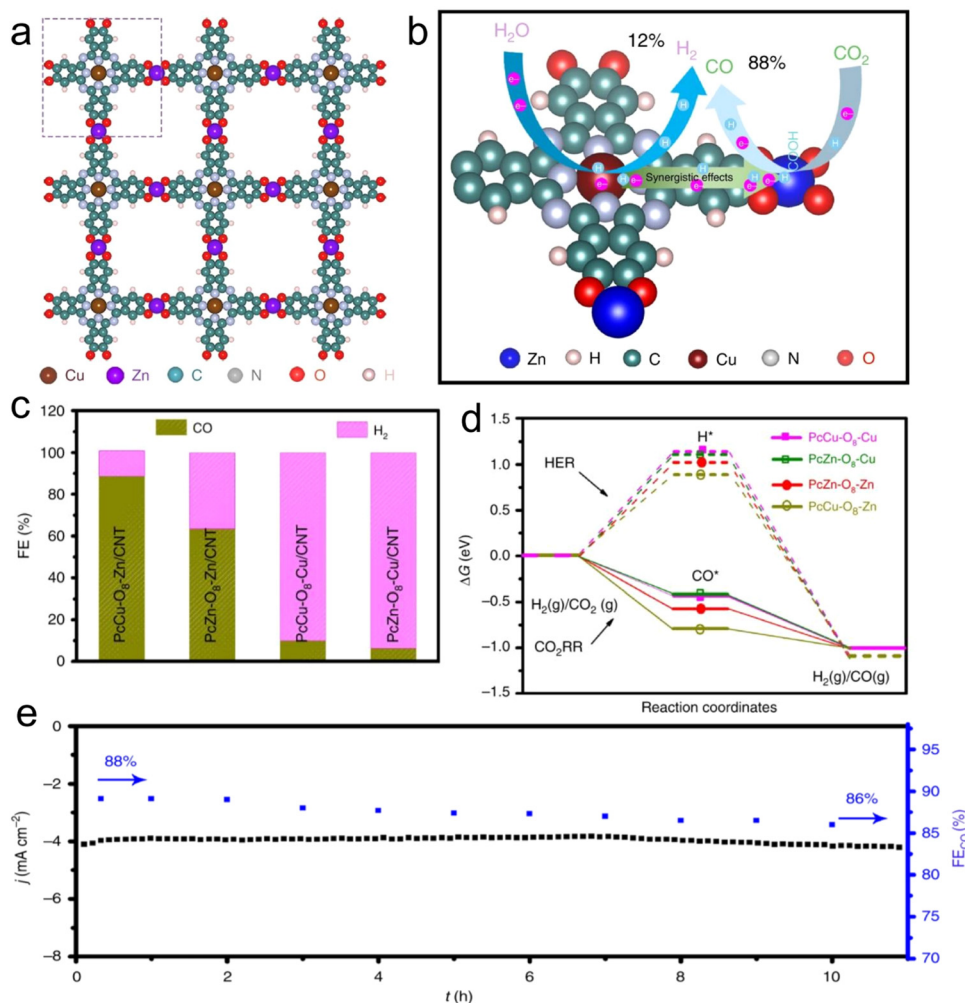
Fig. 19 (a) Illustration of the crystal structure of Zn−PcCu−O$_8$. (b) Depiction of CO$_2$RR and HER over Zn−PcCu−O$_8$. (c) FEs of H$_2$ and CO for different catalysts. (d) Possible free energy diagram for different catalysts. (e) Amperometry ($i \sim t$) stability test for Zn−PcCu−O$_8$/CNT. Reproduced with permission from ref. 189 Copyright 2020, Springer Nature.

CO conversion, while the coordination of CuN$_4$ in PcCu−O$_8$−Zn MOF promotes the protonation of *CO$_2$ adsorbed on the ZnO$_4$ complex (Fig. 19d). Thus, the bimetal active centers in the catalytic materials show a worthy synergistic effect on the CO$_2$RR, thus accelerating the whole CO$_2$RR kinetics.[189] Reddy et al.[192] obtained a Co/Ce$_{0.8}$Zr$_{0.2}$O$_2$ catalyst using an MOF as a template, which showed excellent activity and stability for the CO$_2$RR to methane. Alternatively, metal nanoparticles are also widely used as catalysts due to their high conductivity, high stability, and large surface area. Zhang et al.[193] used H$_2$O$_2$ as the only reductant and seed-mediated growth method to synthesize sea−urchin−needle-shaped gold nanoparticles as a catalyst for the CO$_2$RR, effectively improving current density and CO selectivity. There is an obvious tip electric field effect at Au needles, which enriches cations and increases the CO$_2$ concentration at the tip during the catalytic process. Kim et al.[194] used MOF-74 derivatives to prepare highly dispersed Cu nanoparticles to increase the yield of CO$_2$RR to CH$_4$. The experimental results showed that the Cu NPs derived from the

MOF had low aggregation and excellent electrocatalytic properties due to the existence of a stable eutectic structure, high selectivity and activity for mono-carbon products.

The high selectivity of Cu NP catalysts for the CH$_4$ was attributed to the inhibition of C−C bond coupling by the isolated NPs. Recently, Wang et al.[195] reported the design of Cu nano-ribbons via the in situ electrochemical reduction of a Cu-based organometallic skeleton for high selectivity for the production of C$_{2+}$ compounds (Fig. 20a). The experimental results showed that the FE for C$_{2+}$ was 82% and the partial current density was 348 mA cm^{-2} in the flow electrolytic cell when the mesoporous structure was used for CO$_2$ electroreduction (Fig. 20b). Compared with Cu nanoleaves and nanorods without a porous structure, the Cu nanobelts significantly improved the selectivity for C$_{2+}$ products in CO$_2$ electroreduction. The finite domain (FDTD) outcomes showed that electric field on the surface of catalyst can be increased using a mesoporous structure, thereby increasing the concentration of K ions and OH$^-$ and promoting the reduction of CO$_2$ to C$_{2+}$ products.
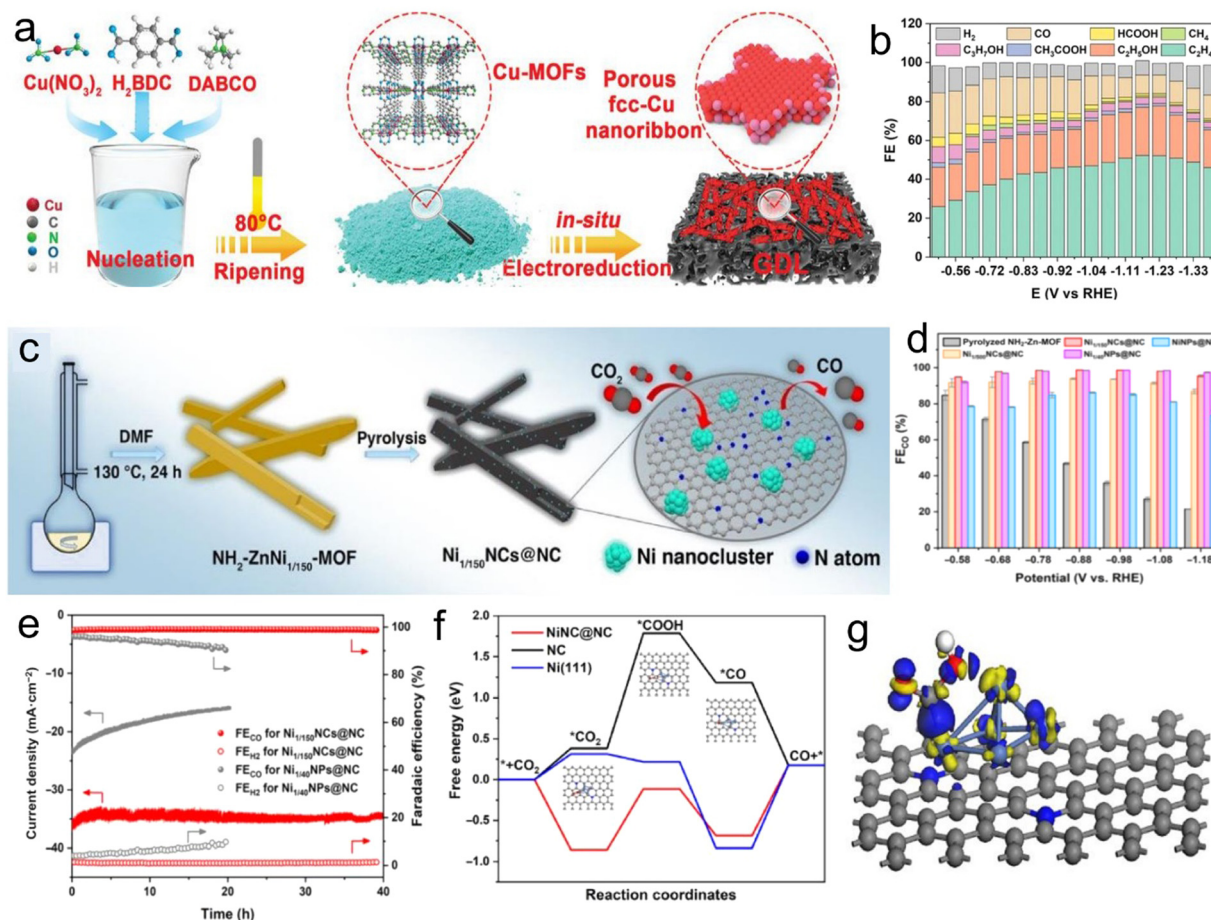
Fig. 20 (a) Synthesis scheme of Cu–MOFs and porous Cu nanoribbons. (b) FEs for Cu nanoribbons. Reproduced with permission from ref. 195 Copyright 2021, Wiley. (c) Synthesis of $Ni_{1/150}NCs@NC$ catalyst. (d) FEs. (e) Stability tests. DFT calculation for CO_2 electrocatalytic reduction: (f) free-energy diagram for different models. (g) Depiction of electron density difference between Ni cluster and *COOH intermediate. Reproduced with permission from ref. 68 Copyright 2022, Springer.

Recently, Xu et al.[68] synthesized highly dispersed Ni nanoclusters with a size of less than 2 nm on NC using Zn/Ni bimetallic MOF precursors (Fig. 20c). The contents and size of the material were successfully controlled by changing the proportion of Zn : Ni in the MOF precursor. The amino functional group on the MOF linker has an important influence on the Ni catalyst size and the performance of the carbon-based catalysts. At the best possible ratio of 150 : 1, Ni nanoclusters with a particle size of 2 nm were obtained by pyrolysis of the MOF. The synthesized catalyst exhibited a high FE_{CO} of 98% and partial current density (J_{CO}, −40 mA cm^{-2}) at −0.88 V (Fig. 20d). The design principle and discovery of the catalyst may have a certain guiding significance for the preparation of highly efficient electrocatalysts for various reactions using other metals. Using bimetallic Ni/Zn MOF precursors with different Ni : Zn ratios, Ni particles with a diameter of 1.8–200 nm were prepared on a nitrogen-doped carbon matrix without any post-processing steps. In the case of an ultra-low Zn : Ni ratio of 150 : 1 and the existence of amino functional groups in the MOF linker, vastly dispersed 1.9 nm Ni nanoclusters were obtained on NC. The results showed that catalytic

performance was significantly enhanced by decreasing the size of Ni on NC. Ni_1 was synthesized at the optimum Ni : Zn ratio of 1 : 150/150NCs@NC. At −0.88 V potential, it exhibited an efficient, selective and stable ECR for CO production with FE of 98.6% and J_{CO} of −40 mA cm^{-2}. In the 40 h stability test (Fig. 20e), the J_{CO} was maintained at 96% and the FE_{CO} was stable. Furthermore, the models calculated by DFT showed that compared with the original NC and big-sized Ni particles, the Ni nanoclusters anchored on the NC substrate are more likely to form *COOH intermediates (Fig. 20f and g), and the electron transfer rate on the reaction interface is faster.

7.3 MOF-derived non-metallic carbon materials

Metal-free carbon materials derived from MOFs mainly include intrinsically defective materials and metal-free heteroatom-doped carbon materials. The heteroatom doping can improve the electronic property of materials; accordingly it causes confined charge polarization, spin state redistribution and local charge density, finally enhancing the desorption/adsorption process on the active sites for the reaction intermediates.[198–200] In addition, the conductivity of carbon

materials is increased by doping heteroatoms, which is also beneficial to activate the carbon atoms, and thus improve the catalytic performance of carbon materials.[201] Nevertheless, Jia et al.[202] recently found that the inherent defects of a five-membered ring showed greater activity than that of carbon doped with nitrogen atoms. With the deepening of research, it has been found that reasonably designed inherent defects (such as edges, holes, vacancies and topological defects) in the skeleton of carbon can regulate the electronic of materials, offering more active centers for catalysis. Especially, the presence of topological defects can efficiently increase the activity of catalysts for the CO_2RR.[203] The key technique to create topological defects in the carbon skeleton is denitrification. The original nitrogen atoms are removed from the graphene-like structure (six-membered ring) through the pyrolysis carbonization process to obtain five-membered rings and seven-membered rings. The carbon atoms with dangling bonds connect with each other to form topological defects.[204] Kang et al.[205] synthesized the Zn NP@ZIF-8 hierarchical porous carbon-rich catalyst with defects (DHPC) through pyrolysis. The mesoporous structure and carbon defects improved the CO_2 adsorption and activation efficiency of DHPC. In 0.5 M

$KHCO_3$ medium, the FE_{CO} reached 99.5% at −0.5 V. The simulation results displayed that the CO_2 adsorption energy barrier of the topologically defected five-membered ring was negative, demonstrating that the adsorption of CO_2 is a spontaneous process. The N-free DHPC catalyst had a lower energy barrier to reduce CO_2 to CO than the N-pyridine-doped carbon catalyst. In addition, the *CO desorption process on the surface of DHPC produced heat. Consequently, the MOF-derived inherent carbon defects had an appropriate adsorption/desorption energy for CO_2 and the reaction intermediate. In turn, the CO_2 molecules were excited and the electrocatalytic CO_2 reduction performance was improved. Chen et al.[196] removed pyrrole-N and pyridine-N from porous carbon materials, while they were doped with N heteroatoms through annealing at high temperature under an NH_3 atmosphere using an MOF, resulting in extra topological defected carbon (Fig. 21a). The results from NEXAFS characterization of carbon illustrated that with an increase in the annealing temperature, the ratio of pyrrolic and pyridinic-N in the carbon skeleton decreased, with the topological defect density progressively increasing, and the CO_2RR performance also improved accordingly. Specifically, DPC-950-NH_3 exhibited significant catalytic activity and
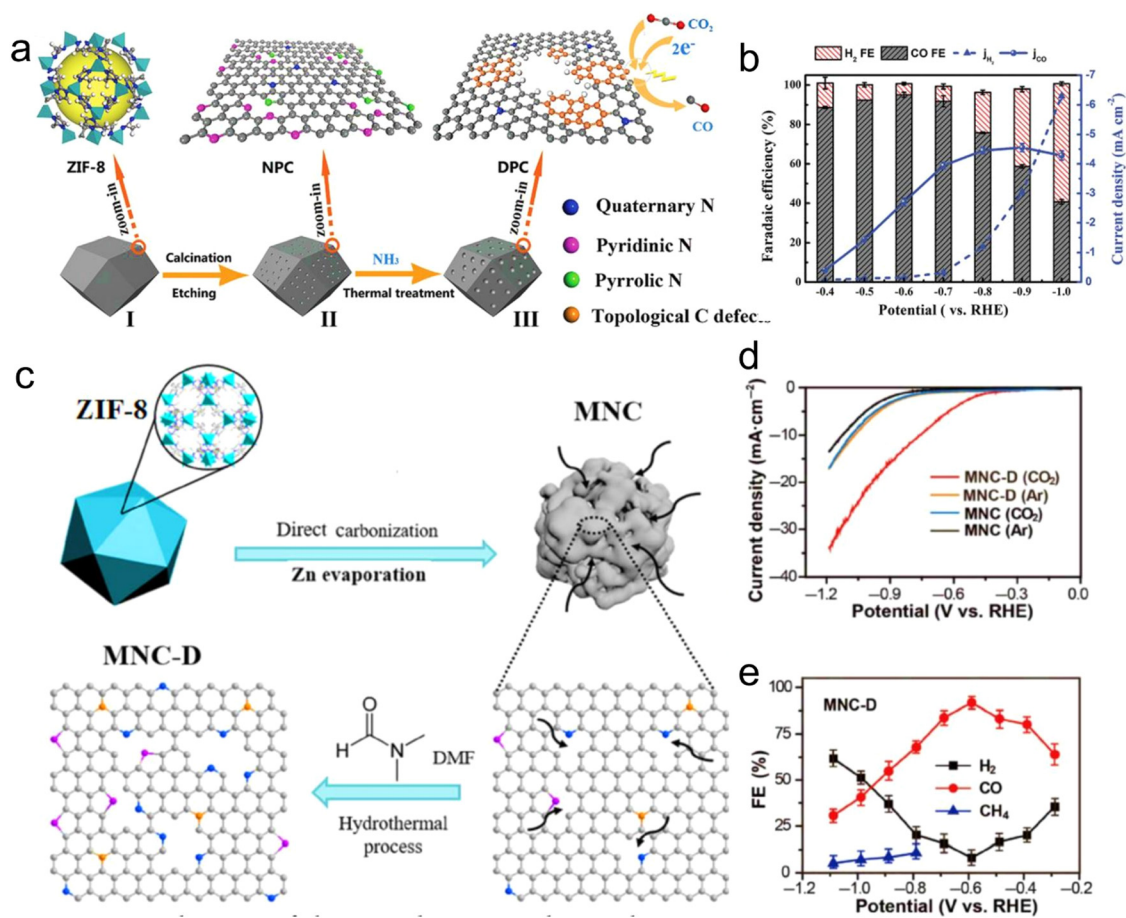

Fig. 21 (a) Synthesis route of defected porous carbon. (b) FEs of CO and H_2 and the partial current densities over DPC. Reproduced with permission from ref. 196 Copyright 2020, Wiley. (c) Synthetic procedure from MNC-D. (d) LSV curves of MNC-D and MNC. (e) FEs over MNC-D. Reproduced with permission from ref. 197 Copyright 2019, Springer.

selectivity for CO_2RR to CO. DFT calculations showed that the reaction intermediate has more suitable adsorption and desorption free energy on the carbon material containing defects than that without defects (Fig. 21b). In general, the activity of N-doped carbon materials depends on the content and type of N-doped elements. Zheng *et al.*[197] reported that N-doped mesoporous carbon materials were obtained by metal–organic skeleton transformation and controlled by the secondary treatment of *N*,*N*-dimethylformamide (DMF). The carbon materials obtained from metal–organic skeleton conversion had numerous electron-rich defects due to N-doping (Fig. 21c). However, due to the high-temperature treatment, these electron-rich defects have no CO_2RR activity. Based on this, when DMF is used for secondary treatment of carbon materials obtained from metal–organic skeleton conversion, the porous and defective characteristics of the carbon materials are conducive to the entry of small molecules of DMF, which can form more pyridine–nitrogen catalytic active sites and increase the CO_2RR efficiency of the catalyst. The electrochemical test outcomes displayed that the N-doped mesoporous carbon structure (MNC-D) after DMF secondary treatment had high catalytic activity for the CO_2RR in 0.1 M $KHCO_3$ electrolyte. Under the voltage of -0.58 V *vs.* RHE, the reduction current of carbon dioxide reached -6.8 mA cm^{-2}, and the selectivity for carbon monoxide reached $\sim$92%. Simultaneously, after 16 h reaction at -0.58 V *vs.* RHE, its current density and selectivity were 84% and 83% of the initial value, respectively, showing excellent cycle stability (Fig. 21d and e). Thus, this method provides a feasible idea for preparing carbon-based CO_2RR materials.

In addition, the catalytic performance of carbon materials without doped heteroatoms can be significantly enhanced by suitably regulating the inherent carbon defects. Inherent defects will certainly be introduced in the synthesis of carbon materials. Thus, it will be significant to deeply understand the influence of inherent defects of catalysts for CO_2RR outputs using different advanced techniques to interpret their mechanism, particularly *in situ* techniques and theoretical calculations to obtain further new effective and robust electrocatalysts. In most studies, compared with non-metal carbon materials derived from MOFs, pre-designed reaction centers and monatomic catalysts having porous structures of can enable desorption/adsorption for CO_2RR. Nevertheless, because of the high surface structure of single-atom metal catalysts, their catalytic activity significantly decreases in the electrolysis process. Moreover, increasing the interactions between the support and metal is of great importance to improve the durability of monoatomic catalysts in practical applications.

7.4 MOF-derived single-atom catalysts

Catalysts based on transition metals have been studied intensively in the field of CO_2RR. The electronic structure of valence electrons of transition metals changes when they are specifically adsorbed with CO_2 reduction intermediates due to the existence of d orbitals that are not occupied by electrons. The

CO_2RR is a multi-step PCET process, and the inherent activity of the catalyst can be evaluated by the electronic behavior of the active centers on the its surface. In this case, the change in the valence electron structure of transition metals is beneficial to improve the reduction efficiency and selectivity in the CO_2RR.

Given that iron (Fe) is the second most abundant metal on Earth, it is desirable to develop Fe-based SACs to realize the CO_2RR.[207] Because of their large abundance, it is convenient to study the mechanism of CO_2RR on these materials with the most common FeN_x structure. However, in the preparation of SACs, there is a common problem that single atoms and nanoparticles coexist, which have a noticeable influence on the catalysis performance.[208,209] The proportion of CO/H_2 products can be adjusted by altering the ratio of $Fe-N_4$ sites to Fe nanoparticles. For example, an Fe–N–C catalyst ($Fe_{0.5}$d) with no Fe nanoparticles and 1.5% Fe mass loading showed the best performance, indicating that $Fe-N_4$ is the active site for catalyzing CO_2 to CO.[210] Some studies also demonstrated that the Fe site bound to pyridine–nitrogen is the real active center for the CO_2RR by poisoning the active center through specific binding with $Fe-N_4$ without affecting the N–C site by using a reactant with good affinity to the Fe site (such as SCN^-).[211] At present, the structure of FeN_x is usually based on MOFs as the carbon framework (such as ZIF-8), and then iron ions are further adsorbed using the vacancy generated by the volatilization of Zn at high temperature to capture Fe to obtain the structure of FeN_x.[137] Under the overpotential of 340 mV, the partial I_d reached 94 mA cm^{-2} with FE_{CO} = 90%.

The Fe^{3+} site is the key to the catalytic activity. It was also be proven that the activity of the catalyst decreases due to the reduction of Fe^{3+} to Fe^{2+} at -0.5 V. Moreover, Li *et al.*[213] stated that the Fe(ı) site generated *in situ* is the active site for the CO_2RR. The strong interactions between the d_{z^2} orbital with a single electron of Fe(ı) and the π^* orbital occupied by a single electron in [COOH] is the key to excellent CO_2RR activity. For the production of reduction products requiring more than $2e^-$, the larger desorption free energy of CO at the $Fe-N_4$ site may play a positive role. Simultaneously, the proper adsorption of *H on the surrounding sites can just combine with CO bound on the Fe center, which promotes the production of more than $2e^-$ reduction products.[214,215]

Recently, He *et al.*[206] designed an efficient method to prepare copper-SA and proposed the concept of effective single atoms. Through the construction of network interpenetrating and self-supporting structures, the probability of single atoms at the interface is greatly improved to avoid the loss of their catalytic activity due to embedding (Fig. 22a). Because a large number of effective single atoms is obtained, a high current density can be achieved at a low metal single-atom content, which has a certain practical application prospect. Carbon nanofiber films (CuSAs/TCNFs) can be prepared with a size of $\sim$300 cm^2 under laboratory conditions, which have good conductivity and mechanical strength. After cutting, they can be directly used as working electrodes for the CO_2RR without any adhesive agents. The self-supporting through hole structure of the catalyst can prevent the active site from being embedded
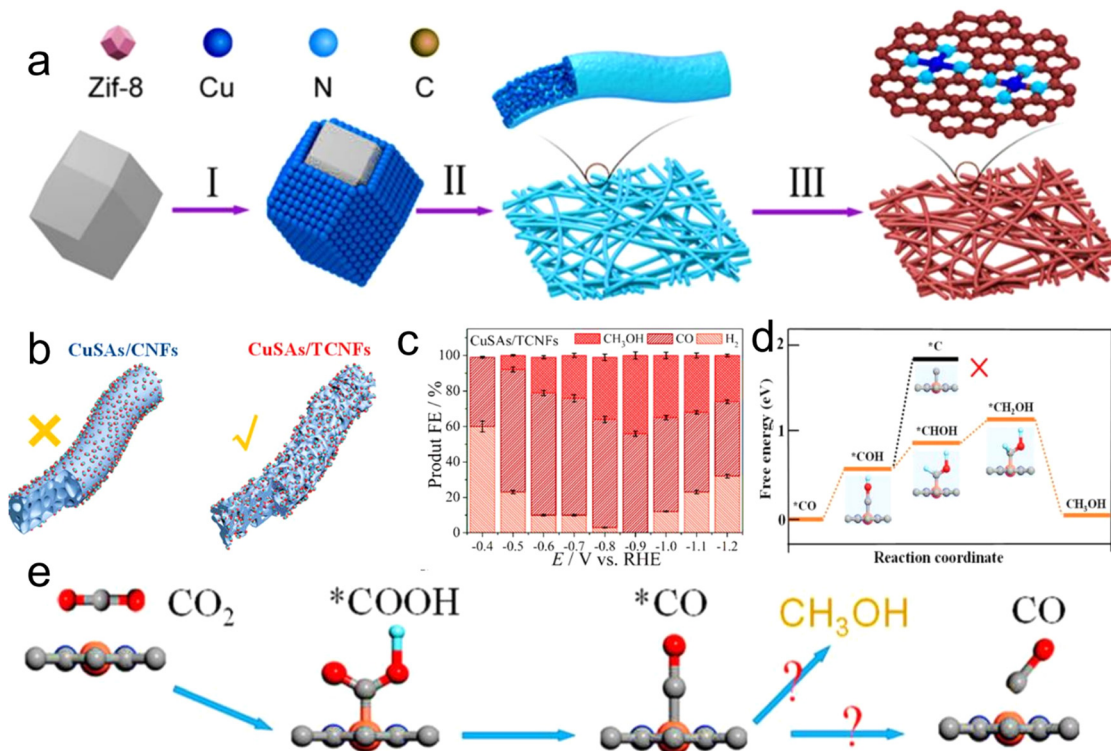
Fig. 22 (a) Synthesis of Cu single atom. (b) Illustration of CO_2 diffusion on two samples. (c) FEs of products. (d) Free energy model for the conversion of *CO to methanol. (e) Optimized atomic structures of CuSAs/TCNFs and proposed reaction paths for CO_2 electroreduction. Reproduced with permission from ref. 206 Copyright 2019, ACS.

inside, forming an enormous copper-single atoms, which can participate in the CO_2RR (Fig. 22b). CuSA/TCNF films could be used for the CO_2RR in aqueous solution systems to obtain methanol with 44% FE and the partial I_d of the C_1 product reached -93 mA cm^{-2} (Fig. 22c). In addition, the CuSA/TCNF film could be used stably for more than 50 h without significant degradation in its performance. DFT calculation showed that Cu–N_4–C structure can effectively reduce the Gibbs free energy of the *COOH intermediate and improve the catalytic activity of CuSAs/TCNFs. Simultaneously, Cu–N_4–C has good adsorption ability for the *CO intermediate, which can further reduce the *CO intermediate to methanol (Fig. 22d and e). In addition, the hierarchical pore structure of CuSAs/TCNFs can improve the electrochemical active area, enhance the CO_2 adsorption capacity, and increase the effective active sites for the CO_2RR, leading to a higher current density. Zu et al.[216] realized the synthesis of positive-charged single atoms of Sn ($Sn^{\delta+}$). The structure and morphology of the catalyst were confirmed by XAFS and HAADF-STEM characterization. In situ FTIR showed that $Sn^{\delta+}$ activated CO_2 and realized the subsequent protonation process by stabilizing the $CO_2^{\bullet-}$ and $HCOO^-$* intermediates. Simultaneously, nitrogen doping also promotes the desorption process of the decisive $HCOO^-$ step. Therefore, the initial potential of $HCOO^-$ generation was only -60 mV and the TOF of $HCOO^-$ at -1.8 V reached 11 930 h^{-1} vs. SCE. Furthermore, its electroreduction activity could be maintained for 200 h. They also synthesized an Sn_1/CuO composite

single-atomic catalyst with oxygen vacancies through metal support interaction. Zhang et al.[217] obtained different morphologies at different pyrolysis temperatures and the structural characterization of the different materials is shown in Fig. 23. Fig. 23f shows that Bi in BiSAs/NC exists in the form of single-atomic dispersion. The catalyst achieved 97% FE_{CO} at a low overpotential and the TOF reached 5525 h^{-1}. DFT calculation showed that due to the low reaction energy barrier, the Bi–N_4 structure promotes the rapid formation of the CO intermediate *COOH. The nitrogen-doped porous carbon-supported Sb monoatomic catalyst synthesized by the calcination of urea and carbon black achieved efficient CO_2RR to CO, and the TOF_{CO} reached 16 500 h^{-1}.[218] In addition, another single-atom catalyst with Sb–N_4 structure exhibited selectivity of 94% for the CO_2RR to formate.[219] DFT showed that the Sb–N_4 site is more conducive to the formation of HCOO*, and thus the product is mainly formate rather than CO. This is different from the product reported in the previous Sb single-atomic catalyst. This may be due to the different preparation methods, resulting in a change in the electronic structure of the single-atomic site, and the intermediate conducive to adsorption changes from *COOH to HCOO*. In terms of catalyst preparation method, Sb–N_4 on nitrogen-doped carbon is mainly obtained by co-pyrolysis of $SbCl_3$ with dicyandiamide and pyromellitic acid. In situ XAFS and DFT confirmed the presence of $Sb^{\delta+}$–N_4. It is favorable for the CO_2RR to $HCOO^-$ to occur at the N_4 site. For these reported catalysts, their FE reached a relatively high level,
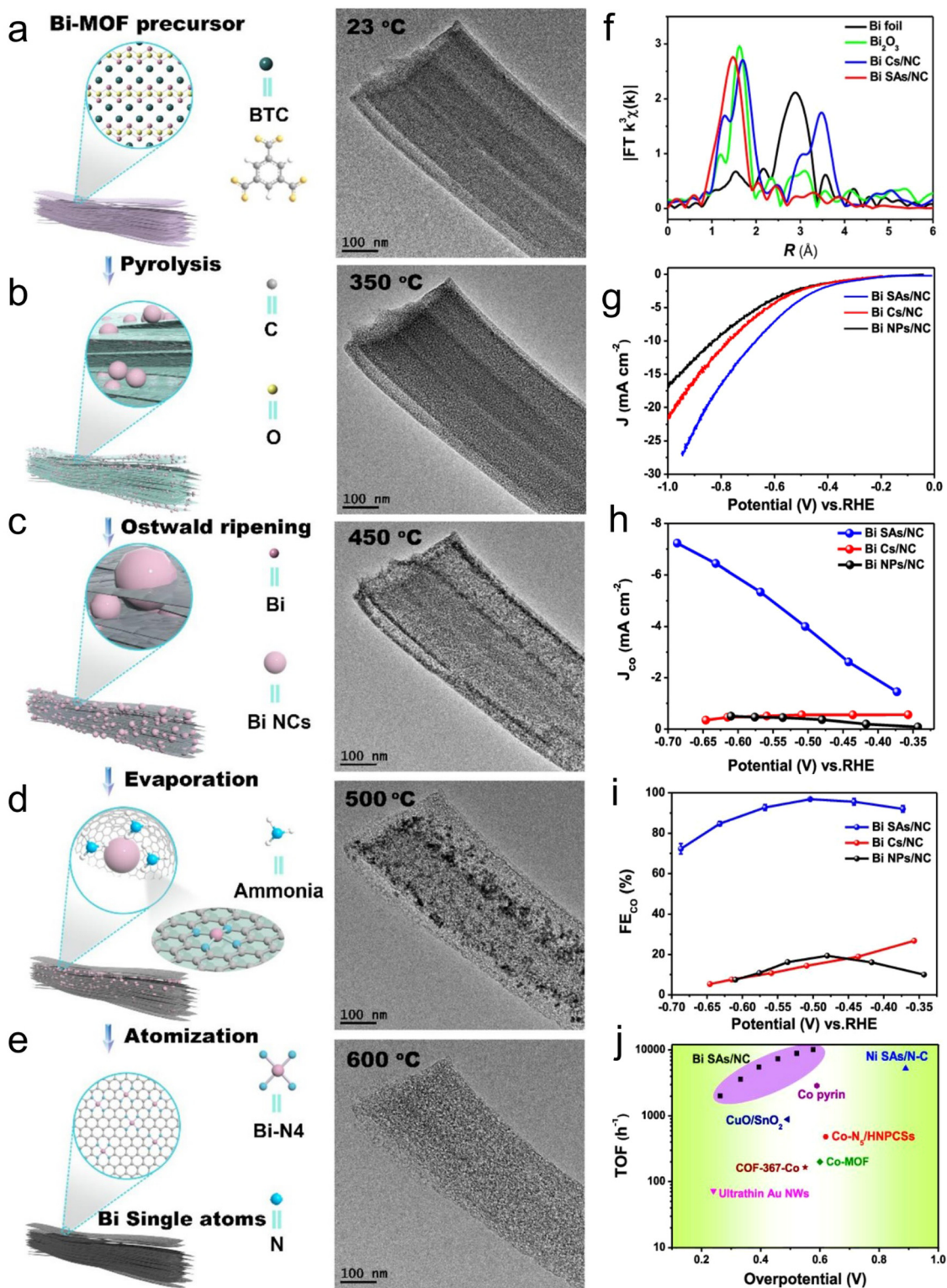
Fig. 23 (a–e) Illustration of the transformation of Bi-MOF to Bi-SA together with corresponding TEM images. (f) EXAFS spectra with $k^3\chi(k)$ function. (d) LSV curves. (h) Partial current densities of CO. (i) FE_{CO} and (j) comparison of TOF values. Reproduced with permission from ref. 212 Copyright 2019, ACS.

but the current density is still low and far away from the requirement for industrial use (1 A cm^{-2}).

Furthermore, Wang *et al.*[33] reported the preparation of a type of N-heterocyclic carbene-linked MOF and copper single-

atomic center (2Bn–Cu@UiO-67, where Bn is di-benzyl imidazole). Under the condition of I_d of 420 mA cm^{-2}, at −1.5 V the FE of CH$_4$ was promoted to as high as 81%. It is worth noting that the FE_{CH_4} of the catalyst remained above 70% in a wide

Table 3 The performance of MOF-derived carbon-based catalysts in the CO_2RR

Material	Precursor (MOF)	Main product	Electrolyte	faradaic efficiency [%]	Potential	Current density [mA cm^{-2}]	Ref.
NC	ZIF-8	CO	0.1 M KHCO$_3$	78	−0.93	−1.1	220
Fe–N–C	ZIF-8	CO	0.1 M NaHCO$_3$	91	−0.6	4.5	221
Fe–N–C	ZIF-8	CO	0.5 M KHCO$_3$	93.5	−0.5	NA	222
Fe–N–C	Zn–Fe ZIFs	CO	0.5 M KHCO$_3$	86.9	−0.47	NA	223
Ni–N–C	ZIF-8	CO	0.5 M KHCO$_3$	71.9	−0.9	NA	180
Zn Ni–N–C	Zn Ni–MOF	CO	1 M KHCO$_3$	NA	-1.03	71.5 ± 2.9	224
Ni$_{SA}$–N$_x$–C	Mg–Ni–MOF-74	CO	0.5 M KHCO$_3$	98	−0.8	NA	225
Co–N–C	Zn–Co MOF	CO	0.1 M KHCO$_3$	82	−0.8	NA	226
Co–N–C	Zn–Co ZIF	CO	0.5 M KHCO$_3$	94	−0.63	18.1	227
Bi–N–C	Bi MOF	CO	0.1 M NaHCO$_3$	97	−0.5	3.9	217
Cu–N–C	Cu-doped ZIF-8	CH$_3$COCH$_3$	0.1 M KHCO$_3$	36.7	−0.36	NA	228
Ni/Fe–N–C	Zn/Ni/Fe ZIF	CO	0.5 M KHCO$_3$	98	−0.7	7.4	187
Fe–N–C/CNTs	ZIF-8	CO	0.1 M KHCO$_3$	97	−0.56	1.9	229
Ni–NPC/CNTs	ZIF-8	CO	0.5 M KHCO$_3$	94	−0.77	11.2	230
Cu/Cu$_2$O/NPC	ZIF-L	C$_2$H$_5$OH	0.5 M KHCO$_3$	70.52	−0.87	10.4	231

potential range and reached an unprecedented 16.3 s^{-1} TOF, which is almost the best CH$_4$ electrosynthesis catalyst thus far. The researchers chose UiO-67 as the substrate material to load the SAS active center connected by NHC, which can well match the molecular size of NHC and remain stable for several hours in aqueous solution. Simultaneously, the porosity of the catalyst promoted the diffusion of CO$_2$ to 2Bn–Cu, thus significantly improving the utilization of each catalytic site. The design of this NHC-linked Cu-SAS catalyst has great advantages in methane electrosynthesis, providing a new idea for the industrial production of methane. To compare the CO$_2$RR performance of MOF-derived catalysts, a summary of the latest results of the CO$_2$RR is given in Table 3.

7.5 MOF-derived diatomic catalyst

The development of diatomic catalysts (DACs) for the CO$_2$RR has become a promising frontier research field due to its efficient atom utilization and complex functions. However, the design of DACs at the atomic level and the understanding of the two-site synergistic mechanism are still challenging. Recently, He et al.[232] reported that with the help of an MOF, a novel N$_4$Ni/CuN$_4$ bi-site catalyst was developed (Fig. 24a). The crystal structure of the MOF provides ordered and periodic space to classify positions and adjust the relative space distance between the Cu and Ni precursors, which were doped in the form of metal nodes and encapsulated in the cavity of ZIF-8. Therefore, ordered Cu and Ni precursors are conducive to the formation of Ni/Cu adjacent sites after one-step thermal activation.

The experimental results showed that the catalyst containing N$_4$Ni/CuN$_4$ has excellent catalytic activity and selectivity for the CO$_2$RR. At −0.79 V (vs. RHE), the FE$_{CO}$ reached up to 99.2%, and in the range of −0.39 to −1.09 V (vs. RHE), it reached more than 95% (Fig. 24b). In addition, at −1.09 V, the TOF value was 6895 h^{-1}, while that of Ni–N–C and Cu–N–C was 5119 and 2500 h^{-1}, respectively. Further DFT calculations showed that the synergistic effect between heteronuclear monomers can also be achieved by metal atoms that exhibit similar bonding interactions with the intermediates such as Ni and Cu. Among them, the charge redistribution of the Ni centers caused by

adjacent CuN$_4$ sites promotes the adsorption of *COOH, thereby promoting the formation of CO (Fig. 24d). Although the FEs of most Ni-based monoatomic catalysts (Ni–N–C) have achieved satisfactory results in the CO$_2$RR to CO (>90%), their high overpotential (>600 mV vs. RHE) still limits their practical application, which means that the energy consumption required to catalyze the CO$_2$RR is high. Combining the benefits of Fe–N- and Ni–N–C-based catalysts, Jordi et al.[234] described the design of a quasi-binary Ni/Fe catalyst to achieve high selectivity and low overpotential in the CO$_2$RR process (Fig. 24c). Here, due to the weak CO bonding, the Ni–N–C catalyst has the ability to quickly desorb *CO (CO* → CO^{+*}), while the Fe–N active center usually shows a low overpotential for the CO$_2$RR due to the fast transfer rate of electrons from the first proton coupling. Simultaneously, due to the synergy between the closely located Fe and Ni active centers, they act as a nanoreactor, considerably affecting the reaction steps of both active centers, thereby improving the activity and selectivity of the CO$_2$RR. In addition, in a specific environment, the presence of Fe near the Ni center will affect the electron density and conformation of the two active centers, consequently promoting the adsorption/desorption of the intermediates in the CO$_2$RR. The researchers prepared ternary MOFs via a one-pot solvothermal method as an alternative to the complex and multi-step process, and by reasonably controlling the amount of Fe and Ni added to IrMOF-3, which is Zn based. Then, the adjacent Fe and Ni double-active centers are prepared by calcination. The experimental results showed that the as-synthesized Ni$_7$/Fe$_3$–N–C material displayed a good FE$_{CO}$ of 98% at a low overpotential of −390 mV vs. RHE, which it is greater than that of the single metal catalysts of Fe and Ni. DFT calculations showed that this bimetallic catalyst with adjacent Ni and Fe centers is more favourable for the production of COOH* than the Ni–N–C catalyst. In addition, the Ni/Fe–N–C catalytic material not only promoted the desorption of CO*, but also avoided the undesirable HER side reactions compared with the Fe–N–C catalyst, achieving unexpected catalytic activity for the CO$_2$RR (Fig. 24e). Therefore, the exceptional high catalytic activity can be ascribed to the Fe and Ni centers, which play a synergistic role in regulating the binding energy of the various
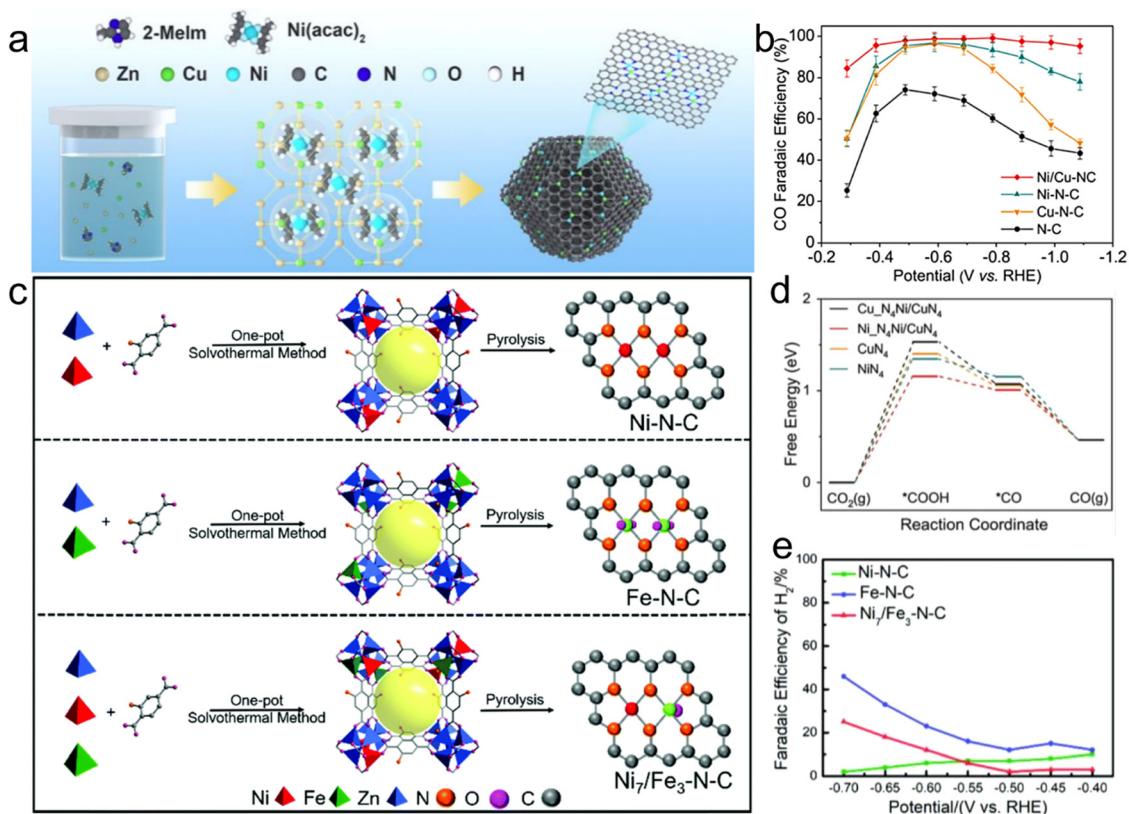
Fig. 24 (a) Schematic description of Ni/Cu−N−C fabrication. (b) FE_{CO}. Reproduced with permission from ref. 233 Copyright 2022, ACS. (c) Method for the synthesis of different metal-based catalysts. Reproduced with permission from ref. 234 Copyright 2021, RSC. (d) Free energy diagram for CO_2 conversion. Reproduced with permission from ref. 233 Copyright 2022, ACS. (e) FE of H_2 for various catalysts. Reproduced with permission from ref. 234 Copyright 2021 RSC.

intermediates throughout the desorption and adsorption process and affecting the different reaction steps of the CO_2RR. Recently, Liang *et al.*[235] reported the preparation of novel Bi–In alloy nanoparticles from bimetallic MOFs, considered as an active method to solve the environmental and energy crises. The FE_{HCOOH} of 92.5% at I_d of 300 mA cm^{-2} with 5170 µmol h^{-1} yield was achieved. In the membrane electrode assembly system, the stability of Bi–In material was also very good. Under the I_d of 120 mA cm^{-2}, the nanoparticles with an Fe content of less than 10% showed excellent stability for more than 25 h. *In situ* spectra and theoretical results showed that the BiIn bimetallic center can provide the best binding energy for *OCHO intermediates, thus accelerating the conversion of CO_2 to HCOOH.

The use of organic framework-based catalytic materials in the CO_2RR to valuable products has the potential to adjust the catalytic performance by tuning the characteristics of the framework chemically and physically with atomic distribution accuracy. Nevertheless, the adjustable performance of these functional materials is still greatly hindered by their poor conductivity. Mirica *et al.*[236] demonstrated that four structural analogues of 2D cMOF made of metal phthalocyanine (MPc) ligands connected by copper phthalocyanine have a conductivity in the range of 2.73×10^{-3} to 1.04×10^{-1} S cm^{-1} and can

used for CO_2RR to CO (Fig. 25a). The catalytic performance (including activity and selectivity) of the MOF was hierarchically controlled *via* two key factors, *i.e.*, the metal (M = Ni and Co) subunits in MPc and heteroatom cross linkers (X = NH *vs.* O) between these subunits. The catalytic performance dominantly depended on the selected metal, and additionally regulated by heteroatom bonds. CoPc–Cu–O displayed high selectivity (FE_{CO} = 85%) with I_d of 17 mA cm^{-2} under an overpotential of −0.63 V. Without the addition of carbon additive, the current density of −9.5 mA cm^{-2} was achieved by using CoPc–Cu–O purely as the catalytic electrode, and the FE_{CO} was 79% (Fig. 25b–e).

The reaction mechanism was determined through comparative experiments with phthalocyanine MOF having no metal atom analogues, which supported the main catalytic action of the phthalocyanine central metal on the Cu node (Fig. 25f). DFT calculation further showed that compared to analogues based on NiPc and -NH linkage, the MOFs based on CoPc and O linkage have inferior activation energy in the production of carboxyl intermediates, which is consistent with their higher selectivity and activity. This study demonstrated that 2D-MPc with conductive frame materials has great hope to achieve effective carbon dioxide fixation through tactical linker engineering with multi-level adjustability. These works emphasize
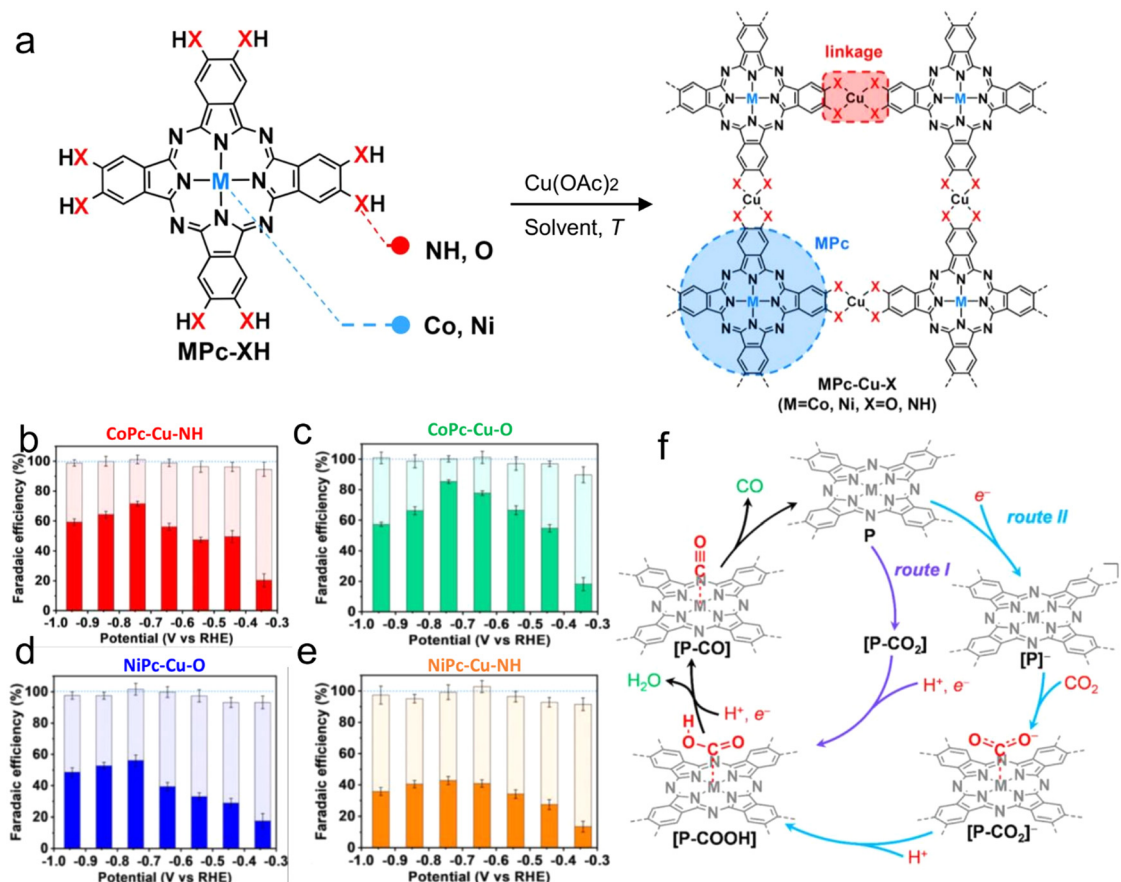
Fig. 25 (a) Synthesis scheme of MPc–Cu–X MOFs. (b–e) FEs of H_2 product for different (catalysts). (f) Suggested mechanism for catalytic electrochemical reduction of CO_2 to CO on MPc–Cu–XH MOFs. Reproduced with permission from ref. 236 Copyright 2020, ACS.

the important role of synergetic adjacent bimetallic materials as promising CO_2RR electrocatalysts and reveal that these bimetallic centers can well serve as a double-site nanoreactors, affecting different reaction steps of different active centers with electronic and atomic engineering structures, which probably support the application potential of DACs in various fields.

8. Regulation of catalyst microenvironment

It is also one of the key aspects that is widely studied in current research to regulate the microenvironment of single atoms to change the intrinsic catalytic properties of the original single atoms. The regulation of the coordination environment of single atoms of non-noble metals can further improve the catalytic performance, even to a level equivalent to that of noble catalysts. This method avoids the use of expensive noble metal catalysts, and instead selects abundant metal elements, which has potential to realize large-scale industrial applications.

8.1 Heteroatom coordination

8.1.1 Synthesis method. The synthesis method can regulate the charge density of the metal center with the heteroatoms

coordinated with the metal atoms, fine tune the binding strength of the metal center with the intermediate in the CO_2RR process, and finally achieve the highly selective and high-yield synthesis of the target product.[237] Liu *et al.*[238] used the organic linker ligand H_3BTC and $In(NO_3)5H_2O$ to synthesize In-MOF. Later, after physical mixing with dicyandiamide, In_A/NC with $In–N_4$ structure was obtained *via* one-step pyrolysis. The control experiment and DFT calculation showed that it is different from In in another study on $In^{\delta+}–N_4$ structures.[185] The In–N site of In_A/NC is not only conducive to the dissociation of COOH* to generate CO, but also hinders the formation of formate, making it more selective to CO than to formate. Simultaneously, because the structure of $In–N_4$ maintains the alkaline environment near the catalytic interface, it also weakens the reduction of hydrogen protons. Furthermore, the use of an ionic liquid as the electrolyte not only increases the concentration of CO_2 substrate, but also inhibits the occurrence of the hydrogen evolution side reaction.[238] These factors jointly promote the reduction of CO_2 to CO, showing an FE_{CO} of 97.2% at 39.4 mA cm^{-2} and a high TOF (about 40 000 h^{-1}, Fig. 26a–d). This method of adjusting the single-atom coordination environment to change the selectivity of the products lays the foundation for further exploring the single-atom structure-performance relationship. Considering the low current density
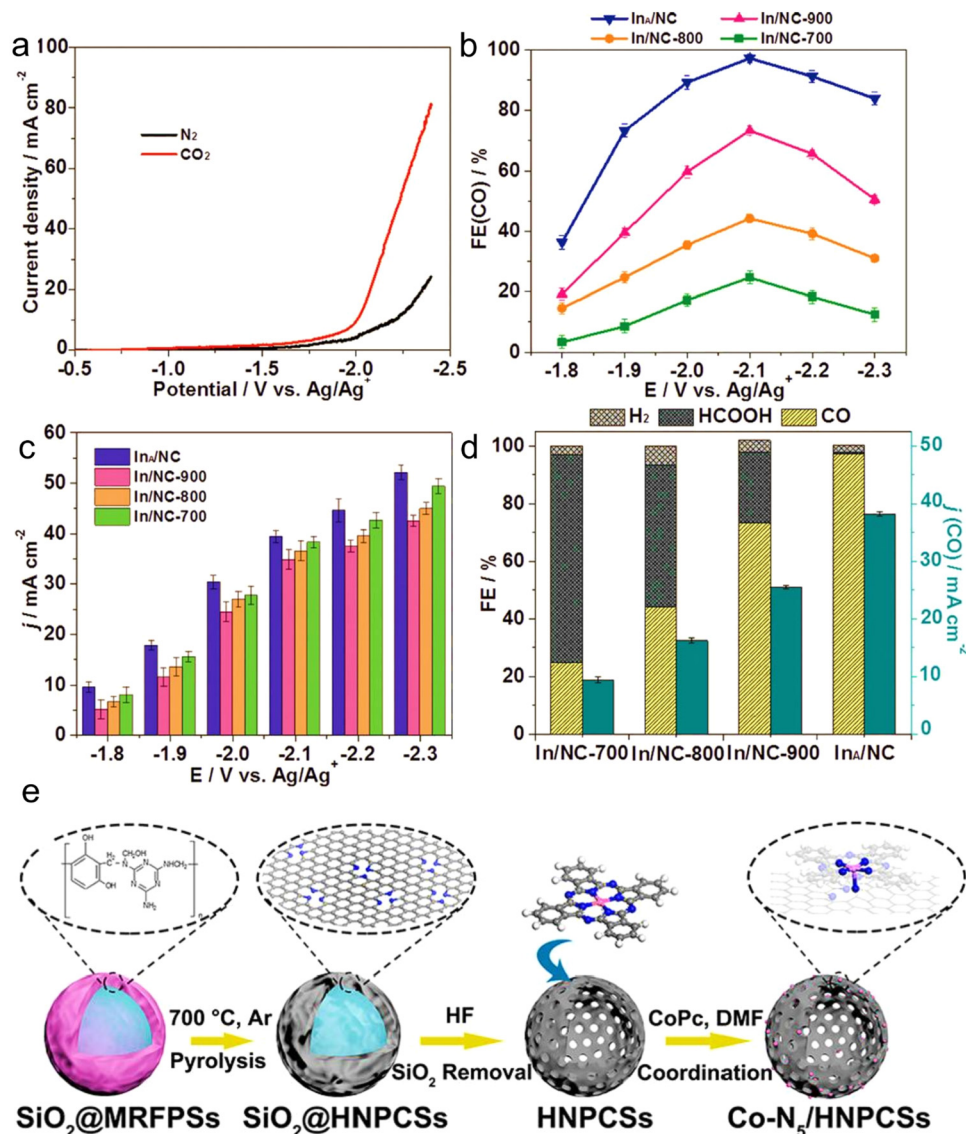
Fig. 26 (a) LSV curves for In_A/NC catalyst. (b) FEs and (c) partial current densities over for CO. (d) FEs of formate, H_2 and CO. Reproduced with permission from ref. 238 Copyright, 2021 ACS. (e) Schematic of the synthesis of Co–N_5/HNPCSs. Reproduced with permission from ref. 241 Copyright 2018, ACS.

of the CO_2RR at present, Chen *et al.*[239] proposed a novel amination strategy to improve the current density of Ni monatomic catalysts for the CO_2RR. Ni–N_4/C formed by pyrolytic Ni-doped ZIF-8 was co-heated with urea, and then reacted with ammonia *via* the hydrothermal method to achieve the amination of the Ni monatomic catalyst. FTIR and XPS both proved the successful modification of -NH_2. Tests in a flow-cell showed that the FE$_{CO}$ was close to 90% at −0.89 V, and the I_d significantly increased to 450 mA cm^{-2}, which can be ascribed to the fact that -NH_2 adjusted the electronic structure of the catalyst and enhanced the adsorption and charge transfer efficiency of the *CO_2 and *COOH intermediates.

8.1.2 Adjusting the number and type of coordination atoms. In the case of Fe SACs, it has been reported that the addition of extra N-coordination atoms at the Fe site can

promote the CO_2RR efficiency. Yang *et al.*[240] first reported that catalysts containing Fe–N_5 sites are carbonized by electrospinning in an inert atmosphere and nitride in an ammonia atmosphere. A composite structure catalyst was constructed to encapsulate Fe$_x$N nanoparticles in a graphite layer embedded with Fe–N_4 sites.

The catalyst achieved an FE$_{CO}$ of and partial current density of 4.7 mA cm^{-2} at −0.53 V. The coordination effect of N in Fe$_x$N on the Fe sites effectively solved the problem of catalyst poisoning caused by the excessive combination of CO and Fe sites.[222] The catalyst with a clear Fe–N_5 site was obtained *via* the co-pyrolysis of Fe, melamine and graphene, and subsequently leaching with sulfuric acid. Without the addition of graphene, only an SAC with Fe–N_4 site structure could be obtained. During the pyrolysis of melamine, the introduced graphene is

mixed with nitrogen heteroatoms and the Fe–N$_4$ sites dispersed on this support will coordinate with the additional N atoms axially, forming Fe–N$_5$ sites. Based on this, the FE$_{CO}$ of the catalyst was about 97% at the overpotential of 0.35 V. Theoretical calculation showed that the additional axial coordination further reduces the electrons in the Fe 3d orbital, thus reducing the feedback π bond between Fe and CO, and thus CO is easier to desorb from the Fe site.[242] The Co–N site can also enhance the selectivity of the CO$_2$RR by introducing additional N coordination atoms. Chen *et al.*[241] prepared hollow nitrogen-doped carbon spheres *via* a templating method and obtained electrocatalysts with a Co–N$_5$ coordination configuration by impregnating and adsorbing cobalt phthalocyanine (CoPc). The nitrogen atom in the hollow nitrogen-doped carbon ball was used as an additional nitrogen source to bond with the Co–N$_4$ site in CoPc. A schematic diagram of its synthesis is shown in Fig. 26e. *In situ* XANES characterization determined that the catalytic active site is Co–N$_5$. The catalyst maintained an FE$_{CO}$ of more than 90% in a wide voltage window (-0.57 to -0.88 V), and an FE$_{CO}$ of greater than 99% in the window of -0.73 to -0.79 V. Simultaneously, after 10 h testing, the current density and FE exhibited almost no change, indicating that the catalyst has good stability. Theoretical calculations further explained that the formation of *COOH on the Co–N$_5$ site requires a lower free energy, and CO desorption is easier. A similar trend can be found by comparing Co–N$_4$ site with Co–N$_{4-x}$–C$_x$. At -0.8 V *vs.* RHE, the former exhibited an FE$_{CO}$ of 82%, while that of the latter was 47%.[226] In addition, by comparing the influence of the Ni–C/Ni–N coordination environment on the electrocatalysis performance, the results showed that a change in the coordination microenvironment will lead to a change in performance, which further confirms the above-mentioned conclusion.[243] It is notable that in their early work on studying the effect of the coordination number on catalytic performance, they presented different rules. With a reduction in the coordination number of the N-atom, the selectivity of CO increased. By adjusting the annealing temperature, Co–N$_x$ with different coordination numbers was obtained, where upon increasing the temperature, the value of x also decreased gradually. Among them, Co–N$_2$ showed the most outstanding performance. At 520 mV overvoltage, 94% CO FE was achieved. The corresponding partial J was -18.1 mA cm^{-2}. Theoretical research showed that the reduction of the coordination number of the N atom near the Co atom produces more unfilled orbitals of 3d, which is conducive to CO$_2^{\bullet-}$ adsorption. Simultaneously, Co–N$_2$ has the lowest charge transfer impedance, that is, it promotes the activation of CO$_2$, accelerates the charge rate, and leads to an improvement in the CO$_2$RR performance.[181] Obviously, the coordination modes of the N atom and central Co atom in these two studies are different. The former increases the axial coordination, while the latter decreases the in-plane coordination, and the reduced N atom is replaced by a C atom. Moreover, these outcomes further show that changing the coordination mode of the coordination atom will significantly affect the catalytic performance. Similarly, by changing the pyrolysis temperature,

Jiang *et al.*[225] prepared several Ni$_{SA}$–N$_{4-2}$–C catalysts. Among them, Ni$_{SA}$–N$_2$–C exhibited better catalytic activity than Ni$_{SA}$–N$_3$–C and Ni$_{SA}$–N$_3$–C. Its highest FE$_{CO}$ reached 98% and its TOF$_{CO}$ was 1622 h^{-1}. The catalyst with Ni–N$_2$ site was successfully obtained through plasma-assisted method and nitrogen vacancy-induced coordination reconstruction strategy. Due to its special electronic structure, the free energy barrier for CO$_2$ molecule adsorption and activation was lower.[244] Thus, this catalyst could achieve 96% FE$_{CO}$ at a low overpotential (590 mV), and J reached 33 mA cm^{-2} at an overpotential of 890 mV. In addition, considering the charge capacity and hydrogen bond interaction, theoretical calculation further indicated that Ni–N$_1$C$_3$ has higher activity and selectivity than its counterparts in the series (Ni–N$_x$C$_{4-x}$).[245] Recently, Zheng *et al.*[245] reported a plasma activation strategy for the synthesis of Cu-based MOF single-atomic catalyst. The oxygen atoms in the catalyst that were previously coordinated with Cu were partially removed by plasma treatment, thus forming a low-coordination Cu single-atomic site rich in oxygen vacancies. Simultaneously, plasma treatment also led to the porous nature of the material. The low-coordination Cu single-atomic and hierarchical porous structures jointly promoted the CO$_2$RR. The electrochemical performance showed that the maximum FE of CH$_4$ reached 75.3%. The selectivity for the CO$_2$RR products reached 96.5% with a J of 48 mA cm^{-2}. In addition to the vacancies generated by the reduction in the number of N-coordination atoms described above being replaced by C atoms, it has also been reported that Ni–N$_x$V$_{4-x}$ catalysts (where V represents defects, *i.e.*, no coordination atoms) can inhibit the HER.[224] This SAC containing coordination unsaturated Ni was obtained *via* the calcination of ZIF-8 containing Ni, and the mass loading of Ni reached 5.44%, which is higher than that reported in the literature. Another study showed that the Ni–N$_3$ site promoted CO production from the CO$_2$RR with FE$_{CO}$ exceeding 90%, and the conversion frequency reached up to 12 000 h^{-1} with the mass activity of 10 600 mA mg^{-1}.[246] Based on the weak interaction between Ni–O, Lu *et al.*[247] directly pyrolyzed the precursor containing Ni(II)–N/O. With the removal of O, vacancy V was generated, and the structure of Ni–N$_3$–V was obtained. The catalyst showed a much better performance than the Ni–N$_4$ single atom, with a TOF of 1.35×10^5 h^{-1}, which is 4 times larger than that of Ni–N$_4$. In conclusion, these results prove the advantages of the Ni–N(S)$_x$V$_{4-x}$ configuration.

Besides the coordination number, exchange of the coordination atom is another strategy for regulating the electrocatalytic activity of single atoms. The introduction of atoms with lower electronegativity can decrease the energy graph of the intermediates in the CO$_2$RR process, and ultimately accelerate the reaction kinetics. On the carbon-based plane, the asymmetric Cu–S$_1$N$_3$ atomic interface has an optimized *COOH binding energy compared with the Cu–N$_4$ site. In addition, the nearby Cu nanoparticles (Cu$_x$) promote the protonation process. Therefore, Cu–S$_1$N$_3$/Cu$_x$ showed nearly 100% FE$_{CO}$ at the voltage of -0.65 V, and maintained more than 90% FE$_{CO}$ in the voltage range of -0.55 to -0.75 V, which is superior to Cu–N$_4$ (FE$_{CO}$ = 54% at the voltage of -0.7 V) and Cu–S$_1$N$_3$

(FE_{CO} = 70% in the potential range of 0.7 to 3 V).[251] Zhang et al.[252] obtained a Cu–O_4 site catalyst (Cu–DBC) by connecting unit point Cu at the MOF node. The methane selectivity of this catalyst was close to 80%, and under the same condition, the partial I_d reached −203 mA cm^{-2} at −0.9 V (vs. RHE), where the Cu–O_4 site has a lower CO_2RR reaction barrier than the Cu–N_4 site Ni–N_2–S obtained by S doping. Ni–N_2 will generate S-vacancy under the condition of high overpotentials, and both the S-atom and S-vacancy can reduce the reaction energy graph of CO_2 to CO. Consequently, the FE_{CO} of the catalyst reached 97% under the condition of −0.8 V vs. RHE, with the CO partial I_d of 40.3 mA cm^{-2} under the condition of −0.9 V (vs. RHE).[253] Furthermore, changing the type of coordination heteroatom can also affect the reaction path and generate different products. For example, SnN_3O_1 shows unique properties compared with the main products of Sn–N_4, i.e., HCOOH and H_2, and the main product CO. Theoretical calculation showed that the SnN_3O_1 configuration can reduce the energy barrier of *COO activation and *COOH formation.[254] In Cd–N_4S_1, the S atom is axially coordinated with the Cd atom, while the Cd atom is anchored on the graphite carbon plane of Cd–N_4.[248] The structure diagram is shown in Fig. 27a, where the axial S atom

coordination not only reduces the energy graph of CO_2RR, but also inhibits the HER. Consequently, Cd–N_4S_1 showed a superior CO_2RR performance, reaching a CO partial I_d of 182.2 mA cm^{-2} with FE of more than 95% in an H-type electrolytic cell. Also, the TOF reached 73 000 h^{-1}, which is the best performance reported to date in an H-type electrolytic cell. Theoretical calculation showed that the Cd–N_4S_1 single atom has an influence on reduction of the energy graph of the CO_2RR compared with Cd–N_4. Sn–O_x mononuclear species were anchored in carbonized ZIF-8 by chemical vapour deposition. Then, further fluorination was achieved by etching ZIF-8 with C_2F_4 generated from the pyrolysis of polytetrafluoroethylene, and finally a single-atom electrocatalyst with Sn–C_2O_2F structure was synthesized. It could maintain an FE_{CO} of 90% in a wide potential range (−0.2 to −0.6 V). Under the same conditions, formate (up to 95.2%) was the main product of Sn–N_4. The adsorption of the intermediates was optimized through the coordination regulation of the C and O atoms, while the introduction of axial F atoms inhibited the HER side reaction and promoted the conversion of CO_2 to CO.[249] However, as shown in Fig. 27b–e, compared with Sn–C_2O_2, the formation energy barrier of *COOH + H$^+$ also increased to a
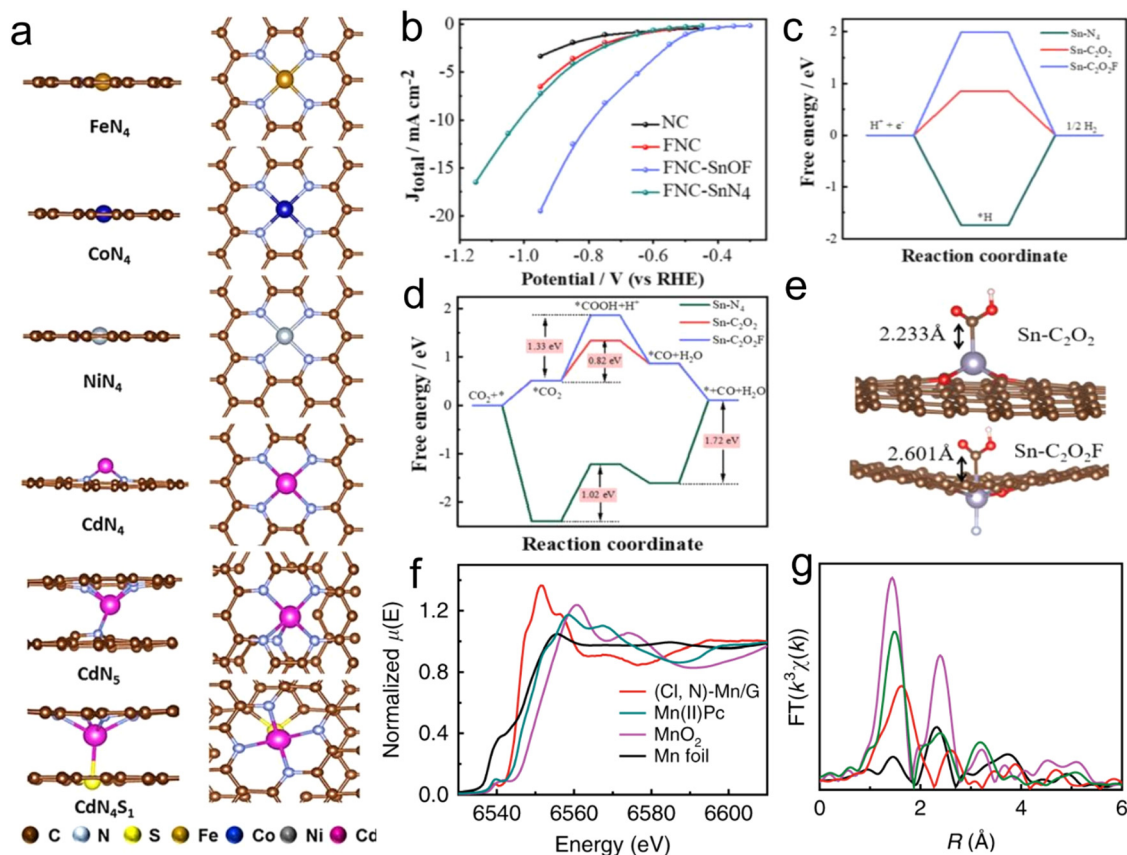

Fig. 27 (a) Top and side views of different metal nitride catalysts, Reproduced with permission from ref. 248 Copyright 2021, Wiley. (b) J_{Total} of NC, FNC, FNC−SnOF, and FNC−SnN$_4$ measured by the controlled potential electrolysis with a carbon paper electrode. (c) Free energy diagram for HER. (d) Free energy diagrams for CO_2 conversion to CO. (e) Adsorption configurations of *COOH on Sn−C_2O_2 (top) and Sn−C_2O_2F (bottom). Reproduced with permission from ref. 249 Copyright 2021, RSC. (f and g) EXAFS and XANES spectra at Mn K-edge. Reproduced with permission from ref. 250 Copyright 2019, Nature Springer.

certain extent when the HER is inhibited. Based on this, under the overpotential of 490 mV, the FE_{CO} of the catalyst was 90.5% and I_d was 10.8 mA cm^{-2}, with the TOF reaching 1566 h^{-1}. Zhang et al.[250] clarified through DFT calculations and in situ XAS that the introduction of axial Cl coordination atoms can effectively decrease the energy of formation barrier of key intermediates at the Mn–N$_4$ site. The structural characterization results are shown in Fig. 27f and g. Under the overpotential of 0.49 V, the CO I_d was about 10 mA cm^{-2}, and the maximum FE was 97%. The above-mentioned study showed that the introduction of axial coordination heteroatoms shows different properties for different metal single-atomic sites. In addition, Chen et al.[255] synthesized an Fe$_1$N$_4$–O$_1$ catalyst through the molten-salt assisted strategy, rapid pyrolysis and controllable activation strategy. Although its oxygen atom was also located in the axial coordination position, this oxygen atom is located in another graphite carbon plane. It is different from the former in that, it is independent of the out-of-plane oxygen atom. This oxygen atom can localize the electrons, promote the desorption of CO, and improve the energy barrier of HER. Therefore, the catalyst could obtain nearly 100% FE_{CO} in the voltage range of −0.56 to −0.87 V. Heteroatoms that do not directly coordinate with the metal will also affect the electronic structure of metal single atoms. For example, in the third coordination shell, the P atoms in the form of P–C bonds will enhance the electronic localization of the Fe single atom.[256] Thus, the stability of the *COOH intermediate is enhanced, showing 97% CO selectivity at a low overvoltage (320 mV).

In summary, most of the research focused on optimizing the local electronic structure, adjusting the adsorption and binding strength of intermediates, and achieving high selectivity of target products by finely regulating the coordination number of metal single atoms, the types of heteroatoms in coordination, and the coordination structure. Thus, further research is needed on the impact of this strategy on the overall activity of SACs.

8.1.3 Coordination environment-dependent selectivity. Among the products, CO$_2$RR for hydrocarbons has broad prospects, but the side reactions and slow reaction rate result in low activity, selectivity, and poor durability. Due to the interference of the HER and transfer of several electrons in the reaction process, the selectivity of the CO$_2$RR for multi-carbon products will be low. As an electrocatalyst for the CO$_2$RR, the microenvironment coordination of the active metal centers in MOFs plays a decisive role. However, the structure-performance relationship of the CO$_2$RR catalyzed by MOFs is still unclear. At present, copper (Cu)-based electrocatalysts can promote the conversion of CO$_2$ to multi-carbon products with satisfactory FEs, but their hydrocarbon selectivity is still low. Based on this, Sun et al.[257] synthesized a number of MOFs through altered Cu(I) microenvironment coordination (Cu-, Cl, Br and I), and evaluated their CO$_2$RR performance. These researchers used halogen atoms in the same family to finely tune the coordination microenvironment of Cu-MOFs, and prepared a series of MOFs based on Cu$_4$X clusters ([Cu$_4$X (TIPE)$_3$]·3X, [X = Cl, Br, I, TIPE = 1,1,2,2-tetrakis(4-(iminazol-1-yl) phenyl) ethane], named

Cu–I, Cu–Br, and Cu–Cl). The experimental results showed that Cu–I achieved an FE of 83% in the CO$_2$RR with Cu-, Cl, and Br and I_d of 88 mA cm^{-2} over −1.08 V against RHE; The FE_{CH_4} was higher than 50% in a wide potential range (−1.08 to −1.48) vs. RHE (Fig. 28a, b and d). At −1.08 V, the maximum FE_{CH_4} was 57.2%, and the partial I_d was 61 mA cm^{-2}. In contrast, the highest FE_{CH_4} of Cu–Cl and Cu–Br at −1.28 vs. RHE was only 32.9% and 40.2%, respectively. DFT calculation was used to understand the extraordinary selectivity of Cu–I for the CO$_2$RR to CH$_4$. The potential-determining steps (PDS) for the conversion of CO$_2$RR to CH$_4$ on Cu–X are *CH$_2$O and *CH$_3$O. With thine increase in the halogen atom radius, the formation energies of *CH$_2$O and *CH$_3$O gradually decreased (Cu–Cl was 1.59 and 1.76 eV; Cu–Br was 1.05 and 1.17 eV; and Cu–I was 0.94 and 0.33 eV, respectively). Furthermore, the energy of formation of *CH$_2$O and *CH$_3$O on Cu–I was small, displaying exceptional catalytic activity for CO$_2$RR to CH$_4$. In general, this work clarified the relation between the microenvironment coordination of active centers and the CO$_2$RR catalyzed by MOFs, and demonstrated the possibility of optimizing the CO$_2$RR performance by adjusting the coordination microenvironment of the metal sites in MOFs.

It has been found that the use of single-center catalysts (SSCs) is a favourable approach to attain high selectivity and true catalysis, but most reported SAC materials tend to form more than 2e$^-$ product instead of multi-carbons. Simultaneously, except for the single-atom sites of nitrogen coordination, few studies have been conducted on the single metal sites of other heteroatom coordination. Although crystalline SSCs can achieve controllable structure and metal site coordination, low conductivity still a serious issue for crystalline catalytic materials. The cMOF materials are assembled with transition metals with conjugated organic linkers, having unique redox, conductivity and MOF-based characteristics. Although some progress has been made in the application of cMOF in the CO$_2$RR, the research on cMOF electrocatalysts is still rare. Zhang et al.[252] reported the preparation of a Cu-based cMOF (Cu-DBC) using graphene-like highly conjugated linkers and Cu sites, and used it as a highly effective electric catalyst for the CO$_2$RR. It was found that highly conjugated organic ligands endow unique redox characteristics and conductivity to MOFs, while the rich and evenly dispersed Cu–O$_4$ centers help to achieve a highly selective and efficient CO$_2$RR to methane (CH$_4$) conversion process. At a low voltage of −0.9 V, Cu-DBC showed about 80% FE_{CH_4}, and the local I_d was −162.5 mA cm^{-2}, which is most efficient catalyst for CO$_2$RR to CH$_4$ (Fig. 28c, e and f). In addition, depending on the crystalline and porous structure of the catalyst, the relation between the coordination environment of the Cu single-atom center and electrochemical reduction catalytic selectivity was also studied. The specificity and detailed catalytic mechanism of the Cu-DBC catalyst for CO$_2$RR to CH$_4$ conversion was further studied through electrolysis measurement and calculation. This study offers a strategy to design CO$_2$RR catalysts with a clear structure and lays a foundation for building accurate structure–reaction correlations of efficient CO$_2$RR catalysts.
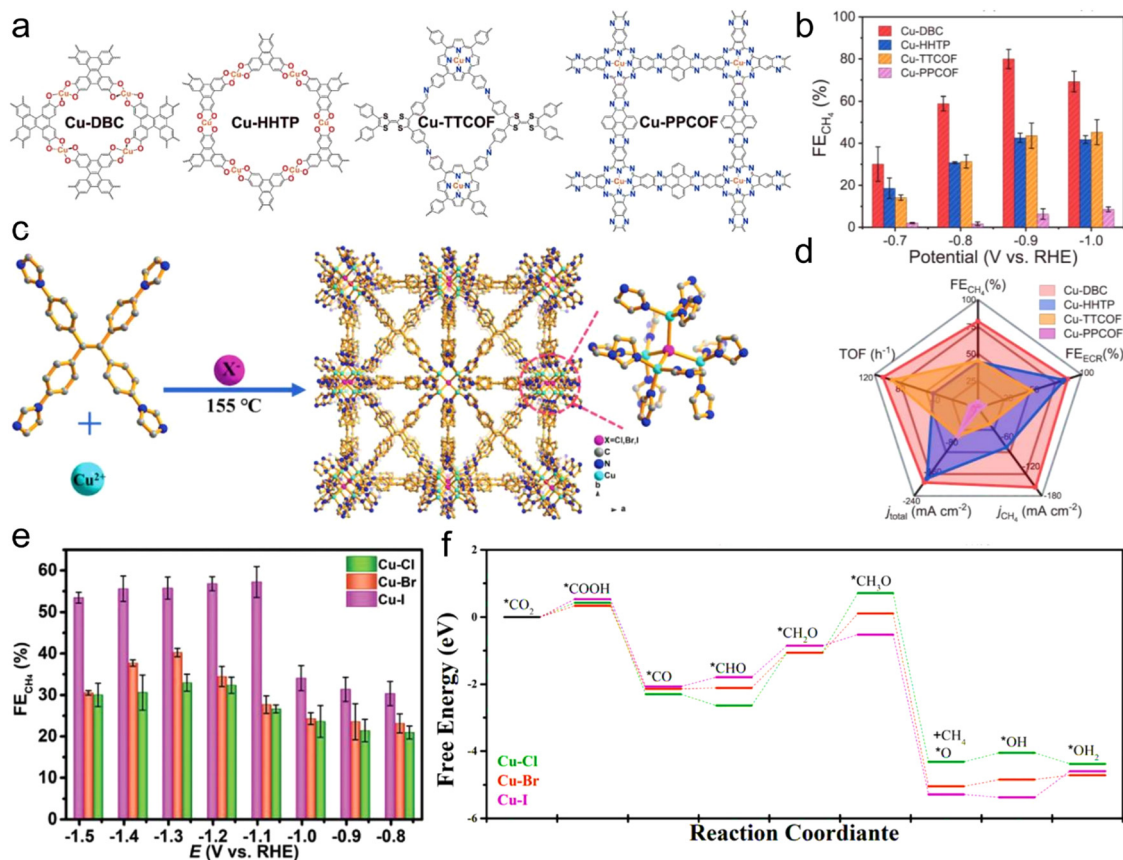
Fig. 28 (a) Formula diagrams. (b) FEs of CH_4 product. Reproduced with permission from ref. 252 Copyright 2017, Nature Springer. (c) Synthesis and crystal structure of Cu–X. Reproduced with permission from ref. 257 Copyright 2022, Wiley. (d) Inclusive electrochemical reduction performance assessment. Reproduced with permission from ref. 252 Copyright 2017, Nature Springer. (e) Average FEs of CH_4 at different potentials over different halogen-based catalysts. (f) Free energy profiles. Reproduced with permission from ref. 257 Copyright 2022, Wiley.

The relationship between the CO_2RR environment of coordination and selectivity of single-atom Cu site was studied by DFT calculations and electrocatalytic measurements. Compared with the nitrogen-coordination Cu site, the $Cu–O_4$ site in Cu-DBC with lower energy graph has good CO_2RR catalysis. Specifically, the design strategy in these studies can lay an experimental and theoretical foundation to understand the relationship among the structure of the catalyst, its microenvironment and CO_2RR performance, facilitating further research.

8.2 Bimetal mono-dispersed catalysts

8.2.1 Bimetallic centers.
Given that single-atoms have a single active site, their loading is low, and the distance between atoms is far, which is not conducive to reactions that require multi-intermediate participation. Consequently, they have no obvious advantages for chemical reactions that require multi PCET steps and involve many reaction intermediates (such as carbon dioxide reduction to C_{2+} products). Alternatively, if two same or different metal monoatom catalysts with double active sites exist, they can play a synergistic role.[258] The moderate adsorption strength of $Fe–N_4$ on *COOH leads to a very low overpotential for the CO_2RR, but *CO dissociated from *COOH is difficult to desorb.[259] Thus to break the scaling relationship

of this intermediate, Lin et al.[260] developed a synergistic catalyst composed of Fe–N site and CoPc, i.e., CoPc@Fe–N–C. It could maintain about 90% FE under a wide potential window, and its starting potential is low (−0.13 V vs. RHE). Theoretical calculation showed that CoPc promotes *CO desorption on the Fe–N–C sites and inhibits the HER and the introduction of CoPc does not affect the formation of *COOH, which is conducive to the experimental outcomes.

Tandem catalysts are a type of catalyst that exhibit unique catalytic properties by combining two materials with different catalytic functions. Because different active sites have different properties, they can achieve the goal of multi-electron (>2e) reduction products of the CO_2RR.[263,264] In SACs, the CoPc@Zn–N–C tandem catalyst could achieve much higher performance than its single components CoPc and Zn–N–C,[20] that its CH_4/CO production ratio is greater than that of the single-component catalysts. Theoretical calculation revealed that CO is first generated on CoPc, while the CoPc site also promotes *H to transfer to Zn–N–C, and CO diffuses on the Zn–N–C center and converted to CH_4. The specific DFT calculation results are shown in Fig. 29a, where *COOH is easier to form on CoPc, However, $Zn–N_4$ is more inclined to convert CO to CH_4.
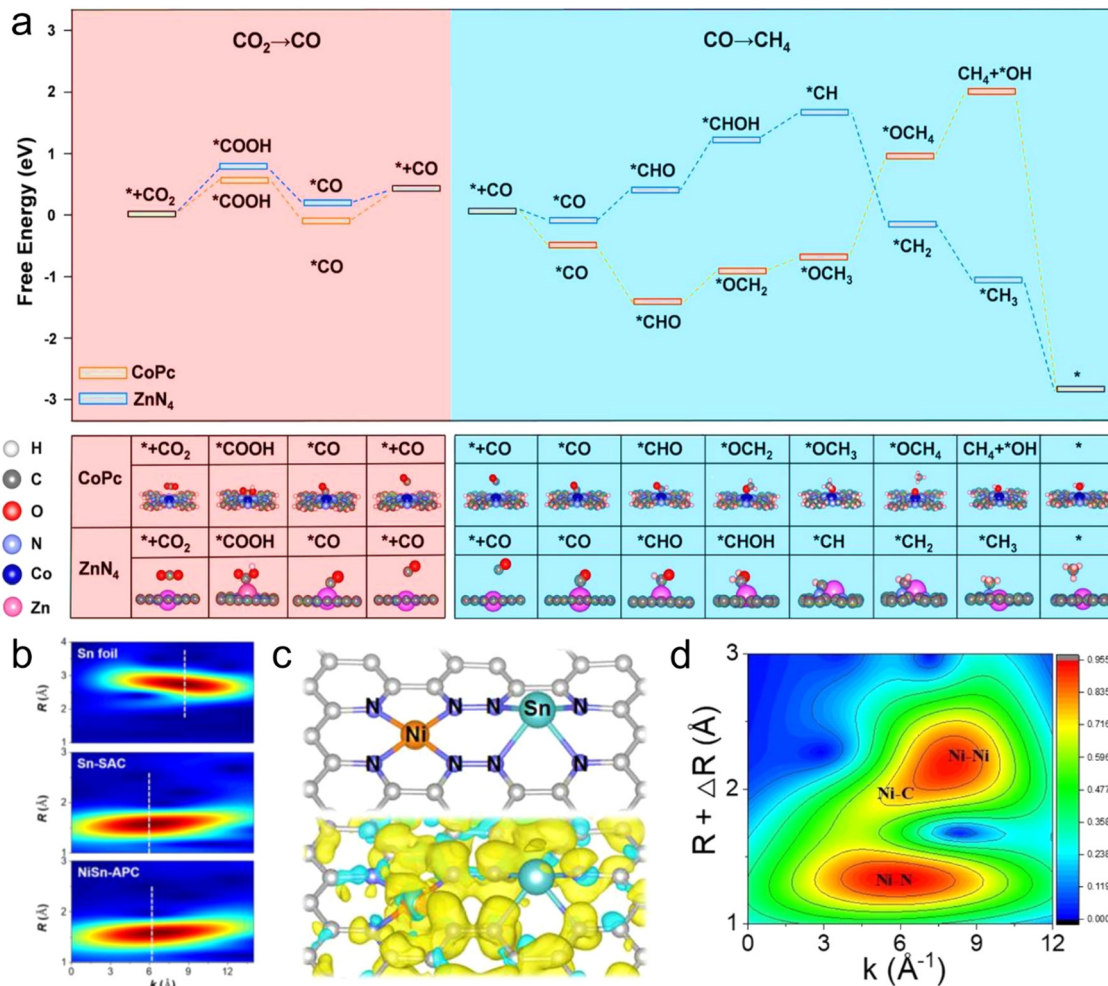
Fig. 29 (a) Free energy profiles and intermediate configuration over CoPc and ZnN₄. Reproduced with permission from ref. 20 Copyright 2020, Wiley. (b) WT analysis of NiSn-APC, Sn-SAC and Sn foil. (c) Spin electron density model proposed for NiSn-APC (yellow; spin up and green; spin down). Reproduced with permission from ref. 261 Copyright 2021, Wiley. (d) WT-EXAFS plot for Ni-CNC-1000. Reproduced with permission from ref. 262 Copyright 2022, Wiley.

8.2.2 Bimetallic sites. Bimetallic sites are usually active sites composed of bimetal atoms in the same graphite-carbon plane, which have a synergistic catalytic effect on the CO₂RR. Theoretical calculation results showed that the three combinations of Cu/Mn, Ni/Mn, and Ni/Fe may break the free energy proportional relationship of the adsorption of *COOH and *CO.[265] Relevant experimental studies further verified the correctness of the theoretical calculation results. Ni–Fe–N₆–C achieved 90% FE in the range of −0.5 to −0.9 V *vs.* RHE.[187] FE$_{CO}$ reached 98% at −0.7 V, and the selectivity of the product almost did not change after a 30 h stability test. According to the theoretical calculation results, Ni–Fe–N₆–C has a lower formation energy for *COOH and desorption energy for *CO. Among them, the combined effect between the non-bonded Ni site and the Fe site also promoted the formation of *COOH. However, the catalyst does not affect the desorption energy barrier of *CO, which also leads to its low CO current density.[266] In addition, the bonding between Ni and Fe can change the level of energy of the atomic orbital, unique

electronic structure and oxidation state of Fe, which weaken the binding energy of the reaction intermediates, thus promoting the CO₂RR performance. Under 690 mV overpotential, the catalyst had a CO partial *J* of 50.4 mA cm⁻² and FE$_{CO}$ of 94.4%.[267] In addition, theoretical calculation showed that N₄–Ni–Sn–N₄ can reduce the formation energy barrier of *OCHO, showing excellent catalytic performance. The yield of formic acid was 36.7 mol h⁻¹ g⁻¹$_{Sn}$, and the corresponding TOF as 4752 h⁻¹.[261] Its structure and charge diagram are shown in Fig. 29b and c.[261] Liang *et al.*[268] introduced a bimetallic catalyst composed of single rare-earth metal atoms, *i.e.*, La and Zn, for the first time. By adjusting the molar ratio of La and Zn, generation of CO/H₂ (syngas) with different molar ratios was realized.

Among the bimetallic catalysts, homonuclear bimetallic catalysts for the CO₂RR have also been reported by Li *et al.*,[269] where Cu monoatomic pairs were loaded on Pd₁₀Te₃ alloy. In the Cu atom pair, *i.e.*, Cu₁⁰–Cu₁ˣ⁺, Cu₁⁰ tends to adsorb CO₂ molecules, while Cu$_x$¹⁺ tends to adsorb H₂O molecules.

Together, they promoted the activation of CO_2 molecules. At about −0.78 V, the CO selectivity reached 92%. This reflects the property of "two atoms activate two molecules", which single atoms do not possess. In addition, Ding et al.[270] constructed a double Ni_1–N_4 site connected by two nitrogen atoms via the pyrolysis of a metal–organic complex occupied by adjacent Ni atoms. Theoretical calculation showed that under the condition of electrocatalysis, the two Ni_1–N_4 sites bridged by oxygen atoms significantly reduced the CO_2 activation barrier, showing high CO selectivity. Cao et al.[262] used electrospinning pyrolysis technology to prepare an Ni_2–N_4–C_2 site catalyst. The structural characterization results are shown in Fig. 29d, which confirm the results. The experimental results and DFT calculations displayed that the binuclear Ni biatomic catalyst bonded with N and C atoms adjusts the electronic characteristics of the d-band, optimizes the adsorption of CO_2 and its intermediates, enhances the charge and material transport, and promotes the reduction of CO_2.

At present, bimetallic catalysts are mainly concentrated on C_1 products, and only some tandem catalysts realize the production of multi-carbon products. Considering the advantages of bimetallic mono-dispersed atomic catalysts with different active centers, the generation of multi-carbon products is one of the main reasons for the development of bimetallic mono-dispersed atomic catalysts.

8.3 Metal carrier interactions

The electronic structure of metal atoms is regulated by covalent or ionic bond connection between the linker and metal atoms

to change the structure–activity relationship of the metal atoms.[237,271] The combination effect between the Cu single atomic site and the C site on C_3N_4 promoted the formation of C_{2+} products including C_2H_4, C_2H_6 and C_2H_5OH. The Cu single-atomic site is the active site for adsorbing *COOH, *CO and *CHO. The C site near C_3N_4 is the active site for *OCH_2 and *OCH_3.[272] The coordination among the Sn single-atomic sites, oxygen vacancies and CuO substrates enables catalyst materials to have extraordinary double layer capacitance, high CO_2 adsorption ability and low charge transfer interfacial impedance.[273] Systematic experimental findings and theoretical calculation proved that Sn_1/V_0-CuO-90 promotes the formation of *CO by reducing the energy barrier of *COOH dissociation. Then, it adsorbs on the CuO substrate and further reduces *CO to CH_3OH. HAADF-STEM and XAFS further confirmed the structure of Sn_1/V_0-CuO. Electrochemical experimental results showed that the catalyst methanol FE reached 88.6% at 67 mA cm^{-2} I_d. Its FE for ethanol and j at different potentials are shown in Fig. 30a and b, and Sn single atom and CuO rich in oxygen vacancy can synergistically promote the formation of C_2H_4. Theoretical calculation showed that Sn doping in CuO reduces the free energy of C–C coupling between the *CO intermediates, thereby promoting the formation of C_2H_4.[274]

The loading of Ir single atoms on an α-Co(OH)$_2$ substrate can effectively stabilize the adsorbed CO_2 species and promote rapid electron transport to generate CO.[275] The Sn single atom loaded on Cu nanoparticles also showed similar properties,
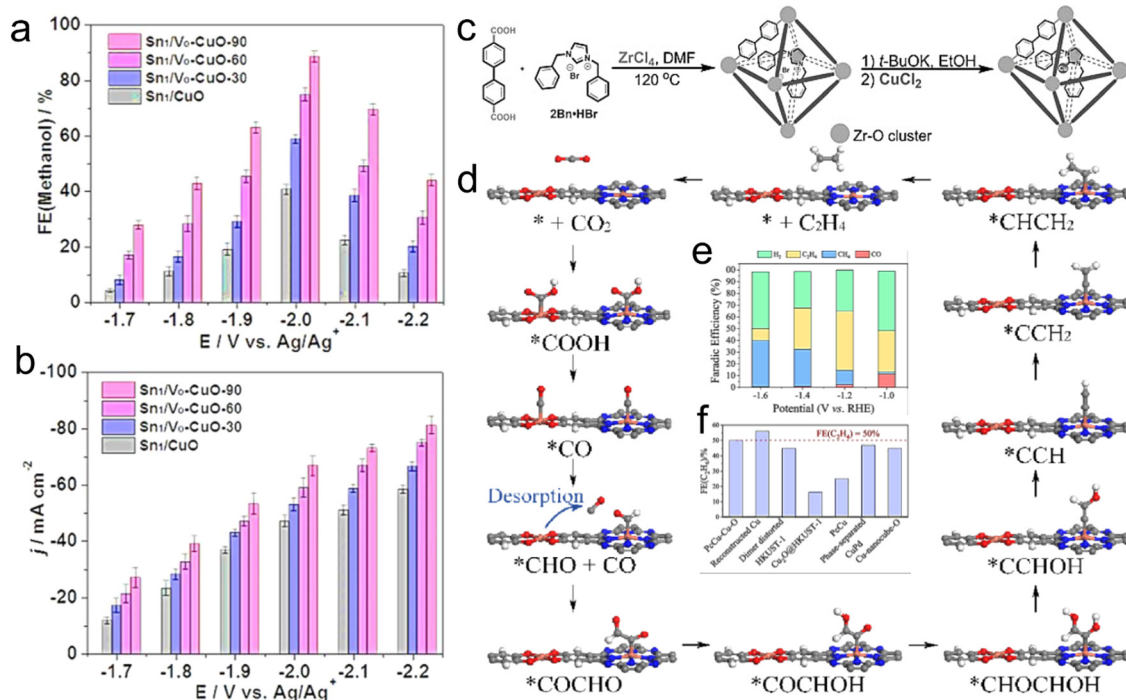
Fig. 30 (a) FE(methanol) and (b) partial current densities (j). Reproduced with permission from ref. 273 Copyright 2021, Wiley. (c) Synthesis scheme of 2Bn–Cu@UiO-67. Reproduced with permission from ref. 33 Copyright 2022, Wiley. (d) Proposed CO_2RR mechanism of PcCu–Cu–O. (e) FEs of CH_4, C_2H_4, H_2 and CO products over PcCu–Cu–O. (f) Comparison of FEs (C_2H_4) of PcCu–Cu–O and some previously reported catalysts. Reproduced with permission from ref. 278 Copyright 2021, ACS.

reaching the maximum FE_{CO} (95.3%) at -1.0 V.[276] The single-atom Pb-doped copper substrate adjusted the electronic structure of copper, and thus adjusted the first protonation process of the CO_2RR from the generation of *COOH path to generation of HCOO*. Finally, the FE of formic acid reached 96% under an industrial current density (1 A cm^{-2}). It should be pointed out that the catalytic active site is the Cu substrate rather than the Pb single atom.[277] Thus, all the above results indicate that interaction with metal support is a potential strategy to improve the catalyst performance of SACs.

8.4 Space confinement

The space-confinement strategy can promote the multi-electron reduction of CO_2 by creating a small reaction space. Recently, a catalyst containing a copper single-atomic site with nitrogen heterocyclic carbene coordination (2Bn–Cu@UiO-67, Bn is a ligand: di-benzyl imidazole) was synthesized. It achieved an unprecedented CH_3OH conversion frequency (TOF CH_3OH = 58 680 h^{-1}) and FE_{CH_4} of 81% at -1.5 V $vs.$ RHE. The J was 420 mA cm^{-2}, and it could still maintain an excellent performance in a wide potential range.[33] A schematic diagram of its synthesis is shown in Fig. 30c. Due to the electron-donating effect of the nitrogen heterocyclic carbene ligand on the Cu single-atomic site, the metal surface charge density of the Cu site increased. Therefore, the adsorption of the *CHO intermediate was greatly optimized, and *CHO is the main intermediate in the production of CH_4. Simultaneously, the pore structure of UiO@67 also has strong CO_2 capture capacity. The narrow space between the pores is conducive to the desorption of the intermediates from one 2Bn–Cu site and diffusion to another 2Bn–Cu site in the process of CO_2 reduction, realizing further the reduction of the intermediates, which is conducive to the generation of CH_4, and the interconnection reaction micro-space provided by UiO-67 in space cooperatively catalyzes the electroreduction of CO_2. This work shows that the space-limited strategy has broad prospects.

8.5 Molecular bridging

Covalent organic frameworks (COFs) can separate single metal sites, which is one of the ideal models for building monodispersed metal SACs. This avoids the high-temperature pyrolysis required by traditional methods and can achieve the dispersion of single-atomic sites at a relatively mild temperature. For example, the common way is to directly use four nitrogen atoms on phthalocyanine ligands to coordinate with metal ions. The metal phthalocyanine structural unit is constructed, and then the connection between the structural units is realized through covalent organic chemical reaction to obtain a metal covalent organic network structure with super conjugated system. The COF_{bpy} catalyst (COF_{bpyMn}) anchored at the Mn unit point has a clear and recognizable coordination center, and the reduction of CO_2 in water had a low overpotential (190 mV), and the current density reached 12 mA cm^{-2} at 550 mV overpotential. The TOF_{CO} and TON_{CO} (turnover number) were 1100 and 5800 h^{-1} (after 16 h), respectively, almost 10 times that of the equivalent Mn-based molecular catalyst.[279]

Lu et al.[280] realized the construction of a series of single-atomic site catalysts by connecting metal phthalocyanines with dioxins. NiPcTFPN and CoPcTFPN achieved (99.8 ± 1.24)% and (96.1 ± 1.25)% FE_{CO}, respectively. In addition, the catalyst containing Cu–N$_4$ and Cu–O$_4$ sites (PcCu–Cu–O) constructed by COFs also achieved high selectivity from CO_2 to multi-carbon products. In 0.1 mol L^{-1} KHCO$_3$ solution, the ethylene selectivity reached 50% under the test conditions of -1.2 V ($vs.$ RHE). The in $situ$ infrared spectroscopy experiment also further verified the combination effect between the Cu–N$_4$ site and Cu–O$_4$ site in CuPc,[278] as shown in Fig. 30d–f. CO desorbed from the Cu–O$_4$ site can undergo C–C coupling reaction with *CO adsorbed by Cu–N$_4$. MOF materials constructed of metal phthalocyanine also show superior performance. 2D metal phthalocyanine-based MOF nanosheets (NiPc–NiO$_4$) overcome the shortcomings of poor conductivity of traditional MOFs,[59] showing 98.4% CO selectivity and J_{CO} as high as 34.5 mA cm^{-2}. The COF composed of metalloporphyrins realized the formation of multi-electron reduction products. In addition, the ultra-thin Cu-Tph COF-Dct (about 3.8 nm) showed an FE_{CH_4} of about 80%, and the flow cell exhibited the performance of -220.0 mA cm^{-2} current density at -0.9 V.[281] This is almost twice that of the unexposed COF. DFT calculation revealed that the improved performance is ascribed to the fixation on the COF, and the integration of amino and triazine groups in the functionalized stripping reagent enhances the activation and adsorption of CO_2, stabilizes the reaction intermediates and increases the CO concentration near the Cu site. For the metal porphyrin MOF material, the multilayer 2D porphyrin MOF was prepared into a single layer, which is also conducive to the generation of C$_2$ products.[282] This is because the monolayer porphyrin-based MOF has a reconstructed Cu–O$_4$ site, while the main products with more than two layers are mainly CO and HCOO$^-$. However, when only a certain potential is applied, only 11.9% FE_{C_2} was achieved. However, upon exposure to light, the FE of C$_2$ increased to 41.1%.

9. Summary and perspectives

According to this review, the design of MOF-based catalytic materials is mainly carried out depending on several important physical and chemical properties, including the metal-center characteristics, ligand and coordination environment, and the morphology and particle size of materials. In different types of materials, the research focus on these properties will be slightly different. The metal centers of active MOFs mostly exist in the form of atoms or clusters, with excellent dispersion. Currently, different types of metals and their different coordination environments tend to exhibit completely different bonding capabilities, resulting in different affinities with CO_2 or differences in the types and quantities of active-free radicals, which ultimately affect the selectivity and activity of the CO_2RR. For the composite catalysts of MOF and metal, the dispersion degree, morphology, particle size, defect state of the supported metal particles and the contact between the two materials

usually affect the transfer of electrons and reactant CO_2 between the two phases, thus becoming the focus of composite catalyst design. Similarly, the research on MOF derivatives attaches great importance to the characteristics of their metal centers, such as whether they can maintain or introduce metal centers in monatomic state, the types of metal non-metal bonds generated and their catalytic activities.

The design of ligand types and coordination environment is mainly to increase the activation and adsorption of CO_2 by utilizing the synergistic effect between specific functional groups of ligand molecules and metals. In addition, the design of ligands has different aims in photo- and electro-catalytic reduction. In photocatalysis, ligands can adjust the energy band structure to enhance the utilization of visible light. In electrocatalysis, ligands can communicate charge transport pathways and increase the working efficiency of the active centers by virtue of their electron-donating ability or the intrinsic catalytic activity of molecules. Finally, the control of the morphology and particle size of materials aims to greatly optimize their size in one or several dimensions to obtain structures such as ultra-small nanoparticles, two-dimensional layered materials, and dendritic crystals. These special morphologies can usually reveal more active centers and shorten the transfer path of electrons, thus showing higher catalytic performance. In addition to the common focus presented above, in electrocatalysis systems, the electrode preparation process needs to be optimized to promote the interaction between the catalytic material and electrolyte, improve the density and openness of the active catalytic sites, and achieve more efficient charge transfer. An ideal electrocatalyst needs to produce a high J at a low overpotential, which requires higher conductivity, active site density and CO_2 affinity in the material.

Catalytic materials based on MOFs have witnessed significant development in the field of catalytic CO_2RR, which will receive even more attention. However, the promotion and application of these materials still face many challenges. Firstly, their catalytic yield is too low, but the energy level required to be input is high, which does not have practical application value. Simultaneously, the cost of the preparation of MOF materials is usually high and their stability is not very prominent. Therefore, it is a future vision to solve the actual carbon emission problem through photo- and electro-catalytic CO_2 reduction. It can be seen from the development history of zeolite molecular sieves, which are porous materials, that after the catalytic performance of the material has made a substantial breakthrough, its preparation cost and service life are expected to make considerable progress with the development of large-scale production. Therefore, at present, the urgent problem to be solved for MOF-based catalysts is how to obtain the reaction conversion rate with commercial value through a simple, green and practical process. The pursuit of catalytic performance leads to another big problem, that is, the research on the reaction mechanism of MOF materials for photo- and electro-reduction of CO_2 is not deep enough and research in this area generally focuses on the analysis of several common physical and chemical properties of materials by trial and error,

instead of forming a system, thus failing to fully utilize the various excellent properties of MOFs and other materials and far from reaching the level of designing high-performance catalysts according to demand. This is mainly because of the complexity of MOF materials, where it is difficult to carry out systematic and comprehensive theoretical calculations and pre-design for multiple influencing factors such as the bonding ability of their active site, the degree of spatial structure openness, charge-carrier transfer efficiency, and the diffusion efficiency of reactants and products.

Also, these complex factors are more difficult to track and grasp after the MOF is compounded or derived. This leads to the fact that most of the current theoretical calculations are supplementary explanations of experimental phenomena, and there are few pre-designed reports based on advanced computing theories. With the rapid development of research and the continuous promotion of the macro policy of carbon neutrality, the research on MOF-based CO_2RR catalysts in the future will gradually emphasize the greening and practicality of materials, strengthen the optimization of catalyst preparation technology and the in-depth exploration of the reaction mechanism, and the involvement of advanced computing and the exploration of catalyst design theory will also be more common. With the continuous improvement of catalytic performance, the diversification and selectivity of reduction products will also be gradually emphasized. In improving the catalytic performance, as the key issue, the current hot strategies, such as preparation of single atomic or ultra-small particle size catalysts, design of advantageous coordination environment, development of ultra-thin 2D MOFs, fabrication of efficient heterostructures, application of conductive MOFs, and *in situ* electrosynthesis, are expected to achieve a significant increase in conversion. At present, the main product of SACs (including bimetallic SCAs) is CO, and the selectivity and current density of CO can maintain a high level in a wide potential window. However, how to improve the performance of the catalyst to next level so that it can operate stably for a long time under industrial conditions is still a problem to be solved at present. In addition, for the generation of multi-electron ($>2e$) reduction products and C_{2+} products, SACs with a single active component are difficult to achieve. This is because the metal loading of single-atom catalysts is generally low ($<5\%$), and the distance between active sites is far, CO generated after CO_2 reduction is difficult to diffuse from the active site to another single atomic site after desorption, and the possibility of carbon–carbon coupling is low, leading to C_1 products dominated by CO, HCOOH and CH_4. Accordingly, introducing single metal atoms in tandem catalysts or multi-component multi-site catalysts is one of the strategies that is expected to generate multi-electron products and C_{2+} products. Additionally there are many challenges faced by SACs to be solved, as follows: (1) exploring ways to replace the traditional competing heterogeneous reactions. (2) Improving the stability of SACs, particularly with a high metal loading or at high temperature or high voltage, to fulfil the industrial requirements. (3) Solving the issues of catalyst carbon deposition and poisoning of the metal

active center in heterogeneous catalysis. (4) Screening monatomic catalytic system suitable for industrial application and developing production technology with large-scale application prospect. (5) Developing monatomic catalysis to accelerate its application at the industrial level and promote its wide application in various research fields as soon as possible. Furthermore, controlling the local microenvironment of single metal atoms systematically and accurately through experimental means remains to be further explored. In addition, the in-depth study of the mechanism of the CO_2RR on SACs is also extremely challenging. Clarifying the reaction mechanism can design the configuration of SACs in a targeted way to achieve higher catalytic activity and selectivity. In the future, we can expect to deeply explore the mechanism and path of the CO_2RR with the help of clearly defined catalytic active sites of SACs, combined with quasi *in situ* and *ex situ* characterization methods, and conduct auxiliary guidance and verification through theoretical calculation simulation, thus exploiting the organic unity of material structure, catalytic activity and reaction mechanism. Finally, this should be based on a deep understanding of the reaction system to efficiently use the characteristics of the MOF metal active centers, ligands and crystal morphology and structure and through the rational design of molecular scale to build a more efficient new generation of catalytic materials.

Conflicts of interest

The authors declare no competing financial interest.

Acknowledgements

References

1 S. Abernethy and R. B. Jackson, *Environ. Res. Lett.*, 2022, **17**, 024019.

2 W. Li, D. Wang, Y. Zhang, L. Tao, T. Wang, Y. Zou, Y. Wang, R. Chen and S. Wang, *Adv. Mater.*, 2020, **32**, 1907879.

3 T. Zhan, Y. Zou, Y. Yang, X. Ma, Z. Zhang and S. Xiang, *ChemCatChem*, 2022, **14**, e202101453.

4 L. Tang, X. Meng, D. Deng and X. Bao, *Adv. Mater.*, 2019, **31**, 1901996.

5 S. Jamil, M. Fasehullah, B. Jabar, P. Liu, M. K. Aslam, Y. Zhang, S. Bao and M. Xu, *Nano Energy*, 2022, **94**, 106961.

6 M. K. Aslam, T. Hussain, H. Tabassum, Z. Wei, W. Tang, S. Li, S.-J. Bao, X. S. Zhao and M. Xu, *Chem. Eng. J.*, 2022, **429**, 132389.

7 N. Farooq, A. u Rehman, A. M. Qureshi, Z. u Rehman, A. Ahmad, M. K. Aslam, H. M. A. Javed, S. Hussain, M. A. Habila, N. AlMasoud and T. S. Alomar, *Surf. Interfaces*, 2021, **26**, 101399.

8 Y. Sun, S. Ding, S. Xu, J. Duan and S. Chen, *J. Power Sources*, 2021, **494**, 229733.

9 Y. Sun, T. Jiang, J. Duan, L. Jiang, X. Hu, H. Zhao, J. Zhu, S. Chen and X. Wang, *ACS Catal.*, 2020, **10**, 11371–11379.

10 J. Duan, Y. Sun, S. Chen, X. Chen and C. Zhao, *J. Mater. Chem. A*, 2020, **8**, 18810–18815.

11 D. Banham, T. Kishimoto, Y. Zhou, T. Sato, K. Bai, J.-I. Ozaki, Y. Imashiro and S. Ye, *Sci. Adv.*, 2018, **4**, eaar7180.

12 H. Gharibi, N. Dalir, M. Jafari, M. J. Parnian and M. Zhiani, *Appl. Surf. Sci.*, 2022, **572**, 151367.

13 H. Wang, W. Wang, H. Yu, Q. Mao, Y. Xu, X. Li, Z. Wang and L. Wang, *Appl. Catal., B*, 2022, **307**, 121172.

14 S. G. Han, M. Zhang, Z. H. Fu, L. Zheng, D. D. Ma, X. T. Wu and Q. L. Zhu, *Adv. Mater.*, 2022, **34**, 2202830.

15 Q. Jiang, Z. Chen, J. Tong, M. Yang, Z. Jiang and C. Li, *Chem. Commun.*, 2017, **53**, 1188–1191.

16 Q. Jiang, J. Tong, G. Zhou, Z. Jiang, Z. Li and C. Li, *Sol. Energy*, 2014, **103**, 425–437.

17 A. Demont and S. Abanades, *RSC Adv.*, 2014, **4**, 54885–54891.

18 S. Dey, B. Naidu and C. Rao, *Chem. – Eur. J.*, 2015, **21**, 7077–7081.

19 M. Jouny, W. Luc and F. Jiao, *Ind. Eng. Chem. Res.*, 2018, **57**, 2165–2177.

20 L. Lin, T. Liu, J. Xiao, H. Li, P. Wei, D. Gao, B. Nan, R. Si, G. Wang and X. Bao, *Angew. Chem., Int. Ed.*, 2020, **59**, 22408–22413.

21 X. Li, S. You, J. Du, Y. Dai, H. Chen, Z. Cai, N. Ren and J. Zou, *J. Mater. Chem. A*, 2019, 7, 25853–25864.

22 S. S. A. Shah, T. Najam, M. Wen, S.-Q. Zang, A. Waseem and H.-L. Jiang, *Small Structures*, 2022, **3**, 2100090.

23 Z. Song, L. Zhang, K. Doyle-Davis, X. Fu, J. L. Luo and X. Sun, *Adv. Energy Mater.*, 2020, **10**, 2001561.

24 K. Srinivas, Y. Lu, Y. Chen, W. Zhang and D. Yang, *ACS Sustainable Chem. Eng.*, 2020, **8**, 3820–3831.

25 X. Ma, F. Sun, L. Qin, Y. Liu, X. Kang, L. Wang, D.-E. Jiang, Q. Tang and Z. Tang, *Chem. Sci.*, 2022, **13**, 10149–10158.

26 Y. Xu, C. Li, Y. Xiao, C. Wu, Y. Li, Y. Li, J. Han, Q. Liu and J. He, *ACS Appl. Mater. Interfaces*, 2022, **14**, 11567–11574.

27 Y. Zou, T. Zhan, Y. Yang, Z. Fan, Y. Li, Y. Zhang, X. Ma, Q. Chen, S. Xiang and Z. Zhang, *J. Mater. Chem. A*, 2022, **10**, 3216–3225.

28 S. Li, A. V. Nagarajan, X. Du, Y. Li, Z. Liu, D. R. Kauffman, G. Mpourmpakis and R. Jin, *Angew. Chem., Int. Ed.*, 2022, e202211771.

29 X. Zhou, E. Song, Z. Kuang, Z. Gao, H. Zhao, J. Liu, S. Sun, C.-Y. Mou and H. Chen, *Chem. Eng. J.*, 2022, **430**, 133035.

30 T. Tsujiguchi, Y. Kawabe, S. Jeong, T. Ohto, S. Kukunuri, H. Kuramochi, Y. Takahashi, T. Nishiuchi, H. Masuda, M. Wakisaka, K. Hu, G. Elumalai, J.-I. Fujita and Y. Ito, *ACS Catal.*, 2021, **11**, 3310–3318.

31 T. Tang, W.-J. Jiang, X.-Z. Liu, J. Deng, S. Niu, B. Wang, S.-F. Jin, Q. Zhang, L. Gu and J.-S. Hu, *J. Am. Chem. Soc.*, 2020, **142**, 7116–7127.

32 C. He, Y. Zhang, Y. Zhang, L. Zhao, L. P. Yuan, J. Zhang, J. Ma and J. S. Hu, *Angew. Chem., Int. Ed.*, 2020, **132**, 4944–4949.

33 S. Chen, W.-H. Li, W. Jiang, J. Yang, J. Zhu, L. Wang, H. Ou, Z. Zhuang, M. Chen, X. Sun, D. Wang and Y. Li, *Angew. Chem., Int. Ed.*, 2022, **61**, e202114450.

34 J. Zhang, W. J. Jiang, S. Niu, H. Zhang, J. Liu, H. Li, G. F. Huang, L. Jiang, W. Q. Huang and J. S. Hu, *Adv. Mater.*, 2020, **32**, 1906015.

35 E. Vijayakumar, S. Ramakrishnan, C. Sathiskumar, D. J. Yoo, J. Balamurugan, H. S. Noh, D. Kwon, Y. H. Kim and H. Lee, *Chem. Eng. J.*, 2022, **428**, 131115.

36 Y. Zhou, R. Abazari, J. Chen, M. Tahir, A. Kumar, R. R. Ikreedeegh, E. Rani, H. Singh and A. M. Kirillov, *Coord. Chem. Rev.*, 2022, **451**, 214264.

37 J. Gascon, A. Corma, F. Kapteijn and F. X. Llabres i Xamena, *ACS Catal.*, 2014, **4**, 361–378.

38 L. B. Vilhelmsen, K. S. Walton and D. S. Sholl, *J. Am. Chem. Soc.*, 2012, **134**, 12807–12816.

39 Y. Ma, H. Peng, J. Liu, Y. Wang, X. Hao, X. Feng, S. U. Khan, H. Tan and Y. Li, *Inorg. Chem.*, 2018, **57**, 4109–4116.

40 J. Jiang and O. M. Yaghi, *Chem. Rev.*, 2015, **115**, 6966–6997.

41 H. Kobayashi, Y. Mitsuka and H. Kitagawa, *Inorg. Chem.*, 2016, **55**, 7301–7310.

42 Q. Yang, Q. Xu and H.-L. Jiang, *Chem. Soc. Rev.*, 2017, **46**, 4774–4808.

43 B. D. McCarthy, A. M. Beiler, B. A. Johnson, T. Liseev, A. T. Castner and S. Ott, *Coord. Chem. Rev.*, 2020, **406**, 213137.

44 J. Wen, Y. Li and J. Gao, *Chem. Res. Chin. Univ.*, 2020, **36**, 662–679.

45 X. Liu, G. Verma, Z. Chen, B. Hu, Q. Huang, H. Yang, S. Ma and X. Wang, *The Innovation*, 2022, **3**, 100281.

46 J. Lei, M. Zeng and L. Fu, *Chem. Res. Chin. Univ.*, 2020, **36**, 504–510.

47 X. Han, X. Ling, Y. Wang, T. Ma, C. Zhong, W. Hu and Y. Deng, *Angew. Chem., Int. Ed.*, 2019, **58**, 5359–5364.

48 Y. He, Q. Shi, W. Shan, X. Li, A. J. Kropf, E. C. Wegener, J. Wright, S. Karakalos, D. Su and D. A. Cullen, *Angew. Chem., Int. Ed.*, 2021, **60**, 9516–9526.

49 S. Fang, X. Zhu, X. Liu, J. Gu, W. Liu, D. Wang, W. Zhang, Y. Lin, J. Lu and S. Wei, *Nat. Commun.*, 2020, **11**, 1–8.

50 Y. Wang, Y. Pan, L. Zhu, H. Yu, B. Duan, R. Wang, Z. Zhang and S. Qiu, *Carbon*, 2019, **146**, 671–679.

51 M. K. Aslam, S. S. A. Shah, S. Li and C. Chen, *J. Mater. Chem. A*, 2018, **6**, 14083–14090.

52 J. Wang, Z. Huang, W. Liu, C. Chang, H. Tang, Z. Li, W. Chen, C. Jia, T. Yao and S. Wei, *J. Am. Chem. Soc.*, 2017, **139**, 17281–17284.

53 Y. Chen, S. Ji, Y. Wang, J. Dong, W. Chen, Z. Li, R. Shen, L. Zheng, Z. Zhuang and D. Wang, *Angew. Chem., Int. Ed.*, 2017, **129**, 7041–7045.

54 J. Li, M. Chen, D. A. Cullen, S. Hwang, M. Wang, B. Li, K. Liu, S. Karakalos, M. Lucero and H. Zhang, *Nat. Catal.*, 2018, **1**, 935–945.

55 S. Ji, Y. Chen, X. Wang, Z. Zhang, D. Wang and Y. Li, *Chem. Rev.*, 2020, **120**, 11900–11955.

56 J. Liu, D. Yang, Y. Zhou, G. Zhang, G. Xing, Y. Liu, Y. Ma, O. Terasaki, S. Yang and L. Chen, *Angew. Chem., Int. Ed.*, 2021, **60**, 14473–14479.

57 X.-J. Kong, T. He, J. Zhou, C. Zhao, T.-C. Li, X.-Q. Wu, K. Wang and J.-R. Li, *Small*, 2021, **17**, 2005357.

58 L. Qin, Z. Xu, Y. Zheng, C. Li, J. Mao and G. Zhang, *Adv. Funct. Mater.*, 2020, **30**, 1910257.

59 J. D. Yi, D. H. Si, R. Xie, Q. Yin, M. D. Zhang, Q. Wu, G. L. Chai, Y. B. Huang and R. Cao, *Angew. Chem., Int. Ed.*, 2021, **133**, 17245–17251.

60 Q. Dang, H. Huang, L. Li, X. Lyu, S. Zhong, Y. Yu and D. Xu, *Chem. Mater.*, 2021, **33**, 5690–5699.

61 W. Kai, X. Li, C. Hengze, Q. Huiying, C. Chao and Z. Ning, *Chem. J. Chin. Univ.*, 2016, **37**, 723–727.

62 C. Park, W. T. Koo, S. Chong, H. Shin, Y. H. Kim, H. J. Cho, J. S. Jang, D. H. Kim, J. Lee and S. Park, *Adv. Mater.*, 2021, **33**, 2101216.

63 M. Usman, M. Ali, B. A. Al-Maythalony, A. S. Ghanem, O. W. Saadi, M. Ali, M. A. Jafar Mazumder, S. Abdel-Azeim, M. A. Habib and Z. H. Yamani, *ACS Appl. Mater. Interfaces*, 2020, **12**, 49992–50001.

64 Y. Liu, D. Deng and X. Bao, *Chem*, 2020, **6**, 2497–2514.

65 Y. Y. Birdja, E. Pérez-Gallent, M. C. Figueiredo, A. J. Göttle, F. Calle-Vallejo and M. T. M. Koper, *Nat. Energy*, 2019, **4**, 732–745.

66 Z. Tao and H. Wang, *Chem. Res. Chin. Univ.*, 2020, **36**, 1145–1146.

67 X. Fu, A. Zhu, X. Chen, S. Zhang, M. Wang and M. Yuan, *Chem. Res. Chin. Univ.*, 2021, **37**, 1328–1333.

68 H. Wang, X. Wu, G. Liu, S. Wu and R. Xu, *Nano Res.*, 2022, DOI: **10.1007/s12274-022-4199-4**.

69 J. Xiangyuan, Z. Libing, S. Xiaofu, B. Han, L. Zhang, X. Jin and X. Sun, *Chem. J. Chin. Univ.*, 2022, **43**, 20220035.

70 A. Wagner, C. D. Sahm and E. Reisner, *Nat. Catal.*, 2020, **3**, 775–786.

71 Y. Wang, P. Han, X. Lv, L. Zhang and G. Zheng, *Joule*, 2018, **2**, 2551–2582.

72 J.-M. Savéant, *Chem. Rev.*, 2008, **108**, 2348–2378.

73 R. Kortlever, J. Shen, K. J. P. Schouten, F. Calle-Vallejo and M. T. M. Koper, *J. Phys. Chem. Lett.*, 2015, **6**, 4073–4082.

74 H. A. Hansen, J. B. Varley, A. A. Peterson and J. K. Nørskov, *J. Phys. Chem. Lett.*, 2013, **4**, 388–392.

75 J. T. Feaster, C. Shi, E. R. Cave, T. Hatsukade, D. N. Abram, K. P. Kuhl, C. Hahn, J. K. Nørskov and T. F. Jaramillo, *ACS Catal.*, 2017, **7**, 4822–4827.

76 W. Ni, Y. Xue, X. Zang, C. Li, H. Wang, Z. Yang and Y.-M. Yan, *ACS Nano*, 2020, **14**, 2014–2023.

77 S. Zhang, P. Kang and T. J. Meyer, *J. Am. Chem. Soc.*, 2014, **136**, 1734–1737.

78 A. S. Varela, W. Ju, A. Bagger, P. Franco, J. Rossmeisl and P. Strasser, *ACS Catal.*, 2019, **9**, 7270–7284.

79 J. Li, P. Yan, K. Li, J. You, H. Wang, W. Cui, W. Cen, Y. Chu and F. Dong, *J. Mater. Chem. A*, 2019, **7**, 17014–17021.

80 X. Nie, M. R. Esopi, M. J. Janik and A. Asthagiri, *Angew. Chem., Int. Ed.*, 2013, **52**, 2459–2462.

81 H. Zhang, X. Chang, J. G. Chen, W. A. Goddard, B. Xu, M.-J. Cheng and Q. Lu, *Nat. Commun.*, 2019, **10**, 3340.

82 Y. Zheng, A. Vasileff, X. Zhou, Y. Jiao, M. Jaroniec and S.-Z. Qiao, *J. Am. Chem. Soc.*, 2019, **141**, 7646–7659.

83 L. Fan, C. Xia, F. Yang, J. Wang, H. Wang and Y. Lu, *Sci. Adv.*, 2020, **6**, eaay3111.

84 I. Ledezma-Yanez, E. P. Gallent, M. T. M. Koper and F. Calle-Vallejo, *Catal. Today*, 2016, **262**, 90–94.

85 L. Wang, S. Nitopi, A. B. Wong, J. L. Snider, A. C. Nielander, C. G. Morales-Guio, M. Orazov, D. C. Higgins, C. Hahn and T. F. Jaramillo, *Nat. Catal.*, 2019, **2**, 702–708.

86 Y. Momose, K. Sato and O. Ohno, *Surf. Interface Anal.*, 2002, **34**, 615–618.

87 X. Zhi, Y. Jiao, Y. Zheng, A. Vasileff and S.-Z. Qiao, *Nano Energy*, 2020, **71**, 104601.

88 M. A. Tekalgne, H. H. Do, A. Hasani, Q. Van Le, H. W. Jang, S. H. Ahn and S. Y. Kim, *Mater. Today Adv.*, 2020, **5**, 100038.

89 X. Su, Y. Sun, L. Jin, L. Zhang, Y. Yang, P. Kerns, B. Liu, S. Li and J. He, *Appl. Catal., B*, 2020, **269**, 118800.

90 F. Zhang and A. C. Co, *Angew. Chem., Int. Ed.*, 2020, **59**, 1674–1681.

91 Y. Feng, W. An, Z. Wang, Y. Wang, Y. Men and Y. Du, *ACS Sustainable Chem. Eng.*, 2020, **8**, 210–222.

92 Y. Hori, H. Wakebe, T. Tsukamoto and O. Koga, *Electrochim. Acta*, 1994, **39**, 1833–1839.

93 W. Ma, S. Xie, T. Liu, Q. Fan, J. Ye, F. Sun, Z. Jiang, Q. Zhang, J. Cheng and Y. Wang, *Nat. Catal.*, 2020, **3**, 478–487.

94 Q. Hu, Z. Han, X. Wang, G. Li, Z. Wang, X. Huang, H. Yang, X. Ren, Q. Zhang, J. Liu and C. He, *Angew. Chem., Int. Ed.*, 2020, **59**, 19054–19059.

95 D. H. Won, H. Shin, J. Koh, J. Chung, H. S. Lee, H. Kim and S. I. Woo, *Angew. Chem., Int. Ed.*, 2016, **55**, 9297–9300.

96 H. S. Jeon, I. Sinev, F. Scholten, N. J. Divins, I. Zegkinoglou, L. Pielsticker and B. R. Cuenya, *J. Am. Chem. Soc.*, 2018, **140**, 9383–9386.

97 D. Ren, B. S.-H. Ang and B. S. Yeo, *ACS Catal.*, 2016, **6**, 8239–8247.

98 G. Keerthiga and R. Chetty, *J. Electrochem. Soc.*, 2017, **164**, H164–H169.

99 J. Albo, A. Sáez, J. Solla-Gullón, V. Montiel and A. Irabien, *Appl. Catal., B*, 2015, **176–177**, 709–717.

100 S. Sarfraz, A. T. Garcia-Esparza, A. Jedidi, L. Cavallo and K. Takanabe, *ACS Catal.*, 2016, **6**, 2842–2851.

101 M. Morimoto, Y. Takatsuji, R. Yamasaki, H. Hashimoto, I. Nakata, T. Sakakura and T. Haruyama, *Electrocatalysis*, 2018, **9**, 323–332.

102 K. D. Yang, W. R. Ko, J. H. Lee, S. J. Kim, H. Lee, M. H. Lee and K. T. Nam, *Angew. Chem., Int. Ed.*, 2017, **56**, 796–800.

103 F. Li, L. Chen, G. P. Knowles, D. R. MacFarlane and J. Zhang, *Angew. Chem., Int. Ed.*, 2017, **56**, 505–509.

104 H. Song, M. Im, J. T. Song, J.-A. Lim, B.-S. Kim, Y. Kwon, S. Ryu and J. Oh, *Appl. Catal., B*, 2018, **232**, 391–396.

105 A. Dutta, M. Rahaman, N. C. Luedi, M. Mohos and P. Broekmann, *ACS Catal.*, 2016, **6**, 3804–3814.

106 A. S. Hall, Y. Yoon, A. Wuttig and Y. Surendranath, *J. Am. Chem. Soc.*, 2015, **137**, 14834–14837.

107 Z. Pan, K. Wang, K. Ye, Y. Wang, H.-Y. Su, B. Hu, J. Xiao, T. Yu, Y. Wang and S. Song, *ACS Catal.*, 2020, **10**, 3871–3880.

108 J.-J. Lv, M. Jouny, W. Luc, W. Zhu, J.-J. Zhu and F. Jiao, *Adv. Mater.*, 2018, **30**, 1803111.

109 M. Ma, K. Djanashvili and W. A. Smith, *Angew. Chem., Int. Ed.*, 2016, **55**, 6680–6684.

110 F. Li, G. H. Gu, C. Choi, P. Kolla, S. Hong, T.-S. Wu, Y.-L. Soo, J. Masa, S. Mukerjee, Y. Jung, J. Qiu and Z. Sun, *Appl. Catal., B*, 2020, **277**, 119241.

111 P. Gotico, Z. Halime and A. Aukauloo, *Dalton Trans.*, 2020, **49**, 2381–2396.

112 W. Zhang, Y. Hu, L. Ma, G. Zhu, Y. Wang, X. Xue, R. Chen, S. Yang and Z. Jin, *Adv. Sci.*, 2018, **5**, 1700275.

113 A. Liu, M. Gao, X. Ren, F. Meng, Y. Yang, L. Gao, Q. Yang and T. Ma, *J. Mater. Chem. A*, 2020, **8**, 3541–3562.

114 H. Cui, Y. Guo, L. Guo, L. Wang, Z. Zhou and Z. Peng, *J. Mater. Chem. A*, 2018, **6**, 18782–18793.

115 F. Calle-Vallejo and M. T. Koper, *Angew. Chem., Int. Ed.*, 2013, **125**, 7423–7426.

116 Q. Zhu, D. Yang, H. Liu, X. Sun, C. Chen, J. Bi, J. Liu, H. Wu and B. Han, *Angew. Chem., Int. Ed.*, 2020, **132**, 8981–8986.

117 X. Kang, L. Li, A. Sheveleva, X. Han, J. Li, L. Liu, F. Tuna, E. J. McInnes, B. Han and S. Yang, *Nat. Commun.*, 2020, **11**, 1–9.

118 X. Kang, B. Wang, K. Hu, K. Lyu, X. Han, B. F. Spencer, M. D. Frogley, F. Tuna, E. J. McInnes and R. A. Dryfe, *J. Am. Chem. Soc.*, 2020, **142**, 17384–17392.

119 S. Dou, J. J. Song, S. B. Xi, Y. H. Du, J. Wang, Z. F. Huang, Z. C. J. Xu and X. Wang, *Angew. Chem., Int. Ed.*, 2019, **58**, 4041–4045.

120 C.-J. Chang, S.-F. Hung, C.-S. Hsu, H.-C. Chen, S.-C. Lin, Y.-F. Liao and H. M. Chen, *ACS Cent. Sci.*, 2019, **5**, 1998–2009.

121 P. De Luna, R. Quintero-Bermudez, C.-T. Dinh, M. B. Ross, O. S. Bushuyev, P. Todorović, T. Regier, S. O. Kelley, P. Yang and E. H. Sargent, *Nat. Catal.*, 2018, **1**, 103–110.

122 L. Majidi, A. Ahmadiparidari, N. Shan, S. N. Misal, K. Kumar, Z. Huang, S. Rastegar, Z. Hemmat, X. Zou and P. Zapol, *Adv. Mater.*, 2021, **33**, 2004393.

123 I. Hod, M. D. Sampson, P. Deria, C. P. Kubiak, O. K. Farha and J. T. Hupp, *ACS Catal.*, 2015, **5**, 6302–6309.

124 X. Zhang, Y. Zhang, Q. Li, X. Zhou, Q. Li, J. Yi, Y. Liu and J. Zhang, *J. Mater. Chem. A*, 2020, **8**, 9776–9787.

125 Y. Wang, P. Hou, Z. Wang and P. Kang, *ChemPhysChem*, 2017, **18**, 3142–3147.

126 X. Jiang, H. Li, J. Xiao, D. Gao, R. Si, F. Yang, Y. Li, G. Wang and X. Bao, *Nano Energy*, 2018, **52**, 345–350.

127 S. Dou, J. Song, S. Xi, Y. Du, J. Wang, Z. F. Huang, Z. J. Xu and X. Wang, *Angew. Chem., Int. Ed.*, 2019, **58**, 4041–4045.

128 M. Perfecto-Irigaray, J. Albo, G. Beobide, O. Castillo, A. Irabien and S. Pérez-Yáñez, *RSC Adv.*, 2018, **8**, 21092–21099.

129 C.-W. Kung, C. O. Audu, A. W. Peters, H. Noh, O. K. Farha and J. T. Hupp, *ACS Energy Lett.*, 2017, **2**, 2394–2401.

130 X. Tan, C. Yu, C. Zhao, H. Huang, X. Yao, X. Han, W. Guo, S. Cui, H. Huang and J. Qiu, *ACS Appl. Mater. Interfaces*, 2019, **11**, 9904–9910.

131 X. Jiang, H. Wu, S. Chang, R. Si, S. Miao, W. Huang, Y. Li, G. Wang and X. Bao, *J. Mater. Chem. A*, 2017, **5**, 19371–19377.

132 P. De Luna, W. Liang, A. Mallick, O. Shekhah, F. P. García de Arquer, A. H. Proppe, P. Todorović, S. O. Kelley, E. H. Sargent and M. Eddaoudi, *ACS Appl. Mater. Interfaces*, 2018, **10**, 31225–31232.

133 N. Kornienko, Y. Zhao, C. S. Kley, C. Zhu, D. Kim, S. Lin, C. J. Chang, O. M. Yaghi and P. Yang, *J. Am. Chem. Soc.*, 2015, **137**, 14129–14135.

134 O. A. Baturina, Q. Lu, M. A. Padilla, L. Xin, W. Li, A. Serov, K. Artyushkova, P. Atanassov, F. Xu and A. Epshteyn, *ACS Catal.*, 2014, **4**, 3682–3695.

135 L. Ye, J. Liu, Y. Gao, C. Gong, M. Addicoat, T. Heine, C. Wöll and L. Sun, *J. Mater. Chem. A*, 2016, **4**, 15320–15326.

136 R. Senthil Kumar, S. Senthil Kumar and M. Anbu Kulandainathan, *Electrochem. Commun.*, 2012, **25**, 70–73.

137 J. Gu, C.-S. Hsu, L. Bai, H. M. Chen and X. Hu, *Science*, 2019, **364**, 1091–1094.

138 I. Choi, Y. E. Jung, S. J. Yoo, J. Y. Kim, H.-J. Kim, C. Y. Lee and J. H. Jang, *J. Electrochem. Sci. Technol.*, 2017, **8**, 61–68.

139 Y. Wang, P. Hou, Z. Wang and P. Kang, *ChemPhysChem*, 2017, **18**, 3142–3147.

140 X. Jiang, H. Li, J. Xiao, D. Gao, R. Si, F. Yang, Y. Li, G. Wang and X. Bao, *Nano Energy*, 2018, **52**, 345–350.

141 Y. Wu, J. Jiang, Z. Weng, M. Wang, D. L. J. Broere, Y. Zhong, G. W. Brudvig, Z. Feng and H. Wang, *ACS Cent. Sci.*, 2017, **3**, 847–852.

142 E. S. Donovan, B. M. Barry, C. A. Larsen, M. N. Wirtz, W. E. Geiger and R. A. Kemp, *Chem. Commun.*, 2016, **52**, 1685–1688.

143 R. Hinogami, S. Yotsuhashi, M. Deguchi, Y. Zenitani, H. Hashiba and Y. Yamada, *ECS Electrochem. Lett.*, 2012, **1**, H17–H19.

144 J. Albo, D. Vallejo, G. Beobide, O. Castillo, P. Castaño and A. Irabien, *ChemSusChem*, 2017, **10**, 1100–1109.

145 M. Hammouche, D. Lexa, M. Momenteau and J. M. Saveant, *J. Am. Chem. Soc.*, 1991, **113**, 8455–8466.

146 Z. Weng, J. Jiang, Y. Wu, Z. Wu, X. Guo, K. L. Materna, W. Liu, V. S. Batista, G. W. Brudvig and H. Wang, *J. Am. Chem. Soc.*, 2016, **138**, 8076–8079.

147 G. Zhu, Y. Li, H. Zhu, H. Su, S. H. Chan and Q. Sun, *ACS Catal.*, 2016, **6**, 6294–6301.

148 S. Lin, C. S. Diercks, Y.-B. Zhang, N. Kornienko, E. M. Nichols, Y. Zhao, A. R. Paris, D. Kim, P. Yang and O. M. Yaghi, *Science*, 2015, **349**, 1208–1213.

149 S. R. Ahrenholtz, C. C. Epley and A. J. Morris, *J. Am. Chem. Soc.*, 2014, **136**, 2464–2472.

150 M. Ding, X. Cai and H.-L. Jiang, *Chem. Sci.*, 2019, **10**, 10209–10230.

151 J.-D. Yi, R. Xie, Z.-L. Xie, G.-L. Chai, T.-F. Liu, R.-P. Chen, Y.-B. Huang and R. Cao, *Angew. Chem., Int. Ed.*, 2020, **59**, 23641–23648.

152 M. Duguet, A. Lemarchand, Y. Benseghir, P. Mialane, M. Gomez-Mingot, C. Roch-Marchal, M. Haouas, M. Fontecave, C. Mellot-Draznieks and C. Sassoye, *Chem. Commun.*, 2020, **56**, 10143–10146.

153 P. Mialane, C. Mellot-Draznieks, P. Gairola, M. Duguet, Y. Benseghir, O. Oms and A. Dolbecq, *Chem. Soc. Rev.*, 2021, **50**, 6152–6220.

154 J. Gu, W. Chen, G.-G. Shan, G. Li, C. Sun, X.-L. Wang and Z. Su, *Mater. Today Energy*, 2021, **21**, 100760.

155 H. Yang, D. Yang, Y. Zhou and X. Wang, *J. Am. Chem. Soc.*, 2021, **143**, 13721–13730.

156 D. Yang, B. Ni and X. Wang, *Adv. Energy Mater.*, 2020, **10**, 2001142.

157 D. Yang, S. Zuo, H. Yang and X. Wang, *Adv. Energy Mater.*, 2021, **11**, 2100272.

158 S. Zhang, N. Liu, H. Wang, Q. Lu, W. Shi and X. Wang, *Adv. Mater.*, 2021, **33**, 2100576.

159 D. Yang, S. Zuo, H. Yang, Y. Zhou and X. Wang, *Angew. Chem., Int. Ed.*, 2020, **59**, 18954–18959.

160 H. Yang, D. Yang and X. Wang, *Angew. Chem., Int. Ed.*, 2020, **59**, 15527–15531.

161 D. Yang, H. Yu, T. He, S. Zuo, X. Liu, H. Yang, B. Ni, H. Li, L. Gu and D. Wang, *Nat. Commun.*, 2019, **10**, 1–10.

162 M.-L. Sun, Y.-R. Wang, W.-W. He, R.-L. Zhong, Q.-Z. Liu, S. Xu, J.-M. Xu, X.-L. Han, X. Ge, S.-L. Li, Y.-Q. Lan, A. M. Al-Enizi, A. Nafady and S. Ma, *Small*, 2021, **17**, 2100762.

163 Y. Benseghir, A. Lemarchand, M. Duguet, P. Mialane, M. Gomez-Mingot, C. Roch-Marchal, T. Pino, M. H. Ha-Thi, M. Haouas, M. Fontecave, A. Dolbecq, C. Sassoye and C. Mellot-Draznieks, *J. Am. Chem. Soc.*, 2020, **142**, 9428–9438.

164 J.-X. Wu, S.-Z. Hou, X.-D. Zhang, M. Xu, H.-F. Yang, P.-S. Cao and Z.-Y. Gu, *Chem. Sci.*, 2019, **10**, 2199–2205.

165 L. Ye, J. Liu, Y. Gao, C. Gong, M. Addicoat, T. Heine, C. Wöll and L. Sun, *J. Mater. Chem. A*, 2016, **4**, 15320–15326.

166 Y. Benseghir, A. Lemarchand, M. Duguet, P. Mialane, M. Gomez-Mingot, C. Roch-Marchal, T. Pino, M.-H. Ha-Thi, M. Haouas, M. Fontecave, A. Dolbecq, C. Sassoye and C. Mellot-Draznieks, *J. Am. Chem. Soc.*, 2020, **142**, 9428–9438.

167 Y. T. Guntern, J. R. Pankhurst, J. Vávra, M. Mensi, V. Mantella, P. Schouwink and R. Buonsanti, *Angew. Chem., Int. Ed.*, 2019, **58**, 12632–12639.

168 Y.-R. Wang, Q. Huang, C.-T. He, Y. Chen, J. Liu, F.-C. Shen and Y.-Q. Lan, *Nat. Commun.*, 2018, **9**, 4466.

169 Y. Guo, W. Shi, H. Yang, Q. He, Z. Zeng, J.-Y. Ye, X. He, R. Huang, C. Wang and W. Lin, *J. Am. Chem. Soc.*, 2019, **141**, 17875–17883.

170 L. Jiao and H.-L. Jiang, *Chem*, 2019, **5**, 786–804.

171 Y. Wu, S. Cao, J. Hou, Z. Li, B. Zhang, P. Zhai, Y. Zhang and L. Sun, *Adv. Energy Mater.*, 2020, **10**, 2000588.

172 C.-W. Kung, C. O. Audu, A. W. Peters, H. Noh, O. K. Farha and J. T. Hupp, *ACS Energy Lett.*, 2017, **2**, 2394–2401.

173 X. Jiang, H. Wu, S. Chang, R. Si, S. Miao, W. Huang, Y. Li, G. Wang and X. Bao, *J. Mater. Chem. A*, 2017, **5**, 19371–19377.

174 A. Wang, J. Li and T. Zhang, *Nat. Rev. Chem.*, 2018, **2**, 65–81.

175 L. Liu and A. Corma, *Chem. Rev.*, 2018, **118**, 4981–5079.

176 R. Qin, P. Liu, G. Fu and N. Zheng, *Small Methods*, 2018, **2**, 1700286.

177 Y. Chen, S. Ji, S. Zhao, W. Chen, J. Dong, W.-C. Cheong, R. Shen, X. Wen, L. Zheng and A. I. Rykov, *Nat. Commun.*, 2018, **9**, 1–12.

178 S. Wei, Y. Wang, W. Chen, Z. Li, W.-C. Cheong, Q. Zhang, Y. Gong, L. Gu, C. Chen and D. Wang, *Chem. Sci.*, 2020, **11**, 786–790.

179 M. Yoo, Y.-S. Yu, H. Ha, S. Lee, J.-S. Choi, S. Oh, E. Kang, H. Choi, H. An and K.-S. Lee, *Energy Environ. Sci.*, 2020, **13**, 1231–1239.

180 C. Zhao, X. Dai, T. Yao, W. Chen, X. Wang, J. Wang, J. Yang, S. Wei, Y. Wu and Y. Li, *J. Am. Chem. Soc.*, 2017, **139**, 8078–8081.

181 X. Wang, Z. Chen, X. Zhao, T. Yao, W. Chen, R. You, C. Zhao, G. Wu, J. Wang, W. Huang, J. Yang, X. Hong, S. Wei, Y. Wu and Y. Li, *Angew. Chem., Int. Ed.*, 2018, **57**, 1944–1948.

182 L. Jiao, W. Yang, G. Wan, R. Zhang, X. Zheng, H. Zhou, S.-H. Yu and H.-L. Jiang, *Angew. Chem., Int. Ed.*, 2020, **59**, 20589–20595.

183 W. Ju, A. Bagger, G.-P. Hao, A. S. Varela, I. Sinev, V. Bon, B. Roldan Cuenya, S. Kaskel, J. Rossmeisl and P. Strasser, *Nat. Commun.*, 2017, **8**, 944.

184 Z.-H. Zhao, H.-L. Zhu, J.-R. Huang, P.-Q. Liao and X.-M. Chen, *ACS Catal.*, 2022, **12**, 7986–7993.

185 H. Shang, T. Wang, J. Pei, Z. Jiang, D. Zhou, Y. Wang, H. Li, J. Dong, Z. Zhuang, W. Chen, D. Wang, J. Zhang and Y. Li, *Angew. Chem., Int. Ed.*, 2020, **59**, 22465–22469.

186 D. Zhao, K. Yu, P. Song, W. Feng, B. Hu, W.-C. Cheong, Z. Zhuang, S. Liu, K. Sun, J. Zhang and C. Chen, *Energy Environ. Sci.*, 2022, **15**, 3795–3804.

187 W. Ren, X. Tan, W. Yang, C. Jia, S. Xu, K. Wang, S. C. Smith and C. Zhao, *Angew. Chem., Int. Ed.*, 2019, **58**, 6972–6976.

188 N. Mohd Adli, W. Shan, S. Hwang, W. Samarakoon, S. Karakalos, Y. Li, D. A. Cullen, D. Su, Z. Feng and G. Wang, *Angew. Chem., Int. Ed.*, 2021, **133**, 1035–1045.

189 H. Zhong, M. Ghorbani-Asl, K. H. Ly, J. Zhang, J. Ge, M. Wang, Z. Liao, D. Makarov, E. Zschech, E. Brunner, I. M. Weidinger, J. Zhang, A. V. Krasheninnikov, S. Kaskel, R. Dong and X. Feng, *Nat. Commun.*, 2020, **11**, 1409.

190 D.-H. Nam, P. De Luna, A. Rosas-Hernández, A. Thevenon, F. Li, T. Agapie, J. C. Peters, O. Shekhah, M. Eddaoudi and E. H. Sargent, *Nat. Mater.*, 2020, **19**, 266–276.

191 W. Guo, X. Sun, C. Chen, D. Yang, L. Lu, Y. Yang and B. Han, *Green Chem.*, 2019, **21**, 503–508.

192 D. Jampaiah, D. Damma, A. Chalkidis, P. Venkataswamy, S. K. Bhargava and B. M. Reddy, *Catal. Today*, 2020, **356**, 519–526.

193 L. Xiong, X. Zhang, X. Xie and Y. Peng, *Chem. J. Chin. Univ.*, 2021, **42**, 2824–2831.

194 M. K. Kim, H. J. Kim, H. Lim, Y. Kwon and H. M. Jeong, *Electrochim. Acta*, 2019, **306**, 28–34.

195 H. Huo, J. Wang, Q. Fan, Y. Hu and J. Yang, *Adv. Energy Mater.*, 2021, **11**, 2102447.

196 Y. Dong, Q. Zhang, Z. Tian, B. Li, W. Yan, S. Wang, K. Jiang, J. Su, C. W. Oloman, E. L. Gyenge, R. Ge, Z. Lu, X. Ji and L. Chen, *Adv. Mater.*, 2020, **32**, 2001300.

197 M. Kuang, A. Guan, Z. Gu, P. Han, L. Qian and G. Zheng, *Nano Res.*, 2019, **12**, 2324–2329.

198 H. Dong, L. Zhang, L. Li, W. Deng, C. Hu, Z. J. Zhao and J. Gong, *Small*, 2019, **15**, 1900289.

199 Z. Pei, H. Li, Y. Huang, Q. Xue, Y. Huang, M. Zhu, Z. Wang and C. Zhi, *Energy Environ. Sci.*, 2017, **10**, 742–749.

200 Z. Pei, Q. Meng, L. Wei, J. Fan, Y. Chen and C. Zhi, *Energy Storage Mater.*, 2020, **28**, 55–63.

201 J. Zhao, H. Lai, Z. Lyu, Y. Jiang, K. Xie, X. Wang, Q. Wu, L. Yang, Z. Jin and Y. Ma, *Adv. Mater.*, 2015, **27**, 3541–3545.

202 Y. Jia, L. Zhang, L. Zhuang, H. Liu, X. Yan, X. Wang, J. Liu, J. Wang, Y. Zheng and Z. Xiao, *Nat. Catal.*, 2019, **2**, 688–695.

203 Y. Jia, J. Chen and X. Yao, *Mater. Chem. Front.*, 2018, **2**, 1250–1268.

204 Q. Wang, Y. Lei, D. Wang and Y. Li, *Energy Environ. Sci.*, 2019, **12**, 1730–1750.

205 Q. Wu, J. Gao, J. Feng, Q. Liu, Y. Zhou, S. Zhang, M. Nie, Y. Liu, J. Zhao and F. Liu, *J. Mater. Chem. A*, 2020, **8**, 1205–1211.

206 H. Yang, H. Wu, G. Li, Q. Lin, Q. Hu, Q. Zhang, J. Liu and C. He, *J. Am. Chem. Soc.*, 2019, **141**, 12717–12723.

207 C. Cao, S. Zhou, S. Zuo, H. Zhang, B. Chen, J. Huang, X.-T. Wu, Q. Xu and Q.-L. Zhu, *Research*, 2023, DOI: **10.34133/research.0079**.

208 X. Li, S.-G. Han, W. Wu, K. Zhang, B. Chen, S.-H. Zhou, D.-D. Ma, W. Wei, X.-T. Wu, R. Zou and Q.-L. Zhu, *Energy Environ. Sci.*, 2023, **16**, 502–512.

209 M. Zhang, S. Zhou, W. Wei, D.-D. Ma, S.-G. Han, X. Li, X.-T. Wu, Q. Xu and Q.-L. Zhu, *Chem. Catal.*, 2022, **2**, 3528–3545.

210 T. N. Huan, N. Ranjbar, G. Rousse, M. Sougrati, A. Zitolo, V. Mougel, F. Jaouen and M. Fontecave, *ACS Catal.*, 2017, **7**, 1520–1525.

211 F. Pan, W. Deng, C. Justiniano and Y. Li, *Appl. Catal., B*, 2018, **226**, 463–472.

212 E. Zhang, T. Wang, K. Yu, J. Liu, W. Chen, A. Li, H. Rong, R. Lin, S. Ji, X. Zheng, Y. Wang, L. Zheng, C. Chen, D. Wang, J. Zhang and Y. Li, *J. Am. Chem. Soc.*, 2019, **141**, 16569–16573.

213 X. Li, Y. Zeng, C.-W. Tung, Y.-R. Lu, S. Baskaran, S.-F. Hung, S. Wang, C.-Q. Xu, J. Wang and T.-S. Chan, *ACS Catal.*, 2021, **11**, 7292–7301.

214 W. Ju, A. Bagger, X. Wang, Y. Tsai, F. Luo, T. Möller, H. Wang, J. Rossmeisl, A. S. Varela and P. Strasser, *ACS Energy Lett.*, 2019, **4**, 1663–1671.

215 A. S. Varela, M. Kroschel, N. D. Leonard, W. Ju, J. Steinberg, A. Bagger, J. Rossmeisl and P. Strasser, *ACS Energy Lett.*, 2018, **3**, 812–817.

216 X. Zu, X. Li, W. Liu, Y. Sun, J. Xu, T. Yao, W. Yan, S. Gao, C. Wang, S. Wei and Y. Xie, *Adv. Mater.*, 2019, **31**, e1808135.

217 E. Zhang, T. Wang, K. Yu, J. Liu, W. Chen, A. Li, H. Rong, R. Lin, S. Ji and X. Zheng, *J. Am. Chem. Soc.*, 2019, **141**, 16569–16573.

218 M. Jia, S. Hong, T.-S. Wu, X. Li, Y.-L. Soo and Z. Sun, *Chem. Commun.*, 2019, **55**, 12024–12027.

219 Z. Jiang, T. Wang, J. Pei, H. Shang, D. Zhou, H. Li, J. Dong, Y. Wang, R. Cao and Z. Zhuang, *Energy Environ. Sci.*, 2020, **13**, 2856–2863.

220 R. Wang, X. Sun, S. Ould-Chikh, D. Osadchii, F. Bai, F. Kapteijn and J. Gascon, *ACS Appl. Mater. Interfaces*, 2018, **10**, 14751–14758.

221 T. Huan and N. Ranjbar, *ACS Catal.*, 2017, **7**, 1520–1525.

222 X. Qin, S. Zhu, F. Xiao, L. Zhang and M. Shao, *ACS Energy Lett.*, 2019, **4**, 1778–1783.

223 X. Chen, D.-D. Ma, B. Chen, K. Zhang, R. Zou, X.-T. Wu and Q.-L. Zhu, *Appl. Catal., B*, 2020, **267**, 118720.

224 C. Yan, H. Li, Y. Ye, H. Wu, F. Cai, R. Si, J. Xiao, S. Miao, S. Xie and F. Yang, *Energy Environ. Sci.*, 2018, **11**, 1204–1210.

225 Y. N. Gong, L. Jiao, Y. Qian, C. Y. Pan, L. Zheng, X. Cai, B. Liu, S. H. Yu and H. L. Jiang, *Angew. Chem., Int. Ed.*, 2020, **132**, 2727–2731.

226 Z. Geng, Y. Cao, W. Chen, X. Kong, Y. Liu, T. Yao and Y. Lin, *Appl. Catal., B*, 2019, **240**, 234–240.

227 X. Wang, Z. Chen, X. Zhao, T. Yao, W. Chen, R. You, C. Zhao, G. Wu, J. Wang and W. Huang, *Angew. Chem., Int. Ed.*, 2018, **130**, 1962–1966.

228 K. Zhao, X. Nie, H. Wang, S. Chen, X. Quan, H. Yu, W. Choi, G. Zhang, B. Kim and J. G. Chen, *Nat. Commun.*, 2020, **11**, 2455.

229 Y. Guo, H. Yang, X. Zhou, K. Liu, C. Zhang, Z. Zhou, C. Wang and W. Lin, *J. Mater. Chem. A*, 2017, **5**, 24867–24873.

230 S. Ye, G. Fan, J. Xu, L. Yang and F. Li, *Electrochim. Acta*, 2020, **334**, 135583.

231 Y. Zhang, K. Li, M. Chen, J. Wang, J. Liu and Y. Zhang, *ACS Appl. Nano Mater.*, 2019, **3**, 257–263.

232 H. Cheng, X. Wu, M. Feng, X. Li, G. Lei, Z. Fan, D. Pan, F. Cui and G. He, *ACS Catal.*, 2021, **11**, 12673–12681.

233 H. Shi, H. Wang, Y. Zhou, J. Li, P. Zhai, X. Li, G. G. Gargik, J. Hou, H. Yang and X. Guo, *Angew. Chem., Int. Ed.*, 2022, **61**, e202208904.

234 T. Zhang, X. Han, H. Liu, M. Biset-Peiró, X. Zhang, P. Tan, P. Tang, B. Yang, L. Zheng, J. R. Morante and J. Arbiol, *Energy Environ. Sci.*, 2021, **14**, 4847–4857.

235 K. Yao, H. Wang, X. Yang, Y. Huang, C. Kou, T. Jing, S. Chen, Z. Wang, Y. Liu and H. Liang, *Appl. Catal., B*, 2022, **311**, 121377.

236 Z. Meng, J. Luo, W. Li and K. A. Mirica, *J. Am. Chem. Soc.*, 2020, **142**, 21656–21669.

237 X. Li, L. Liu, X. Ren, J. Gao, Y. Huang and B. Liu, *Sci. Adv.*, 2020, **6**, eabb6833.

238 W. Guo, X. Tan, J. Bi, L. Xu, D. Yang, C. Chen, Q. Zhu, J. Ma, A. Tayal and J. Ma, *J. Am. Chem. Soc.*, 2021, **143**, 6877–6885.

239 Z. Chen, X. Zhang, W. Liu, M. Jiao, K. Mou, X. Zhang and L. Liu, *Energy Environ. Sci.*, 2021, **14**, 2349–2356.

240 Q. Cheng, K. Mao, L. Ma, L. Yang, L. Zou, Z. Zou, Z. Hu and H. Yang, *ACS Energy Lett.*, 2018, **3**, 1205–1211.

241 Y. Pan, R. Lin, Y. Chen, S. Liu, W. Zhu, X. Cao, W. Chen, K. Wu, W.-C. Cheong and Y. Wang, *J. Am. Chem. Soc.*, 2018, **140**, 4218–4221.

242 H. Zhang, J. Li, S. Xi, Y. Du, X. Hai, J. Wang, H. Xu, G. Wu, J. Zhang and J. Lu, *Angew. Chem., Int. Ed.*, 2019, **131**, 15013–15018.

243 K. Jiang, S. Siahrostami, T. Zheng, Y. Hu, S. Hwang, E. Stavitski, Y. Peng, J. Dynes, M. Gangisetty and D. Su, *Energy Environ. Sci.*, 2018, **11**, 893–903.

244 C. Jia, S. Li, Y. Zhao, R. K. Hocking, W. Ren, X. Chen, Z. Su, W. Yang, Y. Wang and S. Zheng, *Adv. Funct. Mater.*, 2021, **31**, 2107072.

245 X. Zhao and Y. Liu, *J. Am. Chem. Soc.*, 2020, **142**, 5773–5777.

246 Q. Fan, P. Hou, C. Choi, T. S. Wu, S. Hong, F. Li, Y. L. Soo, P. Kang, Y. Jung and Z. Sun, *Adv. Energy Mater.*, 2020, **10**, 1903068.

247 X. Rong, H. J. Wang, X. L. Lu, R. Si and T. B. Lu, *Angew. Chem., Int. Ed.*, 2020, **132**, 1977–1981.

248 Y. Wu, C. Chen, X. Yan, X. Sun, Q. Zhu, P. Li, Y. Li, S. Liu, J. Ma and Y. Huang, *Angew. Chem., Int. Ed.*, 2021, **133**, 20971–20978.

249 W. Ni, Y. Gao, Y. Lin, C. Ma, X. Guo, S. Wang and S. Zhang, *ACS Catal.*, 2021, **11**, 5212–5221.

250 B. Zhang, J. Zhang, J. Shi, D. Tan, L. Liu, F. Zhang, C. Lu, Z. Su, X. Tan and X. Cheng, *Nat. Commun.*, 2019, **10**, 1–8.

251 H. Xu, D. Rebollar, H. He, L. Chong, Y. Liu, C. Liu, C.-J. Sun, T. Li, J. V. Muntean and R. E. Winans, *Nat. Energy*, 2020, **5**, 623–632.

252 Y. Zhang, L.-Z. Dong, S. Li, X. Huang, J.-N. Chang, J.-H. Wang, J. Zhou, S.-L. Li and Y.-Q. Lan, *Nat. Commun.*, 2021, **12**, 6390.

253 C. Jia, X. Tan, Y. Zhao, W. Ren, Y. Li, Z. Su, S. C. Smith and C. Zhao, *Angew. Chem., Int. Ed.*, 2021, **60**, 23342–23348.

254 J. Guo, W. Zhang, L. H. Zhang, D. Chen, J. Zhan, X. Wang, N. R. Shiju and F. Yu, *Adv. Sci.*, 2021, **8**, 2102884.

255 Z. Chen, A. Huang, K. Yu, T. Cui, Z. Zhuang, S. Liu, J. Li, R. Tu, K. Sun and X. Tan, *Energy Environ. Sci.*, 2021, **14**, 3430–3437.

256 X. Sun, Y. Tuo, C. Ye, C. Chen, Q. Lu, G. Li, P. Jiang, S. Chen, P. Zhu and M. Ma, *Angew. Chem., Int. Ed.*, 2021, **60**, 23614–23618.

257 Y. Zhang, Q. Zhou, Z. F. Qiu, X. Y. Zhang, J. Q. Chen, Y. Zhao, F. Gong and W. Y. Sun, *Adv. Funct. Mater.*, 2022, **32**, 2203677.

258 W. R. Leow, Y. Lum, A. Ozden, Y. Wang, D.-H. Nam, B. Chen, J. Wicks, T.-T. Zhuang, F. Li and D. Sinton, *Science*, 2020, **368**, 1228–1233.

259 F. Pan, H. Zhang, K. Liu, D. Cullen, K. More, M. Wang, Z. Feng, G. Wang, G. Wu and Y. Li, *ACS Catal.*, 2018, **8**, 3116–3122.

260 L. Lin, H. Li, C. Yan, H. Li, R. Si, M. Li, J. Xiao, G. Wang and X. Bao, *Adv. Mater.*, 2019, **31**, 1903470.

261 W. Xie, H. Li, G. Cui, J. Li, Y. Song, S. Li, X. Zhang, J. Y. Lee, M. Shao and M. Wei, *Angew. Chem., Int. Ed.*, 2021, **133**, 7458–7464.

262 X. Cao, L. Zhao, B. Wulan, D. Tan, Q. Chen, J. Ma and J. Zhang, *Angew. Chem., Int. Ed.*, 2022, **134**, e202113918.

263 C. G. Morales-Guio, E. R. Cave, S. A. Nitopi, J. T. Feaster, L. Wang, K. P. Kuhl, A. Jackson, N. C. Johnson, D. N. Abram, T. Hatsukade, C. Hahn and T. F. Jaramillo, *Nat. Catal.*, 2018, **1**, 764–771.

264 D. Chen, L. H. Zhang, J. Du, H. Wang, J. Guo, J. Zhan, F. Li and F. Yu, *Angew. Chem., Int. Ed.*, 2021, **60**, 24022–24027.

265 G. Luo, Y. Jing and Y. Li, *J. Mater. Chem. A*, 2020, **8**, 15809–15815.

266 L. Jiao, J. Zhu, Y. Zhang, W. Yang, S. Zhou, A. Li, C. Xie, X. Zheng, W. Zhou and S.-H. Yu, *J. Am. Chem. Soc.*, 2021, **143**, 19417–19424.

267 Z. Zeng, L. Y. Gan, H. Bin Yang, X. Su, J. Gao, W. Liu, H. Matsumoto, J. Gong, J. Zhang and W. Cai, *Nat. Commun.*, 2021, **12**, 1–11.

268 Z. Liang, L. Song, M. Sun, B. Huang and Y. Du, *Sci. Adv.*, 2021, **7**, eabl4915.

269 J. Jiao, R. Lin, S. Liu, W.-C. Cheong, C. Zhang, Z. Chen, Y. Pan, J. Tang, K. Wu and S.-F. Hung, *Nat. Chem.*, 2019, **11**, 222–228.

270 T. Ding, X. Liu, Z. Tao, T. Liu, T. Chen, W. Zhang, X. Shen, D. Liu, S. Wang and B. Pang, *J. Am. Chem. Soc.*, 2021, **143**, 11317–11324.

271 M. Jia, Q. Fan, S. Liu, J. Qiu and Z. Sun, *Curr. Opin. Green Sustain. Chem.*, 2019, **16**, 1–6.

272 Y. Jiao, Y. Zheng, P. Chen, M. Jaroniec and S.-Z. Qiao, *J. Am. Chem. Soc.*, 2017, **139**, 18093–18100.

273 W. Guo, S. Liu, X. Tan, R. Wu, X. Yan, C. Chen, Q. Zhu, L. Zheng, J. Ma and J. Zhang, *Angew. Chem., Int. Ed.*, 2021, **133**, 22150–22158.

274 Y. Jiang, C. Choi, S. Hong, S. Chu, T.-S. Wu, Y.-L. Soo, L. Hao, Y. Jung and Z. Sun, *Cell Rep. Phys. Sci.*, 2021, **2**, 100356.

275 X. Sun, C. Chen, S. Liu, S. Hong, Q. Zhu, Q. Qian, B. Han, J. Zhang and L. Zheng, *Angew. Chem., Int. Ed.*, 2019, **131**, 4717–4721.

276 M. Zhang, Z. Zhang, Z. Zhao, H. Huang, D. H. Anjum, D. Wang, J.-H. He and K.-W. Huang, *ACS Catal.*, 2021, **11**, 11103–11108.

277 T. Zheng, C. Liu, C. Guo, M. Zhang, X. Li, Q. Jiang, W. Xue, H. Li, A. Li and C.-W. Pao, *Nat. Nanotechnol.*, 2021, **16**, 1386–1393.

278 X.-F. Qiu, H.-L. Zhu, J.-R. Huang, P.-Q. Liao and X.-M. Chen, *J. Am. Chem. Soc.*, 2021, **143**, 7242–7246.

279 G. C. Dubed Bandomo, S. S. Mondal, F. Franco, A. Bucci, V. Martin-Diaconescu, M. A. Ortuno, P. H. van Langevelde, A. Shafir, N. Lopez and J. Lloret-Fillol, *ACS Catal.*, 2021, **11**, 7210–7222.

280 M. Lu, M. Zhang, C. G. Liu, J. Liu, L. J. Shang, M. Wang, J. N. Chang, S. L. Li and Y. Q. Lan, *Angew. Chem., Int. Ed.*, 2021, **133**, 4914–4921.

281 Y. R. Wang, H. M. Ding, X. Y. Ma, M. Liu, Y. L. Yang, Y. Chen, S. L. Li and Y. Q. Lan, *Angew. Chem., Int. Ed.*, 2022, **61**, e202114648.

282 J. Han, N. Li, D. Chen, Q. Xu and J. Lu, *Appl. Catal., B*, 2022, **317**, 121724.